

Elemental abundances of sdB-Stars as benchmark for diffusion models

Master's Thesis in Physics

Presented by:

Lars Möller

12. July 2021

Dr. Karl Remeis-Observatory
Friedrich-Alexander-Universität Erlangen-Nürnberg



Supervisor: Dr. Andreas Irrgang

Contents

1	Introduction	4
2	Target selection and sample	7
2.1	Gaia hot subluminous star catalogue	7
2.2	ESO-Phase 3 archive	7
2.3	FEROS	8
3	Quantitative spectral analysis	9
3.1	Stellar atmospheres	9
3.1.1	Luminosity and effective temperature	9
3.1.2	Radiative transfer	10
3.2	Equations for a model atmosphere	11
3.2.1	Local versus non-local thermodynamic equilibrium	12
3.3	Hybrid LTE/NLTE approach	13
3.4	Model atoms	16
3.5	Spectral lines	16
3.6	Spectroscopic parameters	19
3.7	Fitting method	21
3.7.1	Preparations	21
3.7.2	Fitting	23
3.7.3	Uncertainty calculation	24
4	Photometric analysis	26
4.1	Data	26
4.2	Fitting procedure	27
4.3	SEDs based on photometry	28
4.4	SEDs with combined photometry and spectroscopy	28
5	Fundamental stellar parameters	31
5.1	Gaia	31
5.2	Radius, mass and luminosity	31
6	Results	33
6.1	HD 4539	33
6.2	Kiel and Hertzsprung-Russell diagram	37
7	Results	39
7.1	Elemental abundances with temperature	39
7.2	Silicon model atom	42
8	Discussion	44
8.1	Comparison to Geier et al. 2013	44
8.2	Pulsating stars	46
8.3	Comparison to Michaud et al. 2011	48

9 Summary and conclusion	64
References	66
Acknowledgments	71
Appendix	72

1 Introduction

Stars undergo different evolutionary stages during their lifetime depending on how massive they are. The evolutionary stages can be followed using the Hertzsprung-Russell diagram (HRD), shown in Figure 1.1. The following explanations are related to low-mass stars with a stellar mass of $0.6 - 2.3 M_{\odot}$. Stars are formed from collapsing interstellar clouds. They collapse and form a proto-star with a hydrogen core. As the star accretes more matter, the temperature and pressure in the core rises. When the temperature is finally high enough, the fusion of hydrogen to helium kicks in. The star moves on to the main sequence, where it spends most of its life. Once the hydrogen in the core is exhausted, the next evolutionary stages start. The hydrogen burning moves to a shell outside of the helium core, producing more helium for the core. The lack of energy production in the core causes a contraction, which leads to an expansion of the star's envelope. The star is now on the so called Red Giant Branch (RGB). Due to the expansion of the envelope, the surface temperature drops, which leads to a redder apparent color of the RGB-star. As the star ascends further on the RGB, the helium-core keeps on growing, supplied by the outwards moving hydrogen burning shell. With rising mass, the core gets denser and starts to heat up.

When the RGB-star reaches the tip of the branch, the conditions in the helium core are suited for fusion of helium to carbon and oxygen. Up to now, the core is stabilized by electron degeneracy and has grown to a mass of about $0.5 M_{\odot}$. In the so called helium-flash, the helium fusion is suddenly ignited. This leads to an enormous release of energy, coupled with a strong rise in temperature. This temperature rise lifts the degeneracy and allows the core to expand again. The star moves now onto the horizontal branch (HB).

This horizontal feature in the HRD is of special interest because all stars have roughly the same luminosity. Additionally to the helium burning, the star will continue to burn hydrogen to helium in a small envelope around the core. Depending on how massive the remaining hydrogen envelope is, the star will find itself in different parts of the HB. Stars with more massive envelopes around their cores appear red in their visual spectrum due to a relatively small surface temperature. With decreasing hydrogen envelope mass, the surface temperature rises and the star is found on the HB to the bluer end. The most extreme cases are found on the far left on the so called extreme horizontal branch (EHB). On the blue end of the EHB are the hot subluminous stars of B-type (sdB). They are helium burning stars of about $0.5 M_{\odot}$, with an hydrogen envelope so thin that no hydrogen burning can be sustained. In other words, sdB-stars are cores of red-giants, that are able to fuse helium but have lost most of their hydrogen envelope (Heber 2016).

The discovery of sdB stars dates back to the 1950s and the number of known sdBs remained rather small up until the 1980s. Today there are many identified subluminous B-stars, and the latest catalogue with all possible candidates by Geier et al. (2019) consists of more than 39000 stars. There have been several large projects, like the ESO/SPY survey (Napiwotzki et al. 2001) or the Arizona-Montréal Spectroscopic Program (Fontaine et al. 2014), deriving atmospheric parameters for subluminous stars.

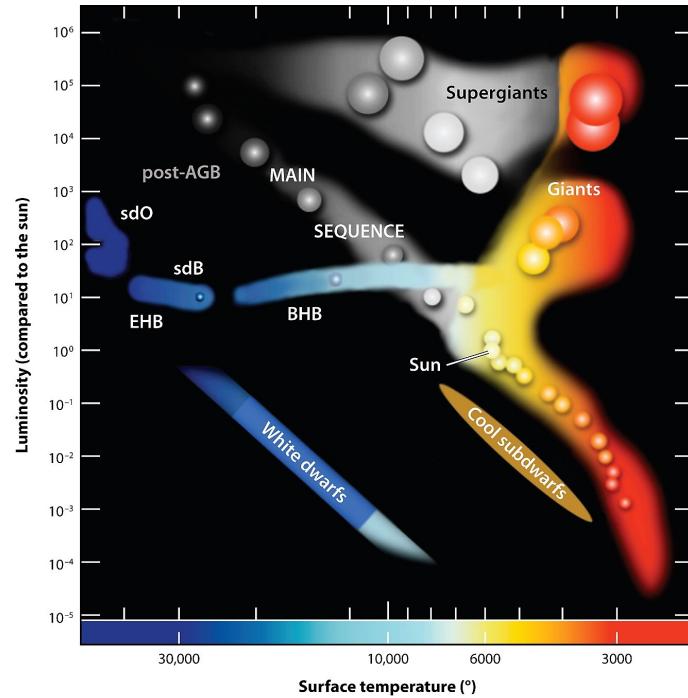


Figure 1.1: Hertzsprung-Russell diagram taken from Heber (2016). The x-axis shows the surface temperature and the y-axis the luminosity in stellar units. There are some evolutionary stages marked in the diagram. Stars spent most of their life time on the main sequence, after which they move onto the red giant branch. The next evolutionary stage is the horizontal branch (HB), followed by the white dwarf stage where the stars evolution ends. The stars in this sample are subdwarfs (sdB) which are located on the so-called extreme horizontal branch (EHB), the blue end of the HB.

The spectra of subdwarf B-stars generally show no signs of micro- or macroturbulences. Furthermore, large rotational broadening of the spectral lines is rather rare, resulting in sharp and distinct spectral lines. However, analysing spectra of sdBs is still time consuming, not due to the spectral lines themselves, but rather due to the composition of the spectra being peculiar. One thing that people discovered early on is that the helium abundance is very low in the spectra of these stars, while other metal abundances are higher than expected from the evolutionary process. This puzzled astronomers at first and explanations for these abundance anomalies have to be found. The generally accepted explanation are diffusion processes, first proposed by Greenstein (1967).

The elemental abundances are set by a balance between gravitational settling and radiative acceleration. Depending on the incidence and strength of the spectral lines of each element, the radiative acceleration is influenced. Saturation of spectral lines limits the radiation pressure, eventually allowing an equilibrium abundance to be reached. The sdB-star has the highest flux in the ultraviolet (UV) spectral range. Because there are only a few helium lines in this spectral region, the radiative support for helium is rather small. Instead for

other elements like iron or silicon, the radiative support is larger, due to many lines in the UV range. This leads to a depletion of helium to very low abundances at the star's surface, and to strong overabundances of other elements. The time scale for this process is rather small compared to the evolutionary time (Heber 2016).

However, the predicted equilibrium helium abundance is lower than the observed one. This means that other mechanisms need to take place to slow the diffusion process down. Michaud et al. (2008, 2011) proposed a model with a turbulent mixing zone making up the outer most layers of the star. Comparing the calculated models to actual observations from Geier et al. (2008, 2010) delivered acceptable results for most of the elements. These diffusion processes are sensitive to the mass of the sdB, as well as to its effective temperature and its metallicity after the red-giant phase (Michaud et al. 2011). These models are still state of the art and will later on be used to compare the findings of this work in Sec. 8.

Diffusion leads to abundance anomalies and each sdB has its own, unique abundance pattern. To understand these poorly understood diffusion processes better and to develop new and accurate models, it is important to derive the elemental abundances of subdwarf B-stars. To determine the elemental abundances of many sdBs, methods have to be found to analyse subdwarf spectra in an efficient way. Geier (2013) developed a semi automatic pipeline to fit the elemental abundances of 106 subdwarfs. This basic analysis uses pre-selected lines, predetermined atmospheric parameters from literature and models assuming local thermal equilibrium (LTE), to model the optical spectra of the star. The method saves a lot of analysis time but it does not provide new insights in atmospheric parameters nor accurate elemental abundances.

I present a detailed analysis of 41 subdwarf B-stars. Their sharp and distinct spectral lines are analyzed to advance our understanding of abundance patterns in sdB stars. The analysis fits atmospheric parameters simultaneously with the elemental abundances using all available lines in the spectra and also considering deviations from LTE, so-called NLTE effects. To this end, high-resolution spectra with good signal-to-noise ratio are needed, which are given by FEROS spectra in the ESO-Phase 3 database for the brightest sdBs of the catalogue by Geier et al. (2019). The most important results of my thesis are atmospheric parameters as well as elemental abundances for each program star for up to 16 different elements (He, C, N, O, Ne, Mg, Al, Si, S, Ar, Fe, Ca, Ti, Cr, P, Sr). With this new insights into diffusion processes and diffusion model developments are possible. The work is organised as follows.

In Sec. 2, the target selection and instruments are introduced. Sec. 3 describes the theoretical fundamentals of the quantitative spectral analysis, going into detail about model atmospheres, line formation and line shaping. Sec. 4 introduces the photometric analysis, the results of which are used to derive the stellar parameters as described in Sec. 5. The results are presented in Sec. 6 and Sec. 7 with the discussion in Sec. 8. The conclusion and an outlook are given in Sec. 9

2 Target selection and sample

The first subdwarf B-stars were discovered in the 1950s, and only a few were known at that time. The Palomar-Green-Survey changed that in the 1980s, finding more stars which fitted the criteria for subdwarf stars. The Sloan Digital Sky Survey (SDSS) doubled the number of known subdwarf stars and nowadays over 5000 subdwarfs are known (Heber 2016; Geier et al. 2019). Identifying new candidates among the many stars in the universe is an ongoing process. The latest subdwarf candidates catalogue is provided by Geier et al. (2019), and it is used for the target selection in this work.

2.1 Gaia hot subluminous star catalogue

"The *Gaia* DR2 catalogue of hot subluminous stars" by Geier et al. (2019) is a continued work based on "the catalogue of known subdwarfs" from 2017 (Geier et al. 2017). The catalogue from 2017 contained about 5600 known subdwarfs and provided, among other things, multi-band photometry, ground based proper motions and atmospheric parameters. With the second data release (DR2) of the European Space Agency's (ESA) astrometric mission *Gaia* (see Sec. 5.1), the catalogue has been extended and now consists of 39800 potential hot subluminous stars candidates. The candidates are selected in *Gaia* DR2 by means of color, absolute magnitude and reduced proper motions cuts. It is expected that the catalogue is almost complete within up to about 1.5 kpc, except the region of the Galactic plane and the LMC/SMC (Geier et al. 2019). For the detailed metal analysis in this work, high-resolution high signal-to-noise ratio spectra are needed. This means that only bright stars in the solar neighbourhood come into question as possible targets. Therefore, all stars of the catalogue with an apparent magnitude of 13 or smaller are taken from the catalogue and are cross checked with the available high-resolution spectra in the archive of the European Southern Observatory (ESO) called ESO-Phase 3 data base.

2.2 ESO-Phase 3 archive

The ESO-Phase 3 data base (ESO 2021a) provides science data products (SDP) with instrument and atmospheric signatures already removed and already calibrated to physical units. While for ESO Public Surveys and ESO Large Programs the upload of the SDPs into the Phase 3 database is mandatory, other smaller surveys can also contribute and upload their data (ESO 2021b). In total 124 different stars from the *Gaia* hot subluminous star catalogue with a magnitude smaller than 13 mag have at least one science spectrum available in the ESO archive. However, not all stars are analyzed in this work. The stars are prioritized by their effective temperature, going from cooler stars to hotter stars. The main reason for this is that the applied model spectra become less and less trustworthy with higher temperature and the spectral lines in the spectrum cannot be treated. Moreover, some stars are misclassified and are not subdwarf B stars.

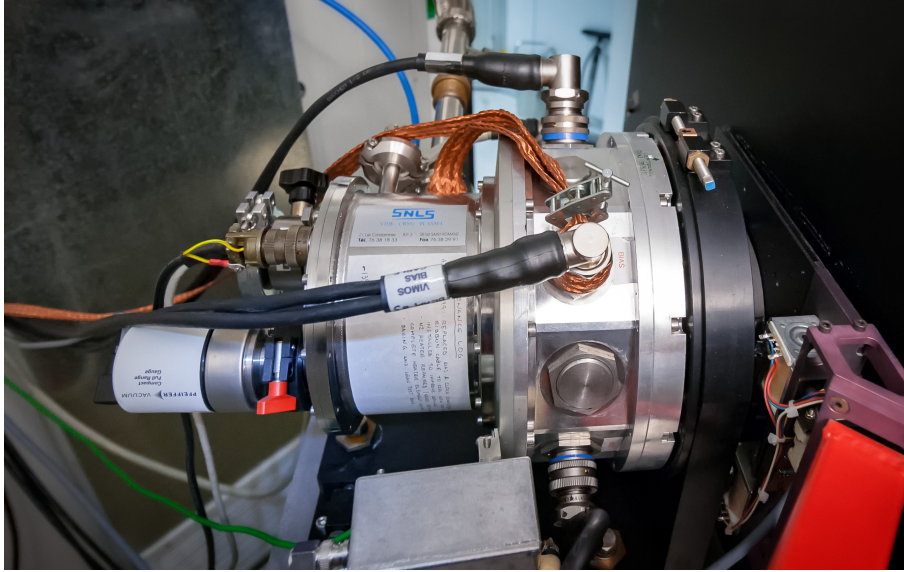


Figure 2.1: The Fiber-fed Extended Range Optical Spectrograph (FEROS) mounted at the 2.2 m telescope at La Silla.

Source: <https://www.eso.org/public/images/AGIL1873-CC/>

Another criterion is that spectral lines are visible in the spectrum. In some cases the signal-to-noise ratio is not good enough to see spectral lines, or there are strange artefacts in the spectra. In other cases fast rotational velocities of the stars provide too weak spectral lines to analyze them. One example would be the star GALEX J093448.2-251248, which is a fast rotating binary star. It is a star of great interest, having 16 available spectra in the ESO-Phase 3 database. The spectra are unusable for determining elemental abundances but I determined the atmospheric parameters, as well as the radial velocity curve of this binary system. The results of this star along with other sorted out stars are available in the appendix. Sorting out stars as well as the time limitation of my master thesis leads to a total of 41 stars which are analyzed in this thesis.

2.3 FEROS

All the different spectra analyzed in this work were taken with the Fiber-fed Extended Range Optical Spectrograph (FEROS). FEROS is currently mounted at the MPG/ESO 2.2-meter telescope at La Silla, Chile. The Echelle-spectrograph was designed to cover the optical spectral range from 3500 Å to 9200 Å in a single spectrogram, at a high-resolution of $R \sim 48000$. To analyse and properly model metal lines in optical spectra, a high-resolution is necessary to see the shape and run of the metal lines. Along with the large optical spectral range, FEROS is the perfect instrument for this analysis. FEROS is fed by two fibers simultaneously, allowing observation and calibration measurements at the same time. The calibration is either done with a calibration lamp or with a region of the sky, close to the actual target (Kaufer et al. 1999). Because all analyzed spectra are taken from ESO-Phase 3 (see Sec. 2.2), data reduction was not necessary.

3 Quantitative spectral analysis

The spectra taken with FEROS are analyzed by matching pre-calculated model spectra to the observations. The calculation of model spectra requires the computation of model atmospheres. Therefore, the theoretical basis of stellar atmospheres is shortly reviewed in the following, mostly based on an analysis by Irrgang (2014).

3.1 Stellar atmospheres

The interior structure of a star is specified by the so called stellar structure equations. These are four differential equations linking the radial distribution of mass, pressure, luminosity, temperature and density to each other. This approach assumes mass continuity, hydrostatic equilibrium, energy conservation, and energy transport via convection or radiation inside every layer of the star, including the star's atmosphere as the most outer layers. Because the star's spectrum is formed in these outer layers, it is important to properly model the atmosphere of a star. This helps to fully understand how the stellar spectra are formed, allowing to calculate model atmospheres, which then can be used to analyse observed spectra. This method allows to determine the atmospheric parameters of the star.

3.1.1 Luminosity and effective temperature

The main mechanism in the atmosphere of a star is radiative transfer. The basic quantity used for this is the specific intensity I_ν . It is defined as the energy dE per frequency interval $d\nu$ that passes in time dt in the direction of the solid angle $d\Omega$ through an area dA with an inclination θ towards the solid angle:

$$I_\nu = \frac{dE}{d\nu \cdot d\Omega \cdot dA \cdot dt \cdot \cos(\theta)}. \quad (3.1)$$

Integrating I_ν over all frequencies gives the total intensity I . Integrating I over all possible directions gives the observable quantity called total Flux F , which is the net amount of energy flowing through the area dA in time dt :

$$F = \int_0^\infty \int_{4\pi} I_\nu \cdot \cos(\theta) \, d\nu d\Omega. \quad (3.2)$$

The flux F can be used to determine the total energy emitted per unit time from the surface S called luminosity L :

$$L = \int_S F dA = 4\pi R^2 F_{\text{Surface}}, \quad (3.3)$$

with R as the radius of the star.

The Stefan-Boltzmann-Law can be used to assign a so-called "effective temperature" to the measured flux of a star. The law states that the flux emitted by a blackbody is equal to $F = \sigma_{\text{SB}} T_{\text{eff}}^4$, where σ_{SB} is the Stefan-Boltzmann constant and T the temperature of the emitter. Applying this law to the surface of a star results in the effective temperature T_{eff} linked to the stellar luminosity L and radius R :

$$L = 4\pi R^2 \sigma_{\text{SB}} \cdot T_{\text{eff}}^4 \quad (3.4)$$

3.1.2 Radiative transfer

The radiative transfer equation (RTE) is used to describe the radiative transfer in stellar atmospheres:

$$dI_\nu = -\kappa_\nu I_\nu ds + \eta_\nu ds. \quad (3.5)$$

κ_ν is the absorption coefficient, η_ν the emission coefficient and ds is the distance that radiation travelled in the direction of a solid angle θ . Ergo, the RTE accounts for changes of the radiation field, caused by absorption and emission of photons. The dimension of κ_ν is length^{-1} . Therefore the characteristic distance a photon can travel before it gets absorbed is given by κ_ν^{-1} .

To simplify the RTE plane-parallelity can be assumed. Then ds can be parametrized by the outbound coordinate dz and $\cos(\theta)$, where θ is the angle to the normal of the plane:

$$ds = \frac{dz}{\cos(\theta)}.$$

By introducing the inbound optical depth

$$\tau_\nu = - \int_{z_0}^z \kappa_\nu \cdot dz',$$

Eq. (3.5) can be rewritten to:

$$\cos(\theta) dI_\nu = I_\nu d\tau_\nu - \frac{\eta_\nu}{\kappa_\nu} d\tau_\nu. \quad (3.6)$$

At this stage the source function $S_\nu = \frac{\eta_\nu}{\kappa_\nu}$ is introduced to reduce the RTE to a first-order differential-equation:

$$\cos(\theta) \frac{dI_\nu}{d\tau_\nu} = I_\nu - S_\nu. \quad (3.7)$$

The formal solution of Eq. (3.7) can be found by multiplying an integrating factor $\exp(-\tau_\nu/\cos(\theta))$, yielding the intensity between two different optical depths τ_1 and τ_2 :

$$I_\nu(\tau_1, \cos(\theta)) = I_\nu(\tau_2, \cos(\theta)) \exp\left(-\frac{\tau_2 - \tau_1}{\cos(\theta)}\right) + \int_{\tau_1}^{\tau_2} \frac{S_\nu(\tau)}{\cos(\theta)} \exp\left(-\frac{\tau - \tau_1}{\cos(\theta)}\right) d\tau. \quad (3.8)$$

The first term in Eq. (3.8) shows that the intensity I_ν is exponentially weakened by absorption on the way from higher optical depths τ_2 to lower optical depths τ_1 . The same is true for the second term of the solution, which considers the contributions of the source function. However, this solution is only a formal solution and must not be applied in reality, because S_ν is also a function of I_ν . The radiation field influences the matter, changing its state and properties. By that κ_ν and η_ν are changed, along with S_ν .

The assumption of plane-parallelity is justified due to the fact that the thickness of the stellar atmosphere is much smaller than the stellar radius R . Therefore the atmosphere can be described by parallel layers. Each layer of the stellar atmosphere is supposed to be homogeneous. Thus, only one coordinate is required to give the location within the atmosphere. Either z or the optical depth τ_ν can be used for this. z increases towards the outer parts of the atmosphere, while τ_ν increases towards the inner region and is zero at the surface. Because τ_ν is a function of frequency, an appropriate mean opacity has to be defined based on Rosseland's description. Time dependent processes like pulsations of the atmosphere can be neglected, because the atmosphere is supposed to be stationary.

3.2 Equations for a model atmosphere

Hydrostatic equilibrium is assumed in all layers of the atmosphere, resulting in the following hydrostatic equation:

$$\frac{dP(z)}{dz} = -G \frac{M}{R^2} \rho(z) = -g\rho(z). \quad (3.9)$$

Here G is the gravitational constant and g the surface gravity, being one of the most important parameters that characterize a stellar atmosphere. The pressure in Eq. (3.9) is a sum of the pressure created by the plasma and the radiation pressure: $P = P_{\text{plasma}} + P_{\text{radiation}}$. While P_{plasma} can be calculated from the equation of state of the plasma, $P_{\text{radiation}}$ can be linked to the frequency dependent flux F_ν , assuming that κ_ν and η_ν are isotropic:

$$\frac{dP_{\text{radiation},\nu}(z)}{dz} = \frac{1}{c} \int_{4\pi} d\Omega \frac{dI_\nu}{dz} \cos^2(\theta) = -\frac{\kappa_\nu}{c} F_\nu. \quad (3.10)$$

Integrating this equation over all frequencies and introducing the radiative acceleration $g_{\text{radiation}}$ results in:

$$\frac{dP_{\text{radiation},\nu}(z)}{dz} = -\frac{1}{\rho(z)c} \int_0^\infty \kappa_\nu F_\nu d\nu \rho(z) = -g_{\text{radiation}} \rho(z). \quad (3.11)$$

This simplifies the P_{plasma} term to:

$$\frac{dP_{\text{plasma}}(z)}{dz} = -\rho(z) (g - g_{\text{radiation}}). \quad (3.12)$$

Also radiative equilibrium is assumed. At each individual point in the atmosphere radiation and emission are in equilibrium. This is given by:

$$\int_0^\infty \int_{4\pi} \kappa_\nu I_\nu d\Omega d\nu \stackrel{!}{=} \int_0^\infty \int_{4\pi} \eta_\nu d\Omega d\nu. \quad (3.13)$$

Using the RTE again and applying Eq. (3.13), this can be rewritten to:

$$\int_0^\infty \int_{4\pi} \cos(\theta) \frac{dI_\nu}{dz} d\Omega d\nu = \int_0^\infty \int_{4\pi} (-\kappa_\nu I_\nu + \eta_\nu) d\Omega d\nu \stackrel{\text{Eq. (3.13)}}{=} 0. \quad (3.14)$$

Pulling the derivative in front of the integration and making use of Eq. (3.2) leads to:

$$\frac{d}{dz} \int_0^\infty \int_{4\pi} \cos(\theta) I_\nu d\Omega d\nu \stackrel{\text{Eq. (3.2)}}{=} \frac{d}{dz} \int_0^\infty F_\nu d\nu = \frac{dF_\nu}{dz} = 0. \quad (3.15)$$

As shown earlier, the flux is linked to the effective temperature T_{eff} via the Stefan-Boltzmann-Law. This means that the equations governing the structure of the stellar atmosphere can be written in terms of the stellar parameters T_{eff} and g . In order to calculate the model atmosphere the following three equations have to be solved:

$$\frac{dP_{\text{plasma}}(z)}{dz} = \rho(z) \left(g - \frac{1}{\rho(z)c} \int_0^\infty \int_{4\pi} I_\nu \kappa_\nu \cos(\theta) d\Omega d\nu \right), \quad (3.16)$$

$$\int_0^\infty \int_{4\pi} \cos(\theta) I_\nu d\Omega d\nu = \sigma_{\text{SB}} T_{\text{eff}}^4, \quad (3.17)$$

$$\cos(\theta) \frac{dI_\nu}{d\tau_\nu} = I_\nu - S_\nu. \quad (3.18)$$

Solving these three equations requires knowledge of the equation of state of the plasma, which is assumed to be an ideal gas. To solve the structure of the atmosphere, knowledge of the source function is crucial, which again requires knowledge of the plasma properties in the atmosphere.

3.2.1 Local versus non-local thermodynamic equilibrium

The source function is heavily influenced by the thermodynamic properties of the plasma. For example how many particles per volume are there at all and what is their velocity distribution. To account for this, the source function is considered in each layer of the atmosphere, which can be done in two different approaches.

Local thermodynamic equilibrium (LTE): One simplifying assumption is that locally each layer of the atmosphere is in thermodynamic equilibrium. This means that each layer can be locally characterized by a certain temperature T . Consequently the particles follow a Maxwell-Boltzmann velocity-distribution and the occupation number densities n_i are described by Boltzmann-excitation. They depend on the energy levels E_i , the local temperature T and its statistical weight g_i ,

$$\frac{n_j}{n_i} = \frac{g_j}{g_i} \exp\left(-\frac{E_j - E_i}{k_{\text{B}}T}\right) \quad (3.19)$$

with k_{B} as the Boltzmann constant.

The ionization equation is given by the Saha-equation for each ionisation stage I :

$$\frac{N_{I+1}}{N_I} = \frac{2}{n_e} \frac{G_{I+1}}{G_I} \frac{(2\pi m_e k_B T)^{\frac{3}{2}}}{h^3} \exp\left(\frac{-\chi_I}{k_B T}\right). \quad (3.20)$$

Here N_I are the number densities of the individual ionization stages, m_e the electron mass, n_e the electron number density, h the Plank constant, χ_I the ionization potential and G_I the partition function which depends on the statistical weights g_i .

Together with the atomic data of each element, these equations allow to calculate the source function of the plasma. This is a very good approximation as long as each layer of the atmosphere can be described by its own properties with index i . This assumption fails when the densities in the atmosphere are so low that the mean-free-path of particles and photons is larger than the typical distance between two zones of different temperature. Another problem is a high photon flux, linking two zones of different temperature to each other. Therefore LTE is a good approximation if collisional, that is, local, interactions dominate over radiative ones. Departures from LTE get more pronounced with increasing effective temperature and declining densities.

Non-local thermodynamic equilibrium (NLTE): In non-local thermodynamic equilibrium the Boltzmann- and Saha-equations (Eq. (3.19) and Eq. (3.20)) cannot be applied anymore. They are replaced by more general equations, called statistical equilibrium or rate equations:

$$n_i \sum_{j \neq i} (R_{ij} + C_{ij}) = \sum_{j \neq i} n_j (R_{ji} + C_{ji}). \quad (3.21)$$

R_{ij} and C_{ij} are the radiative and collisional rates for transitions from level n_i to n_j . It is assumed that the population of any atomic level is stationary with time. Processes populating the atomic level are balanced by the depopulating ones. These rate equations are coupled to the atmospheric structure equations (Eq. (3.16) - Eq. (3.18)). Solving these equations, therefore is a numerically very complex procedure.

3.3 Hybrid LTE/NLTE approach

Calculating a NLTE-model atmosphere is very time consuming. Additionally the determination of spectroscopic parameters is based on a whole grid of models in a multi-dimensional parameter space. Therefore a so-called hybrid LTE/NLTE approach is chosen to reduce the numerical tasks. This hybrid approach was first described by Przybilla et al. (2006) and Nieva & Przybilla (2007) and has since been updated and improved by other authors (Irrgang et al. 2014, 2018).

To get a model atmosphere, multiple steps using different model codes are needed. The basic steps used in this analysis are similar to Irrgang et al. (2018) and will be outlined shortly.

1. ATLAS9: The ATLAS9 code (Kurucz 1993) is used to get an initial guess of the atmospheric structure by solving the atmospheric structure equations in LTE. ATLAS9 accounts for line opacity via pre-tabulated opacity distribution functions (ODFs), which, on the one hand, makes it very fast but, on the other hand, restricts its applicability to the chemical composition of the ODF. ODFs are functions that treat the opacity as a smooth function but only in a sampled frequency interval of the spectrum.

2. ATLAS12: The results from the ATLAS9 calculations are passed into ATLAS12 (Kurucz 1996; Irrgang et al. 2018). The difference to the previous calculations is that ATLAS12 treats opacity through opacity sampling (OS). For OS a large number of selected frequency points is chosen. At each of them the total opacity for each layer of the atmosphere is calculated, by summing over the opacities of atoms, molecules, all bound-free and free-free transitions (Castelli 2005). This leads to a higher accuracy and flexibility in treating opacities, with the downside of much more frequency points and therefore much more computation time. These processes can be accelerated by the ATLAS9 calculations. The resulting atmosphere resulting from the ATLAS12 code will be homogeneous, line-blanketed, plane-parallel and hydrostatic. Still, modelling up to this point is in LTE.

3. DETAIL: The next step is to use the atmosphere out of the ATLAS12 code and pass it into the code DETAIL (Giddings 1981; Irrgang et al. 2018). The code uses the fixed atmosphere and solves the radiative transfer and rate equations for hydrogen, helium and other elements in NLTE using model atoms. The result is the radiation field along with the occupation numbers for the elements involved in NLTE, providing the source function. For now, the radiative transfer is considered in NLTE, whereas the atmospheric structure is described by LTE. To solve this, the NLTE occupation numbers for hydrogen and helium are put back into ATLAS12. All the other metals are incorporated after hydrogen and helium and their opacities are treated as LTE background opacities. An iterative process between the two codes is started. ATLAS12 calculates the structure of the atmosphere, this time using the NLTE occupation numbers of hydrogen and helium, this structure is then used by DETAIL to calculate the NLTE occupation numbers again. This is done until the temperature structure starts to converge and the changes are less than 1 per mille. However DETAIL calculates the source function only for a rough grid of frequencies to speed the process up. This rough grid is not enough to reproduce the line profiles in synthetic spectra.

4. SURFACE: In order to get a final synthetic spectrum, the result of DETAIL is put into the code SURFACE (Giddings 1981; Irrgang et al. 2018). SURFACE uses a finer frequency grid and more detailed line profiles, to determine the formal solution of the RTE (Eq. (3.8)). To obtain the emergent flux, this solution is integrated over one hemisphere of the star:

$$F_{\nu}(0) = 2\pi \int_0^1 I_{\nu}(\tau_2, \cos(\theta)) \exp\left(-\frac{\tau_2}{\cos(\theta)}\right) d\cos(\theta) + \int_0^{\tau_2} \frac{S_{\nu}(\tau)}{\cos(\theta)} \exp\left(-\frac{\tau}{\cos(\theta)}\right) d\tau. \quad (3.22)$$

To obtain a normalized synthetic spectrum, the flux of every frequency point is divided by the continuum flux at that exact point. Not for all atoms a model atom is available. In that case the DETAIL part is skipped and everything is done in LTE. The basic steps are illustrated in Figure 3.1 by Hämmerich (2020). This procedure is called ADS, because the codes employed are ATLAS, DETAIL and SURFACE and can now be used to calculate model spectra.

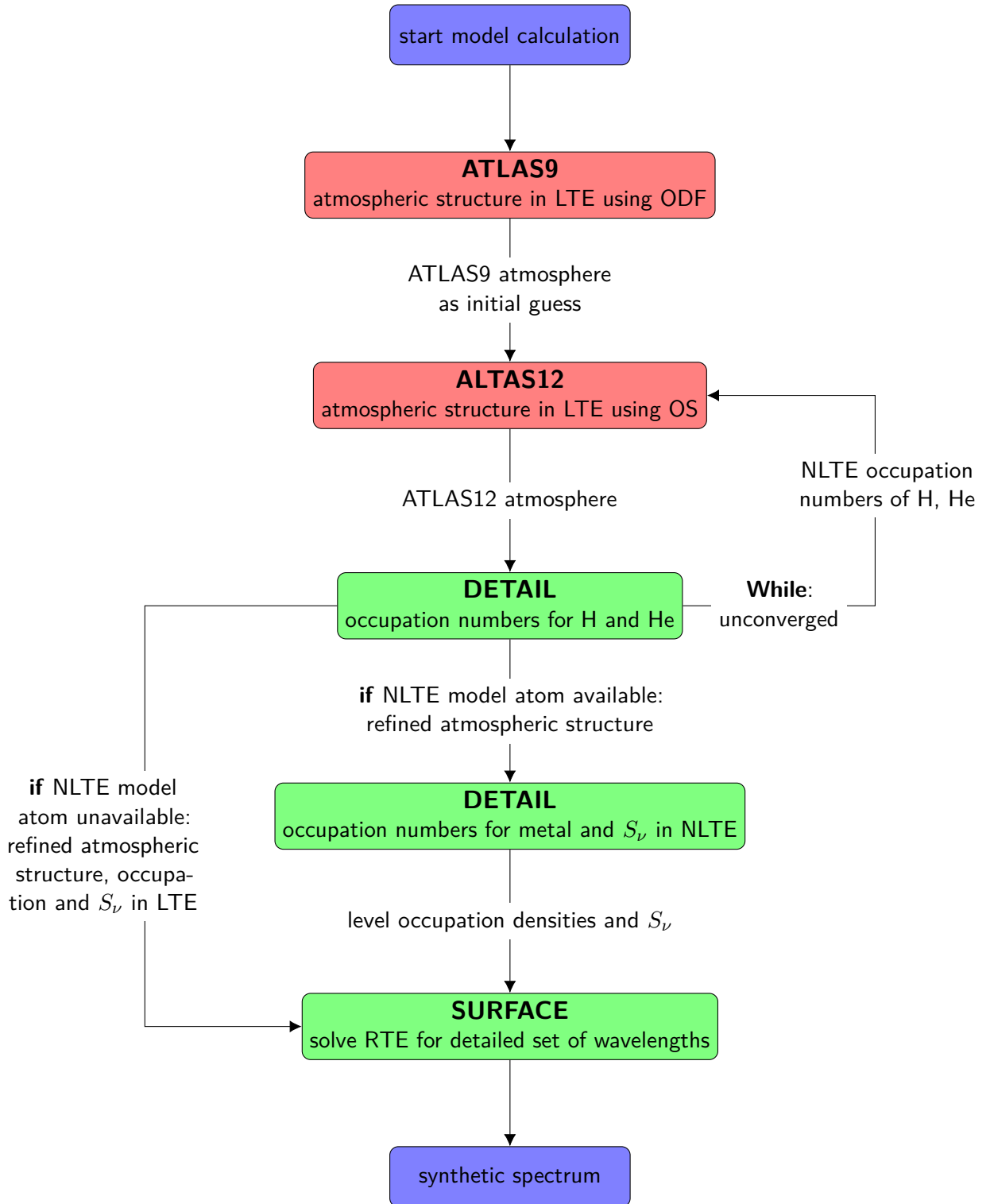


Figure 3.1: The ADS-approach for model spectra calculation. Atmospheric codes using LTE approximation are red, other codes used for NLTE-effects and spectrum-extraction are green, taken from Hämmerich (2020).

element	ionization stages	reference
H		Przybilla & Butler (2004)
He	I, II	Przybilla (2005)
C	II,III	Nieva & Przybilla (2006, 2008)
N	II	Przybilla & Butler (2001); Nieva & Przybilla (2012)
O	I,II	Becker & Butler (1988); Przybilla et al. (2000) Nieva & Przybilla (2012)
Ne	I,II	Morel & Butler (2008); Nieva & Przybilla (2012)
Mg	II	Przybilla et al. (2001)
Al	II,III	Przybilla (in prep.)
Si	II,II,IV	Przybilla & Butler (in prep)
S	II,III	Vrancken et al. (1996)
Ar	II	Butler (in prep.)
Fe	II,III	Becker (1998); Morel et al. (2006) Nieva & Przybilla (2012)

Table 3.1: Available model atoms for the NLTE calculations

3.4 Model atoms

The atmospheric structure equations need atomic data as input. To calculate the atmosphere in NLTE model atoms are constructed. Model atoms contain all kinds of data needed, such as information on the energy levels, transition probabilities, cross-sections for the interaction with photons, etc. The model atoms used during this analysis can be found in Table 3.1. These model atoms do not reflect the full atomic data about one element, but certain ionization stages. These atoms are chosen because they typically occur in sdB-stars. If no model atom is available, the level population is calculated in LTE. Lists containing the transition energies, statistical weights and oscillator strengths are then sufficient as input. For the following elements LTE lists are available: Ca, Ti, Cr, P, Mn, Co, Sr, V.

3.5 Spectral lines

Spectral lines in the stellar spectrum are formed by a discrete transition from one atomic state to another. The wavelength of the spectral line is determined by the energy difference between the upper and the lower atomic states involved in the transition. Atomic transitions of certain elements, and therefore spectral lines, occur at specific wavelengths, and they may serve as fingerprint to identify atoms. Identifying these lines, allows to analyze the composition of the stellar atmosphere. The strength of the spectral lines is connected to

the abundance of the element. In theory the shape of the line is a delta-peak exactly at the given wavelength of the atomic transition. In reality many effects broaden the spectral line, some of them will be briefly introduced in the following:

- **Natural line width:** Energy levels do not have an infinite lifetime t , but decay after a certain period of time. Due to the Heisenberg uncertainty principle $\Delta E \Delta t \geq h$, the energy difference between the excited and de-excited state is not sharp but has an intrinsic spread ΔE . Therefore an energy range exists for the emitted/absorbed photons, which naturally broadens the line.
- **Pressure broadening:** All ions in the plasma interact with each other via the Coulomb force. The resulting electric field leads to a shift of the energy levels via the Stark effect. Electrons are mainly responsible for this effect, due to their mobility and attracting Coulomb force. With increasing density and gravity acceleration, the pressure in the stellar atmosphere rises. The electron density rises, leading to closer encounters and stronger Coulomb interactions.
- **Thermal Doppler broadening:** The velocity of the atoms in a stellar atmosphere follows a Maxwell-Boltzmann distribution. Due to the well-known Doppler effect, frequencies of photons moving along the line-of-sight will be shifted. This results in the so called Thermal-Doppler broadening of the spectral lines.
- **Microturbulence:** To match the model spectra with the observations, another parameter must be introduced. The so-called microturbulence covers tiny motions of the atoms, which are far below the mean free path. The origin of the microturbulence is not yet understood, but is probably not thermal in nature. While normally having a strong effect on the metal lines in a spectrum, there is yet no evidence for a significantly high microturbulence in subdwarf B stars.

These broadening processes are all uncorrelated and need to be combined to give the total line profile. So far all processes are on a microscopic scale. But there are also processes on a macroscopic scale.

- **Rotational broadening:** Rotational movements of the star also lead to broadening of the line. The center of the projected stellar disk is in no motion, while one side of the star is moving towards the observer, the other side away from him. Photons emitted from the side moving towards the observer get blue shifted by the Doppler effect, increasing with increasing distance of the emission site from the star's center. This leads to an elliptical shape of the lines in the spectrum of the star. The velocity of the rotation is important for this effect: The faster the star rotates, the more broadened are the spectral lines. Because the Doppler effect only provides the radial velocity component, the inclination angle i of the star towards the line-of-sight of the observer also has to be considered. This relation is expressed as $v_{\text{rot, observed}} = v_{\text{rot}} \sin(i) = v \sin(i)$
- **Macroturbulence:** Like the microturbulence, movements of large areas in the atmosphere also have an influence on the line profile. Often times these movements are due to pulsations inside of the star, leading to a triangular shaped line profile in the

spectrum. While there are some subdwarf B stars with non-radial pulsations, the effect is typically too small to influence the line profile.

- **Instrumental profile:** Lastly the instrument used for the measurements also introduces a broadening effect. Each spectrograph has a finite resolving power, hence blurring the spectral lines.

For the sdB stars in this work, the microscopic broadening processes are the most important ones, along with rotational broadening. Macroturbulences are typically not present in sdB stars and the instrumental broadening, at a given wavelength λ , from FEROS is $\Delta\lambda = \frac{\lambda}{48000}$. Rotational broadening becomes apparent in the spectrum at rotation velocities of $v \sin(i) \approx 15 \frac{\text{km}}{\text{s}}$ and higher, which is the case for some stars in the sample.

3.6 Spectroscopic parameters and model spectra

In order to fit the observed spectra of sdB-stars, a grid of model spectra has to be pre-calculated. Parameters going into the calculation of the model atmospheres are varied, resulting in a grid of synthetic spectra with as many dimensions as the number of input parameters. There are four primary parameters going into the calculation of the model spectra (T_{eff} , $\log(g)$, $\log(n(\text{He}))$ and microturbulence). These four parameters are called primary parameters because they are used in the ATLAS9 and ATLAS12 code to calculate the model atmosphere, which is then later on used in the DETAIL and SURFACE computations for the individual chemical elements. The final dimension of the grid is then the number of metals used, plus the four primary parameters as well as three additional parameters (macroturbulence, projected rotational and radial velocity), which are not calculated in the model spectra, but added later on. In the following each parameter will be shortly introduced.

- **Effective temperature T_{eff} :** As already shown in Sec. 3.1.2, the effective temperature T_{eff} is a measure for the emitted flux and therefore a key parameter for model spectra. The local temperature in any photospheric layer rises or falls with increasing or decreasing T_{eff} . Each chemical element is heavily influenced by the local temperature, changing its excitation and ionization stage. Therefore each spectral line is more or less sensitive to T_{eff} . How the effective temperature changes the profile of a spectral line qualitatively, depends on the atomic structure and environment. In principle the strength of a certain spectral line increases with rising T_{eff} as long as the population of the lower state involved in the transition increases. After the maximum is reached at a certain temperature, the occupation of the lower state starts to decrease again, because the hotter temperatures drive more and more atoms to higher levels and ionization stages. In the model grids used in this work T_{eff} is spaced in 1000 K steps.
- **Surface gravity $\log(g)$:** The surface gravity $\log(g)$ regulates the pressure and density of the stellar plasma. Therefore all spectral lines are sensitive to $\log(g)$. Increasing surface gravity results in a denser plasma and therefore the probability for electron capture is increased, influencing the ionization balance. Looking at elements exhibiting two different ionization stages is therefore a good method to constrain $\log(g)$. But the main indicator for $\log(g)$ is another one. The wings of the Balmer (hydrogen) lines are heavily effected by the pressure broadening effect mentioned in Sec. 3.5. This can be used to determine $\log(g)$, however the wings of the Balmer lines are also sensitive to T_{eff} . Increasing the temperature in hot stars decreases the strength of the Balmer line and narrows the wings. This can be compensated by increasing the pressure broadening with a higher $\log(g)$. Therefore other elements besides hydrogen are needed to determine $\log(g)$. The model grids used in this work have a spacing of 0.2 in $\log(g)$.
- **Helium abundance $\log(n(\text{He}))$:** The logarithmic helium abundance is present in every model used in this work and gives the helium abundance with respect to all particles in number fractions. It is spaced in 0.25 dex steps.
- **Metal abundance $\log(n(x))$:** Depending on the presence of lines observed in the spectrum, each star has a customized grid of model spectra, with which the fitting

procedure is done. Therefore not every star has every chemical element abundance as a parameter. The NLTE metals shown in Table 3.1 are generally used in every model, with some exceptions. Other LTE metals are added along the analysis if spectral lines of this element are found in the spectrum. Like for helium, each metal abundance is given with respect to all particles in number fractions. The spacing for each metal abundance is 0.25 dex.

- **Microturbulence ξ and macroturbulence ζ :** The microturbulence ξ affects typically all lines because it is an microscopic broadening effect on its own. However this effect is very small and only significant if ξ is the dominant broadening effect. Because this is not the case for the spectra analyzed in this work, this parameter is set to zero. The same is the case for the macroturbulence ζ . It is assumed that the influence is so small that it can be neglected and therefore $\zeta = 0$.
- **Projected rotational velocity $v \sin(i)$:** The rotational broadening affects the shape of spectral lines and makes them more elliptical. Therefore the parameter can be derived from the shape of the lines, in particular from isolated, sharp lines. The effect of this parameter is incorporated after the model spectrum has already been computed, namely via a convolution of the synthetic spectrum with a corresponding broadening kernel, and is therefore called a secondary parameter. In this work the parameter is limited from $0 - 500 \frac{\text{km}}{\text{s}}$.
- **Radial velocity v_{rad} :** The radial velocity simply leads to a Doppler shift of the spectrum. In this work multiple spectra of each star are used. To enhance the signal-to-noise ratio, the individual radial velocities of each of the spectra are measured, so that the single spectra of one star can be eventually coadded. This results in one spectrum for each star with $v_{\text{rad}} \approx 0$. Like $v \sin(i)$, the radial velocity is a secondary parameter not directly considered in the model calculations.

As previously said, the primary parameters T_{eff} , $\log(g)$, $\log(n(\text{He}))$ and microturbulence are used to calculate the model atmosphere in ATLAS12. This model atmosphere is then used for all metals which are considered in the model grid. The first step is always calculating a hydrogen and helium (HHE) model within the desired parameter range. Next, each additional element is calculated together with hydrogen and helium. This is done to account for line blends especially in the lines of the Balmer series. Once all additionally needed metals are calculated, the different SURFACE spectra can be multiplied. However, before the multiplication, each metal spectra is divided by the HHE-spectra. In the end the pure HHE-spectra from the beginning is multiplied with each pure metal spectrum. This procedure brings a lot of advantages, the biggest one being that with the resulting model, each parameter can be fitted simultaneously without having to compute all the combinations of the metal abundances. Other fitting procedures often determine only T_{eff} , $\log(g)$ and $\log(n(\text{He}))$ in a first step. In the second step, these three parameters are then fixed to their determined value and all the other elements are fitted. While line blends between hydrogen, helium and metals are being accounted for, blends between two metal elements are not. However, this is not a problem, because the analysed spectra all come from sdB-stars which show only a few lines in the optical range. This leads to sharp, distinct lines in the spectrum, with very few natural blends between the metal elements, making sdB-stars the perfect candidates for this fitting procedure.

For each star a customized grid is calculated, excluding elements which are not present. To find out the parameter range of the customized grids, a grid with only hydrogen and helium lines was used to get a first guess on T_{eff} , $\log(g)$ and $\log(n(\text{He}))$. This is done for each star, allowing to sort them by these three parameters. Stars with similar parameters are divided into groups to calculate a grid containing all the available metals for each group. This saves calculation time, because various stars can be fitted with only one grid. There are no information on the metal abundances yet, therefore the abundances from Naslim et al. (2013) are used as a starting point for each metal in a range of ± 1 dex. These are typical metal abundances for sdB-stars. With that each spectrum can be fitted and analyzed. Because the spacing in the metal abundance is rather large in these grids, a small grid with only three, yet finer spaced, parameter values (T_{eff} , $\log(g)$, $\log(n(\text{He}))$ as well as estimated metal abundances) is computed in the end for each star.

3.7 Fitting method

The grid calculations and all the fitting procedures are done using the ISIS package (Houck & Denicola 2000a). The approach is similar to the one presented in Irrgang et al. (2014), with some updates and improvements.

3.7.1 Preparations

Looking at a typical spectrum of a star in Figure 3.2, the first thing one notices are the big positive spikes (cosmics) in the spectrum. They are produced by cosmic particles hitting the detector during the observation. These cosmics are identified by comparing the flux value of every data-point with the flux of the environment around it. If the deviation of one data-point/pixel is higher than three standard deviations from the surrounding flux, its value is replaced by the mean value of the environmental flux.

Another correction is applied to get rid of the bumpy shape of the spectrum, coming from the spectrograph itself. This is done by using the spectrum of a star called HD 118112. The star only shows hydrogen and helium lines in its spectrum. This makes the modelling of the spectrum fairly simple and the response function of FEROS can be estimated by fitting the spectrum. The spectrum of the actual observation is then divided by this response function of FEROS, correcting the bumpy shape. Figure 3.3 shows both corrections applied to the spectrum shown in Figure 3.2. There are no cosmics anymore and the general shape of the spectrum is flatter than before.

However, because the observed spectra are not flux-calibrated, model and observation have not the same basis, making a comparison difficult. To simplify the comparison, both model and observation are brought to the same basis, by setting the continuum to 1. For this the next step is to normalize the star spectrum. This is done by fitting a cubic spline continuum function to the spectrum with regularly placed anchor points after certain wavelength intervals. The end result is shown in Figure 3.4.

This continuum correction is fitted along with the other parameters, for which the parameters are grouped into three categories. The pre-defined cubic spline anchor points for global continuum normalization, the telluric spectrum, which is included using a grid of transmission spectra with varying airmass and water-vapor and the parameters presented in Sec. 3.6 as the third and most important category.

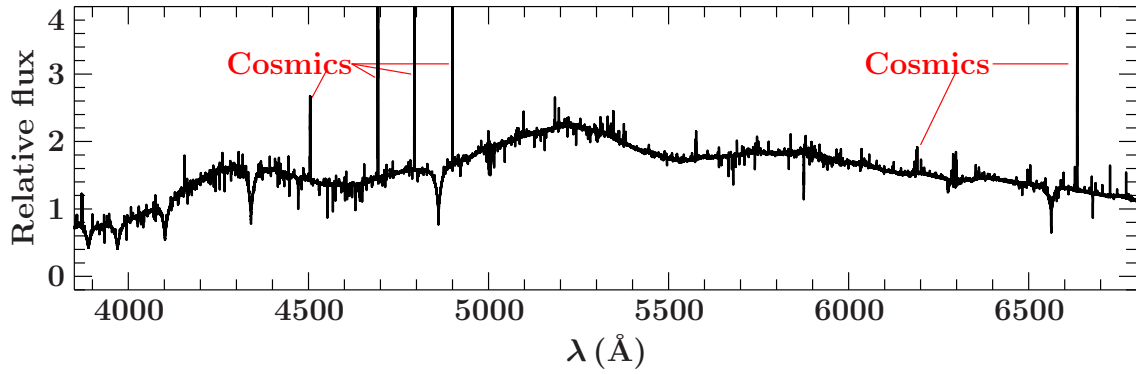


Figure 3.2: Co-added spectrum of CPD-64 481 taken with FEROS in the range of 4000 Å to 6800 Å.

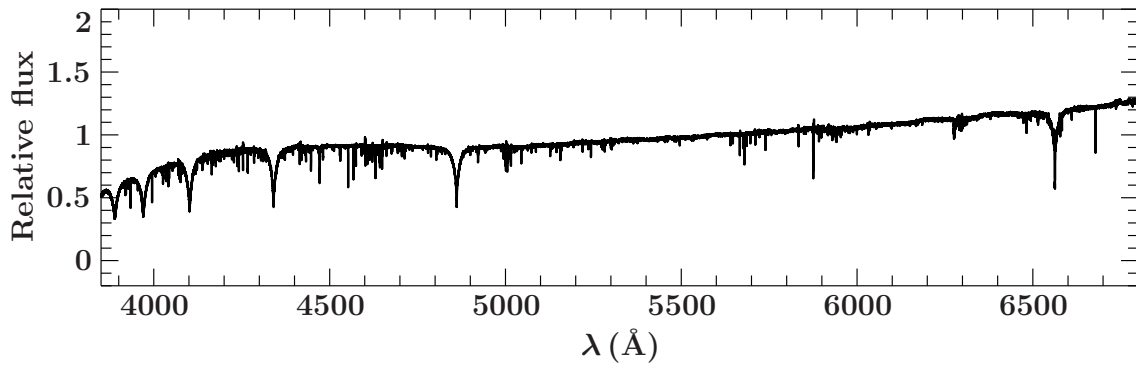


Figure 3.3: Spectrum of CPD-64 481 after removing cosmics and dividing by the response function of FEROS.

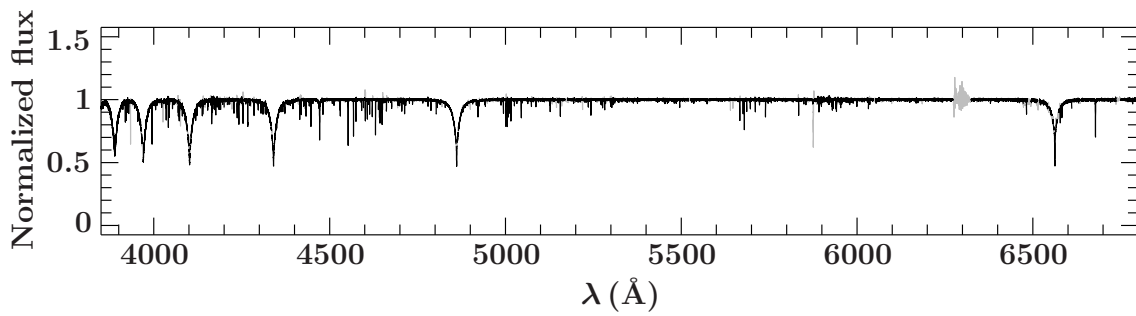


Figure 3.4: Normalized spectrum of CPD-64 481, with all corrections applied.

3.7.2 Fitting

The final calculated grid contains different model spectra in a given range for each free parameter. The observation is compared to the model grid, and by interpolation within the grid the parameters giving the best agreement with the experimental data are found. The best agreement is defined by the goodness-of-fit. It is given by the minimum of the χ^2 statistics, as described below.

In Sec. 3.6 the influence of the individual parameters on the spectra has been discussed. To illustrate this, Figure 3.5 shows different parameter combinations of one hydrogen (H_α) and one helium line (He I 6678 Å). The upper left panel shows a synthetic spectrum calculated with $T_{\text{eff}} = 25000$ K, $\log(g) = 5.6$ and $\log(n(\text{He})) = -3.0$. The other three panels show the same spectrum again, but also a red spectrum which is alternated in one parameter. In the upper right panel, it can be seen that T_{eff} influences the core and the wings of the hydrogen line. Not only the hydrogen line is influenced, but also the strength of the helium line. As mentioned before, the surface gravity is mainly determined by the wings of the Balmer-lines. This is illustrated in the bottom left panel, where a change in $\log(g)$ results in a different wing form. The bottom right panel shows the influence of the helium abundance. As expected, mainly the strength of the helium line is altered. By comparing the actual observed spectra to the model grid, the best parameter combination is found. This is done by χ^2 -minimization. The observed flux F_i at each data-point i , the model flux $F_{\text{model},i}$ and the uncertainty of the observed flux δf_i at the same pixel i , are used to derive the χ^2 :

$$\chi^2 = \sum_i \left(\frac{F_i - F_{\text{model},i}}{\delta f_i} \right)^2 \quad (3.23)$$

ISIS has different χ^2 -minimization algorithms as built-in functions available. I use the two algorithms “mpfit” (Bevington & Robinson 1992) and “powell” (Powell 1964; Zangwill 1967). The default algorithm is mpfit, which is a Levenberg-Marquardt algorithm. Powell uses a non-gradient method to find the minimum of a function. Both are applied during the analysis, making sure the global minimum is found

With this method, the whole spectrum is analyzed and all lines are considered. Yet there are still regions within the spectrum which need to be excluded from the analysis. These are wavelength intervals with interstellar or telluric features. Telluric lines are produced by the atoms in the earth’s atmosphere and not in the observed star. Additionally, metal lines which are not accounted for in the model spectra need to be excluded. These can originate from incomplete atomic data or the spectrum shows metal lines from elements, where no data is available and therefore a modeling is not possible.

After excluding these areas, the quality of the fit can be further improved by applying a so-called local continuum renormalization. During this process, the synthetic spectrum is used to identify the continuum in the spectrum, and the corresponding regions in the observations are then normalized accordingly. The observation is now finally normalized and the best fit can be found. The best fit is determined by the minimum reduced χ^2 , which is expected to be close to unity. Since the χ^2 -statistics are used for the uncertainty calculations, systematic uncertainties are added to achieve a reduced χ^2 of unity. This step assumes that deviations between model and observed spectra are due to systematic uncertainties and appropriate values are added to the statistical ones.

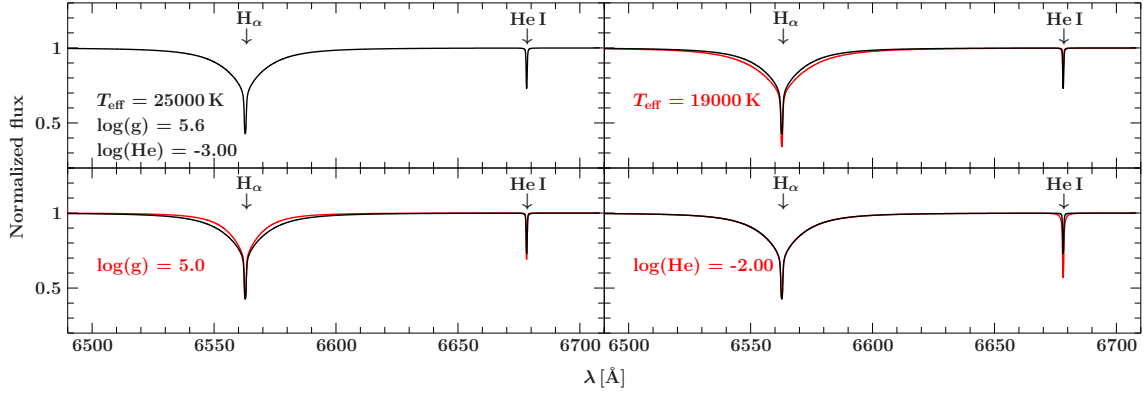


Figure 3.5: Influence of different parameter combinations on the spectrum covering H_α and He I (6678 Å). The upper left panel shows a synthetic spectrum calculated with $T_{\text{eff}} = 25000$ K, $\log(g) = 5.6$ and $\log(n(\text{He})) = -3.0$. The other three panels show the same spectrum in black, but also a red spectrum which is altered in one parameter.

3.7.3 Uncertainty calculation

In addition to the best fitting parameter values, the uncertainties for each value also have to be calculated. The uncertainties presented in this work are all 1σ -uncertainties corresponding to a confidence level of 68%. There are two types of uncertainties which are taken into account during the analysis. The statistical and the systematic uncertainties. The total uncertainty is calculated by combining these two types of uncertainties by quadratic addition.

Statistical uncertainties: In every observed spectra is some noise on the signal. This leads to statistical uncertainties. These uncertainties can be propagated using the χ^2 statistics from the fitting procedure. The starting point for the uncertainty calculation is the best fit with a reduced χ^2 close to one. To determine the uncertainty of one parameter, its value is either increased or decreased, while all the other parameters are fitted. This stepping through one parameter is stopped as soon as the absolute χ^2 is increased by 1. After that, the same procedure is done for the next parameter, until all uncertainties are found. If during this process a new best fit is found, the process for the uncertainty calculation is started all over again.

Systematic uncertainties: Systematic uncertainties are introduced by the analysis of the spectra. These originate from incorrect or missing atomic data, the fitting method or the continuum correction. In general, all procedures applied to the spectra introduce some kind of systematic uncertainty. To get the total systematic uncertainty, all sources have to be considered, as well as the correlations between them, which is however, not feasible. Using the entire spectral range leads to smaller systematic uncertainties, because every parameter is derived using multiple features in the spectra. It is assumed that the most dominant uncertainties are those coming from T_{eff} and $\log(g)$. Therefore by varying these two parameters, the systematic uncertainties can be estimated. The quality of the spectra is very good, therefore a systematic uncertainty of 1% is assumed for T_{eff} and 0.04 dex for

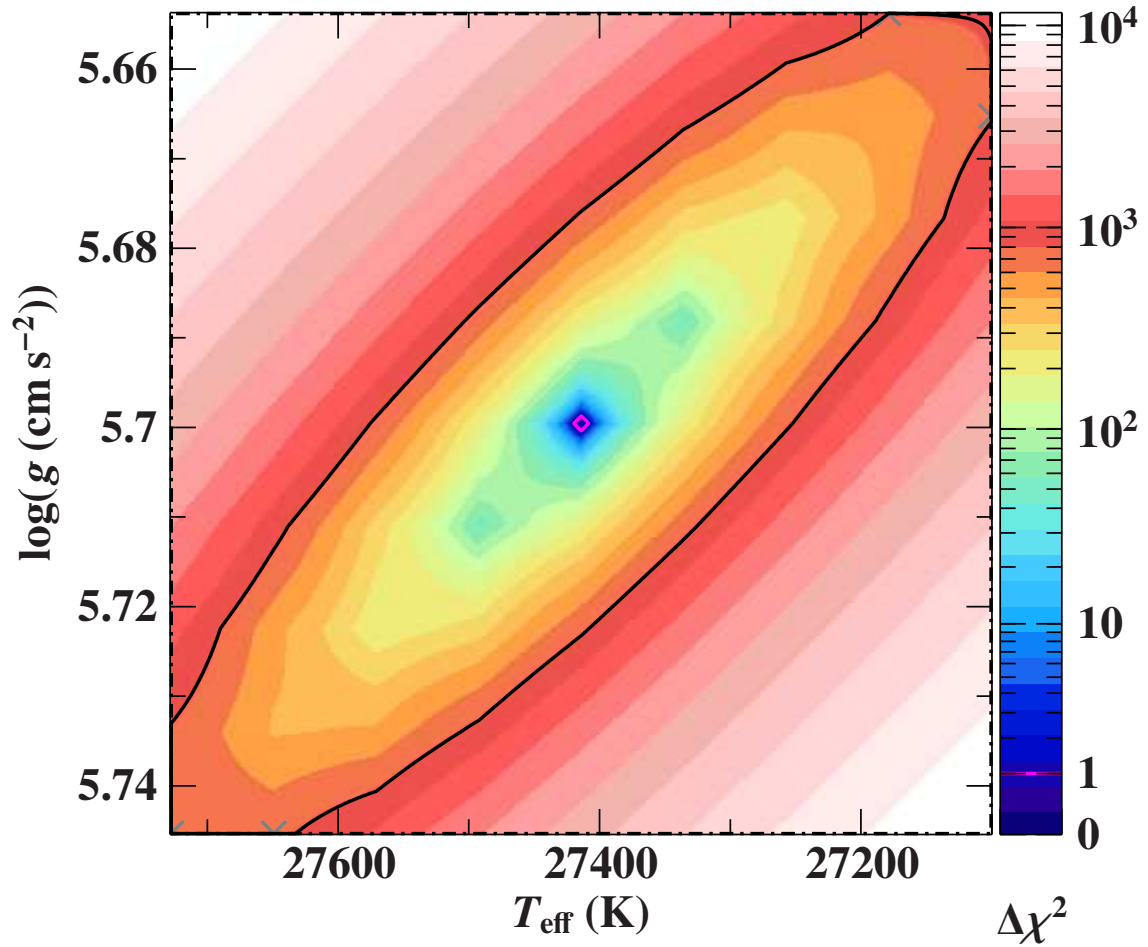


Figure 3.6: Confidence map of the best fit of CPD-64 481.

$\log(g)$. Both parameters are stepped through by taking the best fit for both of them as center and increasing and decreasing them by the quadratic addition of the uncertainties. This is done using 7×7 different parameter combinations. For each combination, T_{eff} and $\log(g)$ are fixed, while all the other parameters are fitted again, which allows to propagate the uncertainties of T_{eff} and $\log(g)$ on all parameters, leading to a confidence map. An example for such a confidence map is shown in Figure 3.6.

4 Photometric analysis

4.1 Data

A star emits light in different wavelength ranges. A photometric analysis is done by combining flux measurements in these different wavelength ranges to form a spectral energy distribution (SED). Various surveys scan the sky in different wavelength ranges using filters of known transmission properties. The photometry from these surveys is compiled by querying the star in the different catalogues. False data are identified and excluded by either missing uncertainties, when magnitudes clearly belong to other nearby sources or are marked with poor quality flags. From the following sources data is used in this work:

- **IUE-Box-Filters:** Spectra from the International Ultraviolet Explorer (IUE) Wamsteker (2000) are used to calculate the magnitudes in three chosen box filters in the ultraviolet range of the spectrum.
- **Tycho:** Tycho is an instrument of the Hipparcos space satellite. It gives two different optical magnitudes V_T and B_T (Høg et al. 2000).
- **Johnson:** The UBV-System uses three filters in the (U)ltraviolet, (B)lue and (V)isual range of the spectrum (Mermilliod 2006).
- **Stroemgren:** The Stroemgren system uses the uvby β photometric system and gives magnitudes for over 60,000 stars (Paunzen, E. 2015).
- **Hipparcos:** The ESA satellite Hipparcos measures magnitudes in the V-Band (van Leeuwen 2007).
- **PAN-STARRS1:** The Panoramic Survey Telescope and Rapid Response System (PAN-STARRS) uses a 1.8 m telescope to image the sky in five broadband filters: g (4866 Å), r (6215 Å), i (7545 Å), z (8679 Å) and y (9633 Å) (Chambers et al. 2019).
- **SDSS:** Like PAN-STARRS, the Sloan Digital Sky Survey (SDSS) images the sky. Similar broadband filters are used: u (3543 Å), g (4770 Å), r (6231 Å), i (7625 Å) and z (9134 Å) (Ahn et al. 2012).
- **SkyMapper:** The SkyMapper survey lead by the Research School of Astronomy provides u, v, g, r, i and z filters, similar to PAN-STARRS and SDSS (Onken et al. 2019; Wolf et al. 2020).
- **Gaia:** Gaia gives fluxes of three optical passbands: G , G_{BP} and G_{RP} .

- **VST:** The VLT survey telescope (VST) is operated by ESO. It surveys the southern sky in comparable depths to the SDSS survey in the northern sky (Shanks et al. 2015).
- **2MASS:** The Two Micron All Sky Survey (2MASS) uses two telescopes to observe the sky. Each telescope measures magnitudes in three different filters simultaneously: J ($1.25 \mu\text{m}$), H ($1.65 \mu\text{m}$) and K ($2.16 \mu\text{m}$) (Skrutskie et al. 2006).
- **VISTA:** The Visual and Infrared Survey Telescope for Astronomy (VISTA) operated by ESO, surveys the sky in the infrared using Z, Y, J, H and K broad band filters (McMahon et al. 2019).
- **UKIDSS:** Similar to VISTA, the UKIRT Infrared Deep Sky Survey (UKIDSS) scans the sky in the broadband filters Z, Y, J, H and K (Dye et al. 2006).
- **DENIS:** In 1996 the ESO started the Deep Near Infrared Survey of the southern Sky (DENIS). During the survey, three different filters J ($1.25 \mu\text{m}$), K ($2.16 \mu\text{m}$) and I ($0.8 \mu\text{m}$) were used. The survey was completed in 2001 (DENIS Consortium 2005).
- **WISE:** The Wide-field Infrared Survey Explorer (WISE) was a space telescope scanning the whole sky in the infrared. It uses filters with central wavelength of $3.4 \mu\text{m}$, $4.6 \mu\text{m}$, $12 \mu\text{m}$ and $22 \mu\text{m}$ (Wright et al. 2010).

4.2 Fitting procedure

Fitting the photometric data provided by the different catalogues requires synthetic magnitudes calculated from a synthetic spectrum. The magnitude of an arbitrary wavelength range x is given by:

$$\text{mag}_x = -2.5 \log \left(\frac{\int_0^\infty r_x(\lambda) f(\lambda) \lambda d\lambda}{\int_0^\infty r_x(\lambda) f^{\text{ref}}(\lambda) \lambda d\lambda} \right) + \text{mag}_x^{\text{ref}}. \quad (4.1)$$

The flux arriving at the detector is $f(\lambda)$, which is weighted with the filter response function r_x of the detector. The λ factor arises from the assumption of photon-counting devices (CCDs). As one can see, the weighted flux is compared to that of a reference object, e.g. the photometric standard star Vega with a given reference magnitude $\text{mag}_x^{\text{ref}}$. Due to the fact that the synthetic spectrum only provides the flux $F(\lambda)$ at the stellar surface, a few corrections have to be made.

The flux arriving at the detector is mostly reduced by the distance d between the source and the detector. Assuming a spherically symmetric object as source, the following relation holds:

$$4\pi d^2 f(\lambda) = 4\pi R^2 F(\lambda). \quad (4.2)$$

The radius R of the distant object is generally unknown, therefore the angular diameter on the celestial sphere $\Theta = \frac{2R}{d}$ is introduced, yielding: $f(\lambda) = \frac{\Theta^2 F(\lambda)}{4}$ (Schaffenroth 2016). Another correction factor is the interstellar extinction. To account for this, the synthetic flux is multiplied with a reddening factor $10^{-0.4A(\lambda)}$. $A(\lambda)$ is the extinction in magnitude at wavelength λ and is a parameterization of the color excess $E(B - V)$ and extinction

coefficient R_V , modeled here using the extinction law by Fitzpatrick et al. (2019). R_V is fixed to 3.1 throughout the analyses, representing the value for the diffuse interstellar medium.

All these corrections applied to Eq. (4.1) yield the following expression for the synthetic magnitude:

$$\text{mag}_x = -2.5 \log \left(\frac{\Theta^2 \int_0^\infty r_x(\lambda) 10^{-0.4A(\lambda)} F(\lambda) \lambda d\lambda}{4 \int_0^\infty r_x(\lambda) f^{\text{ref}}(\lambda) \lambda d\lambda} \right) + \text{mag}_x^{\text{ref}}. \quad (4.3)$$

The grids used during the spectroscopic analysis also contain synthetic SEDs, which are calculated in ATLAS12. Therefore, they can be used to fit the compiled photometric data using a χ^2 minimization. The uncertainties are derived using the χ^2 -statistic, like before for the statistical uncertainties during the spectroscopic analysis (Heber et al. 2018).

4.3 SEDs based on photometry

The best grid to fit the SEDs for all stars in this sample is the large grid containing only hydrogen and helium, which was used for the first guess during the spectroscopic analysis (see Sec. 3.6). During the SED fit T_{eff} , $\log(g)$, $E(B - V)$ and Θ are fitted. The helium abundance is fixed to -1.05 dex, because the SED is completely insensitive to this parameter. However, the uncertainties for effective temperature and surface gravities are significantly higher than those from spectroscopy. Therefore I use the pure SED-Fit only for consistency, to check the results of the spectroscopic analysis for possible errors.

4.4 SEDs with combined photometry and spectroscopy

The atmospheric parameters resulting from spectroscopy are well constrained and can also be used for the SED fit. By plugging T_{eff} and $\log(g)$ in, the fit is done with Θ and $E(B - V)$ as the only free fit-parameters. However, effective temperature and $\log(g)$ are not truly fixed, but the fitting routine only iterates these values between the spectroscopic uncertainties. This leads to a much better constrained angular diameter Θ , which will be used later on. While the main reason of the SED fitting is to get the angular diameter, it is also used to check the sample for binary systems. Binary systems consisting of a subdwarf and a low temperature companion often show an increased flux in the infrared range. If the data provided by the different catalogues introduced earlier in this chapter, indicate such an excess in the infrared, the default binary fit also gives parameters for the companion of the subdwarf. If the data indicates no companion, the binary fit automatically reduces to a single-star fit and gives values for the subdwarf. This allows to check for binary systems, which are otherwise hardly identifiable through the optical spectrum alone. An example for a single SED fit and binary SED fit can be seen in Figure 4.1 and Figure 4.2. With this method four previously known binary systems were identified in the sample, which are shown in Table 4.1.

Name	Gaia DR2 Number
LB 1516	Gaia DR2 6515442543103530624
CD-38 222	Gaia DR2 5000760581717433088
EC 22029-3155	Gaia DR2 6613267462718776832
HE 0230-4323	Gaia DR2 4947023428379802752

Table 4.1: Binary stars, identified through SED fitting.

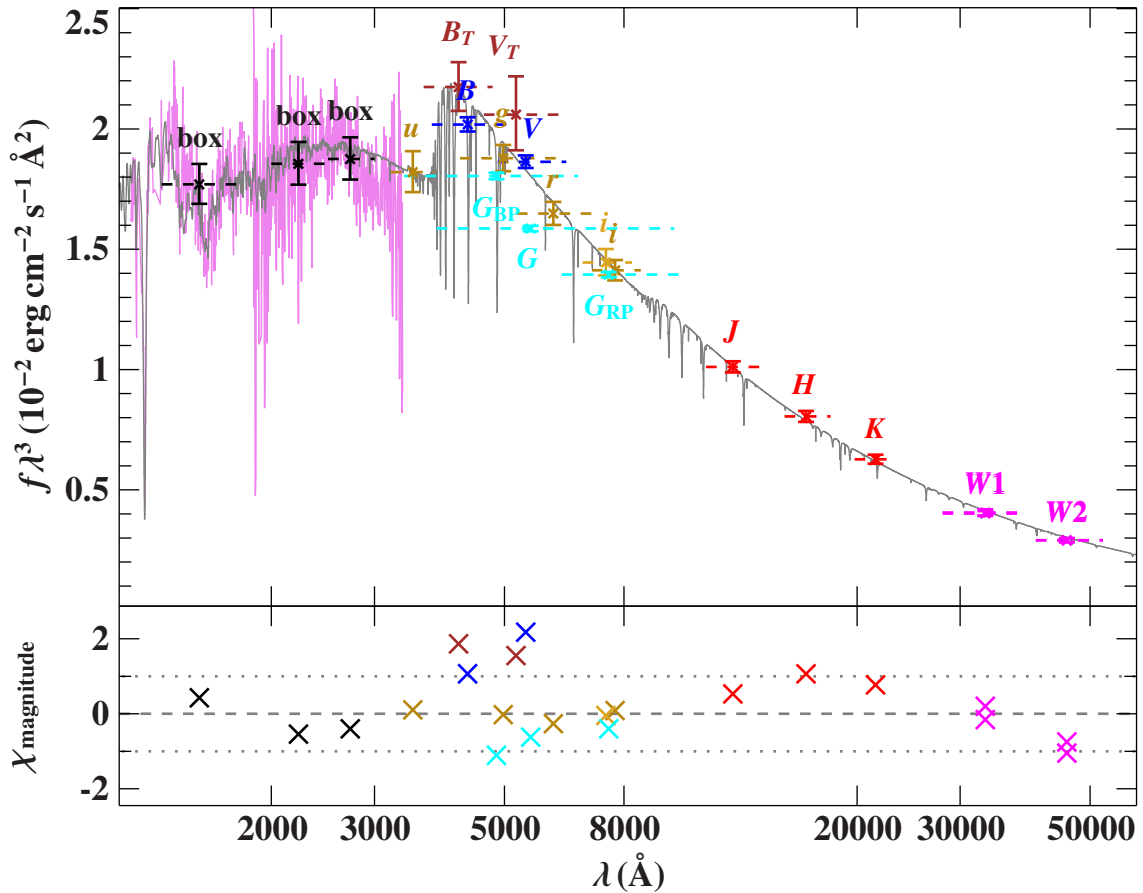


Figure 4.1: SED fit of CPD-64 481. The top panels shows the SED. The grey solid line represents the best fit. The colored data points are the fluxes, converted from the observed magnitudes. To reduce the steep slope of the SED on this wide wavelength range, the flux is multiplied by the wavelength to the power of three. The bottom panels shows the residuals, χ , which is the difference between observed and synthetic magnitudes, divided by the corresponding uncertainties. Each photometric system has a different color: black = IUE-Box-Filters, gold = SkyMapper and SDSS, dark blue = Johnson, dark red = Tycho, turquoise = Gaia, red = 2MASS, magenta = WISE.

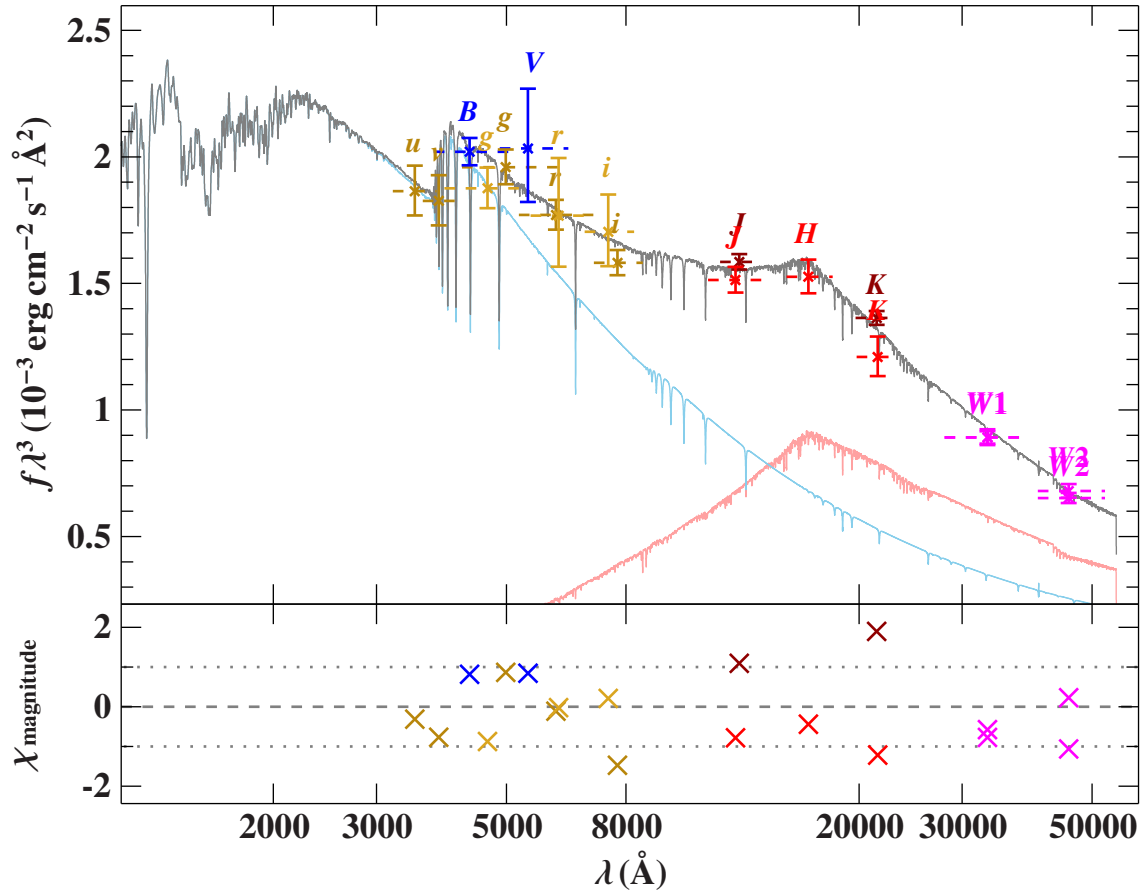


Figure 4.2: SED fit of HE 0230-4323. Like in Figure 4.1, the top panel shows the SED, with the grey solid line representing the best fit. The colored data points are again the fluxes, converted from the observed magnitudes, with the same color code as in Figure 4.1, except this time with dark red = VISTA. The individual contributions of the sdB (light blue) and the companion (light red) are also shown. The bottom panel shows the residuals like in Figure 4.1.

5 Fundamental stellar parameters

Combining the results from the spectroscopic and spectro-photometric analysis with the distance, allows to calculate the fundamental stellar parameters radius, mass and luminosity of each subdwarf (Heber et al. 2018). The distance is determined using parameters given by the Gaia spacecraft.

5.1 Gaia

To determine the distance of each star, data from the Gaia spacecraft is used. Gaia operates in the second Lagrange-point (L2) and scans the sky using two fields of view (FOV), since summer 2014. While operating, the spacecraft slowly rotates around its own axis. Objects in the field of view therefore have a transit motion along the focal plane and are registered by the CCDs. The relative measurements of the two FOVs can be converted into absolute parameters. Gaia measures a lot of parameters of each object, including positions, parallaxes but also photometric data, which is used during the photometric analysis in Sec. 4 (Gaia Collaboration et al. 2016).

For this analysis the parallax is the most important parameter provided by Gaia, because it can be used to derive the distance of the object. All data is taken from the third early data release of Gaia (EDR3) (Gaia Collaboration et al. 2020). To check the trustworthiness of the Gaia data for a specific source, the so called Renormalised Unit Weight Error (RUWE) value can be used. Values greater than 1.4 indicate a bad fit, hence the data should not be used (Lindgren et al. 2020). For this work only data with a RUWE value smaller than 1.4 is used.

5.2 Radius, mass and luminosity

The distance d can be derived using the parallax ϖ provided by Gaia:

$$d = \frac{1}{\varpi} \quad (5.1)$$

Together with Θ from Sec. 4, the radius of the star can be calculated:

$$R_* = \Theta \frac{d}{2} = \Theta \frac{1}{2\varpi}. \quad (5.2)$$

The definition of the surface gravity g is used to express the mass:

$$M_* = g \frac{R_*^2}{G} = \frac{10^{\log(g)} \Theta^2}{4G\varpi^2}. \quad (5.3)$$

The luminosity as the final parameter can be derived using the radius and the effective temperature from spectroscopy:

$$L_* = 4\pi\sigma_{\text{SB}}R_*^2T_{\text{eff}}^4 = \frac{\pi\sigma_{\text{SB}}\Theta^2T_{\text{eff}}^4}{\varpi^2}. \quad (5.4)$$

These three equations are used to calculate the stellar parameters for each sample star. Errors are determined by using a Monte Carlo method of error propagation, using the mode and the highest-density interval (HDI). The mode is the most frequent value of the unimodal distribution and the HDI specifies a probability interval, such that each data point inside the interval has a higher credibility than any point outside of the interval. The results for each sample star are shown in Table 9.7 and Table 9.8

6 Atmospheric and stellar parameter results

The methods presented in the previous chapters are used for all stars in the sample. Each star is analysed using the same approach briefly explained in Sec. 3.7.2. This approach is exemplified in the following for the star HD 4539. The resulting atmospheric parameters are compared to literature values from Schneider et al. (2018), who used a similar approach. This is done to check whether my approach is sufficient and reliable enough for the analysis. After this the results of the whole sample will be discussed in different contexts as well as compared to the previous analysis of Geier (2013). This discussion follows in Sec. 8.

6.1 HD 4539

HD 4539 is a known sdB star about 170 pc away from earth. Its atmospheric parameters have been analyzed before and are typical for sdB stars. The spectra from the ESO-Phase 3 archive are already reduced, but further improvements are necessary to fit the spectra. One spectrum of HD 4539 taken from the archive can be seen in Figure 6.1. To improve the quality of the spectrum, the steps explained in Sec. 3.7.1 are performed. The result after these improvements can be seen in Figure 6.2. The grey parts are areas of the spectra which are excluded from the fit. These areas need to be excluded because there are telluric lines, interstellar lines or gaps/reduction artifacts in the spectrum.

Due to the fact that for a metal analysis a high signal-to-noise ratio is desired, the first step in the analysis is to co-add all available spectra of one star. For this the radial velocity needs to be determined. A simple fit with a hydrogen-helium grid is done to get the radial velocity, as well as a first initial guess on the atmospheric parameters T_{eff} , $\log(g)$ and $\log(n(\text{He}))$. With these initial guess parameters the stars can be grouped, to find stars with similar parameters. The hydrogen-helium fit can be seen in Figure 6.3. For the sake of clarity, the spectrum is only shown up to 6800 Å. The black line is the spectrum, with the fitted model plotted in red. As one can see, there are many metal lines not considered by the model yet. They are not cut out for this fit, because the purpose is only to get a rough idea of T_{eff} , $\log(g)$ and $\log(n(\text{He}))$.

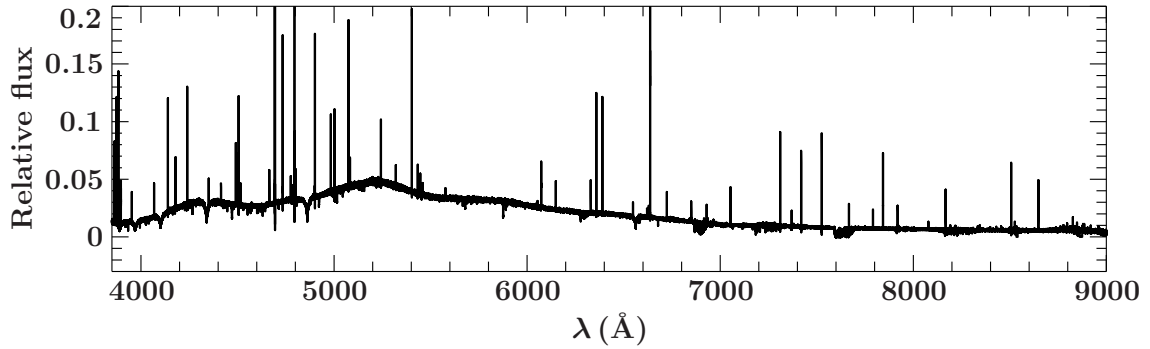


Figure 6.1: One spectrum of HD 4539 taken from the ESO-Phase 3 archive

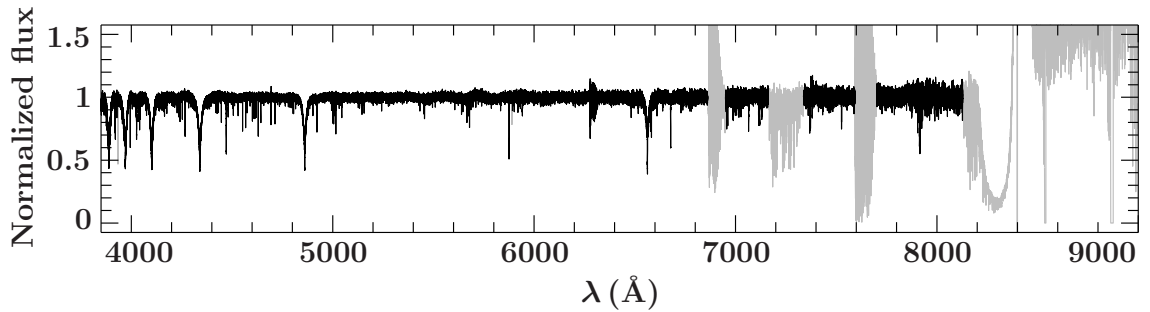


Figure 6.2: Same spectrum of HD 4539 after data preparation as explained in Sec. 3.7.1.

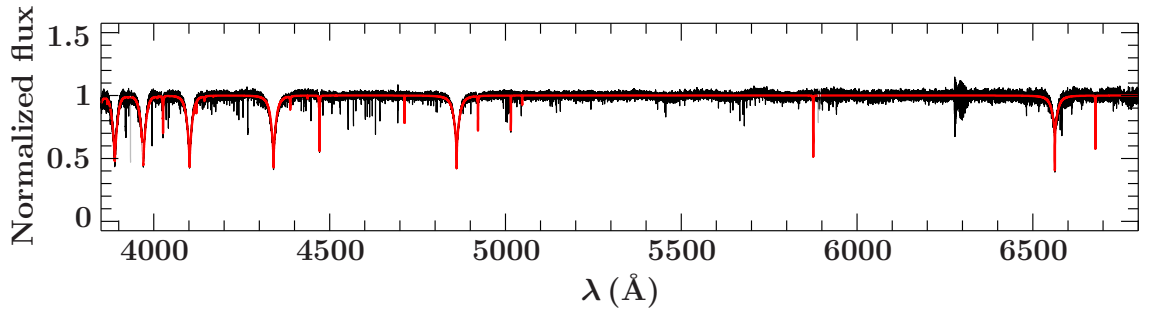


Figure 6.3: Initial guess fit with a hydrogen-helium grid. The observed spectrum is black and the best-fitting synthetic spectrum is red.

With the radial velocities properly considered, all available spectra can be coadded to one spectrum. This improves the signal-to-noise ratio. Because the raw spectra are coadded, the same steps of analysis have to be performed with the coadded spectrum. The result can be seen in Figure 6.4. Again the grey parts represent areas which are excluded from the fit, this time also excluding metal lines for which no atomic data is available.

The next step is to determine the metal abundances. For this grids containing all available metals are used. The abundances from Naslim et al. (2013) are used as a starting point in a range of ± 1 dex. Due to the fact that the stars are grouped by their initial guess

parameters, each grid can be used for many stars, saving a lot of computation time. With the results, a finer grid is finally calculated for each star. It contains only metals for which clear evidence can be found in the spectrum, along with a tailored abundance range of ± 0.25 dex. With this individual grid, the final fit is done. In Figure 6.5 the best fit for HD 4539 is shown along with the residuals of the fit, which are adjusted in an intermediate step to be in the range between -2 and 2. For the sake of clarity the spectrum is only shown up to 6800 Å, because for longer wavelengths, not many metal lines are present in the spectrum.

The comparison to Schneider et al. (2018) is shown in Table 6.1. The values are in very good quantitative agreement.

The full results of HD 4539 as well as the results of the other sample stars are summarized in Table 9.1 to Table 9.6.

Parameter	Schneider et al. (2018)	This work
T_{eff}	23200 ± 470	22900 ± 240
$\log(g)$	5.20 ± 0.1	5.19 ± 0.05
$\log(n(\text{He}))$	-2.27 ± 0.26	-2.29 ± 0.08

Table 6.1: Best fit values for HD 4539 from this work compared to Schneider et al. (2018).

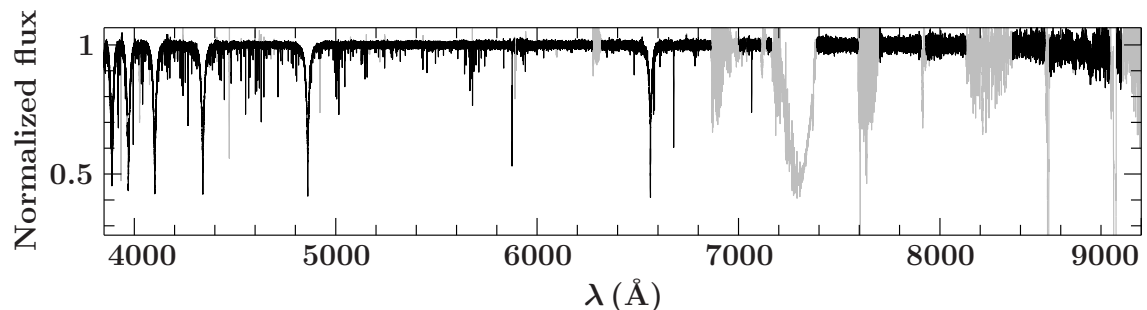


Figure 6.4: Coadded and processed spectrum of HD 4539. The grey parts are excluded from the fit.

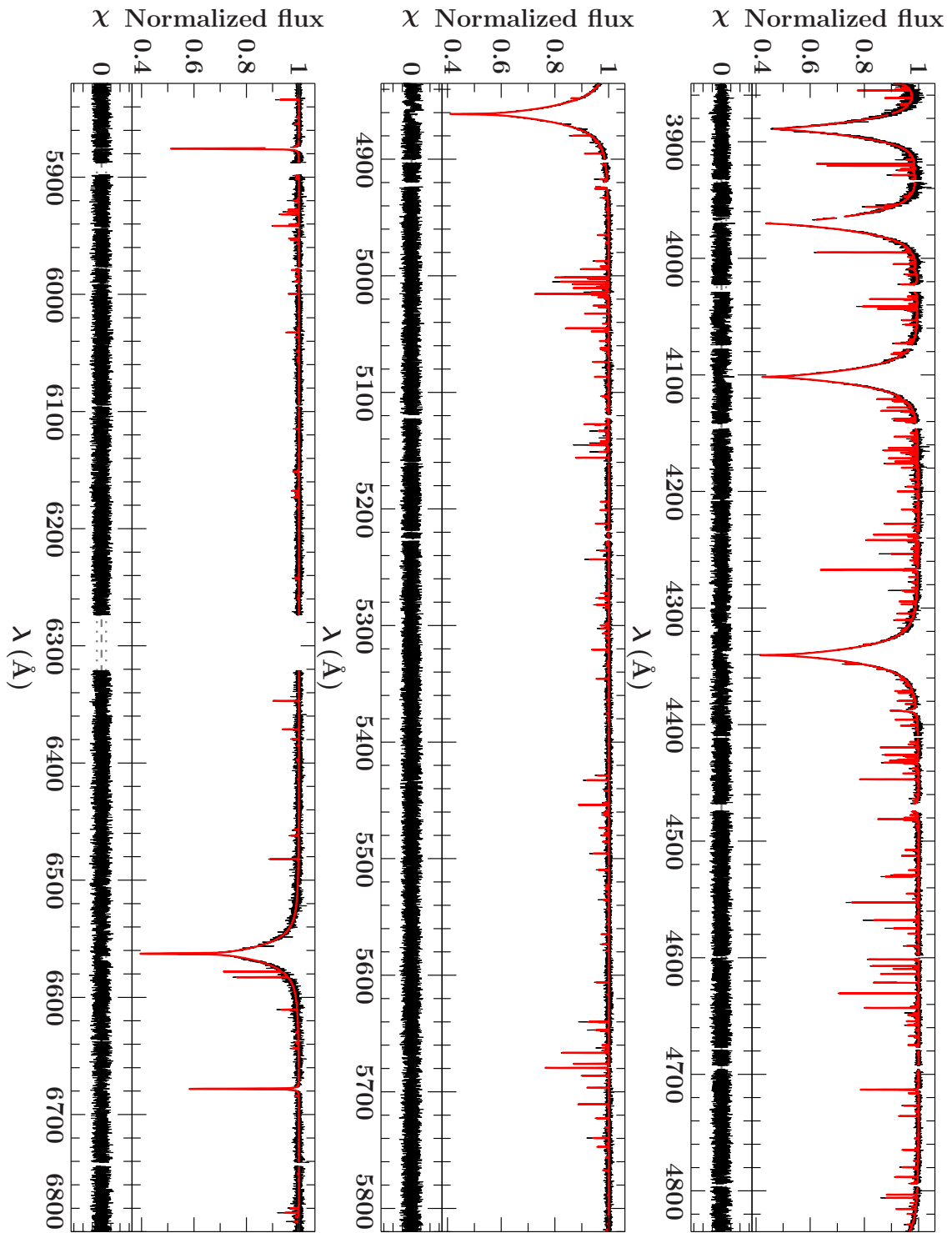


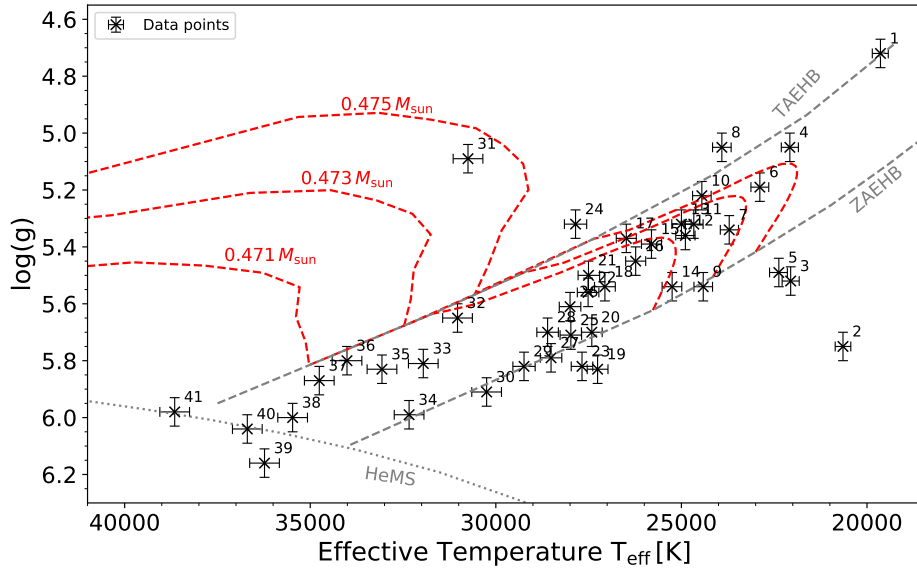
Figure 6.5: Spectrum of HD 4539 in black with the best fit plotted in red. The bottom panel shows the residuals.

6.2 Kiel and Hertzsprung-Russell diagram

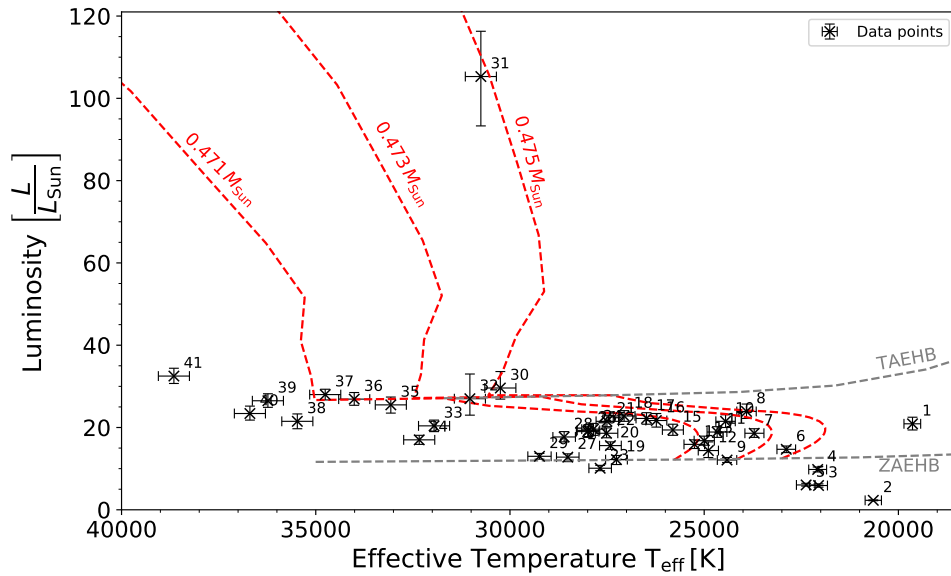
Figure 6.6a shows the logarithmic surface gravities and effective temperatures in Kelvin of all sample stars in a so-called Kiel diagram. For comparison evolutionary tracks with solar metallicity of Dorman et al. (1993) are shown with different masses at the Zero Age Extreme Horizontal Branch (ZAEHB). The extreme horizontal branch (EHB) lies between the ZAEHB and Terminal Age Extreme Horizontal Branch (TAEHB). Most of the sample stars therefore are on the EHB, right where they are expected to be. The star EC 20229-3716 (#31) seems to be an evolved subdwarf star who left the EHB already. Three stars lie on or below the helium main sequence (HeMS), meaning that the hydrogen envelope of these stars should fully be gone, and only the helium core is left. Star number 2 is the low mass sdB HD 188112, which can not sustain helium burning inside of the core. This star evolves as a helium white dwarf and is located below the EHB (Heber et al. 2003). Four other stars also lie below the EHB. One explanation would be a lower mass, placing them below the EHB. However from the derived masses in this work, only stars number 3 and 5 seem to be in line with this explanation with masses of $\approx 0.33 M_{\text{sun}}$. Another yet unlikely explanation would be a higher metallicity for the other two stars, shifting the evolutionary tracks to the right.

In Figure 6.6b the sample stars are shown in a Hertzsprung-Russell diagram with their effective temperature on the x-axis and their luminosity in solar units on the y-axis. Again the evolutionary tracks of Dorman et al. (1993) are shown, which are the same as in Figure 6.6a. The Kiel diagram depends on $\log(g)$, while the HRD depends on the luminosity and is independent of $\log(g)$. The luminosities are derived from spectro-photometry, using the angular diameter Θ and the formulas presented in Sec. 5.2.

Like seen before in the Kiel diagram, most stars lie where they are expected. EC 20229-3716 (#31) has a higher luminosity as all the other stars, because it already evolved from the EHB, confirming the interpretation from the Kiel Diagram. HD 118112 (#2) as expected lies a little bit below the sample and has a low luminosity. The position of star #3 below the main sample at lower luminosity, confirms the explanation of a low mass star from earlier.



(a) Atmospheric parameters of the sample stars, compared to evolutionary tracks from Dorman et al. (1993) in red. The dashed grey lines represent the ZAEHB, TAEHB, as well as the HeMS. The identifications of the stars by numbers is given in Table 9.1 and Table 9.4.



(b) Luminosity and effective temperature of the sample stars. Compared to the same evolutionary tracks from Dorman et al. (1993) as in Figure 6.6a, as well as the ZAEHB and TAEHB. The identifications of the stars by numbers is given in Table 9.1 and Table 9.4.

Figure 6.6

7 Chemical composition results

7.1 Elemental abundances with temperature

Diffusion leads to very different abundance patterns in stars, therefore it is interesting to see whether any trends in metal abundances with rising effective temperature can be found. Figure 7.1 shows the different metal abundances of the sample stars, plotted over the stars' effective temperature.

- **Helium:** The helium abundance for effective temperatures up to 33000 K is rather concentrated to abundances of $\log(n(\text{He})) \approx -2.0$ to -3.0 dex. There are a few outliers in this region, which show either very large helium abundances or low helium abundances of about -4 dex. All sample stars with T_{eff} larger than 33000 K have a general higher helium abundance of -1.0 to -2.0 dex.
- **Carbon:** The carbon abundance varies in the temperature range of 19000 – 40000 K between -4.0 and -6.0 dex with no apparent trends.
- **Nitrogen:** Over the whole temperature range, the nitrogen abundance is limited from -3.0 to -5.0 dex. The general course with rising temperature is flat and most of the stars have an abundance between -5.0 and -4.0 dex, independently from temperature.
- **Oxygen:** For effective temperatures between 19000 and ~ 31000 K the oxygen abundance is mostly between -5.0 and -4.0 dex. In hotter stars of the sample, no oxygen lines could be identified. This is probably due to the fact that the oxygen model atom only covers O I and O II but at such high temperatures O III becomes important.
- **Magnesium:** The magnesium abundance stays pretty much the same over the temperature range between -6.0 and -5.0 dex. It seems that diffusion always leads to magnesium abundances $\sim \frac{1}{10}$ of the solar abundance.
- **Aluminium:** For the whole temperature range, aluminium is rather rare and the abundance has a value between -7.0 and -6.0 dex.
- **Silicon:** While most of the stars have a silicon abundance of ≈ -6.0 to -5.0 , there are a few outliers with stronger abundances up to -4.0 dex and with lower abundances of < -7.0 dex.
- **Sulfur:** The sulfur abundance between 20000 and 30000 K is ≈ -5.5 dex. At temperatures above 30000 K the sulfur abundance starts to rise with rising temperature, up to -4.0 dex at $T_{\text{eff}} \approx 37000$ K.

- **Argon:** The argon abundance behaves similar to the sulfur one. For the lower end of the temperature range the argon abundance is ≈ -5.5 dex and with rising temperature, the abundance starts to rise. With $T_{\text{eff}} \approx 35000$ dex the abundance has risen to -3.5 dex.
- **Iron:** Like expected from the diffusion processes, the iron abundance is more or less at a solar level with values between -5.0 and -4.0 dex. After ≈ 32000 K there is a small dip in the iron abundance to abundances shortly below -5.0 dex.
- **Titanium:** For titanium the same behavior as for sulfur and argon can be seen. It starts with lower abundances of -7.0 to -6.0 dex and with rising temperature, the titanium abundance rises up to -4.0 dex.
- **Strontium:** The strontium abundance is quite flat over the whole temperature range and has typically values of -7.0 dex with some variations up to -6.0 dex.

Other elements found are not shown in Figure 7.1 because they were detected in only a few stars, making it impossible to see any trends over the whole temperature range.

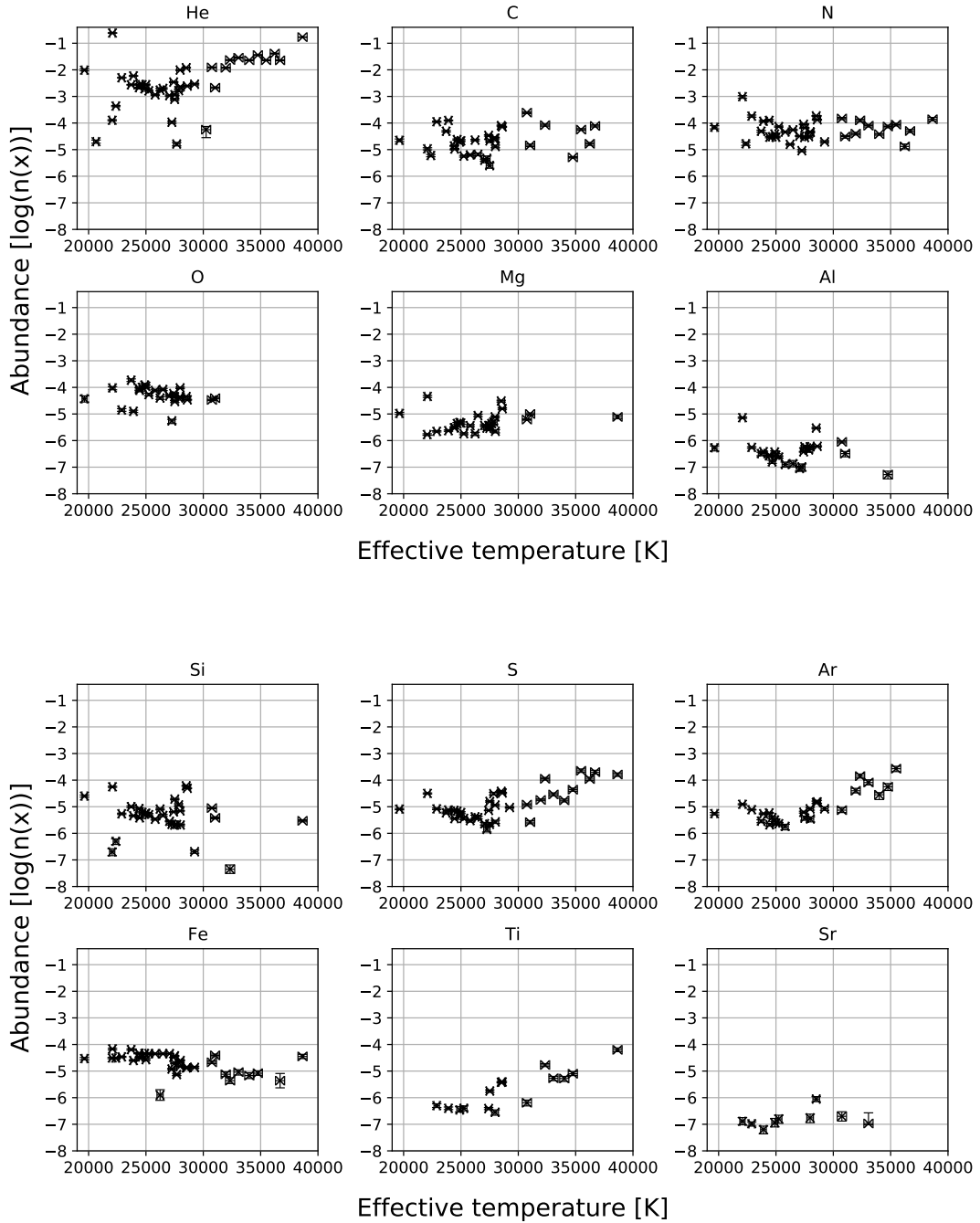


Figure 7.1: Elemental abundances and their dependence on effective temperature

7.2 Silicon model atom

During the analysis of the sample stars a possible problem with the silicon model atom became apparent, which will be discussed in the following. The main indicator for the silicon abundance in the optical range is the so called silicon triplet. It is made up out of three Si III spectral lines close together located at 4552.6 Å, 4567.8 Å and 4574.7 Å. The silicon triplet of HD 4539 along with the best fit, plotted in red, can be seen in the upper panel of Figure 7.2.

Along with the Balmer- and helium-lines, the silicon triplet is an indicator for the effective temperature of a star. In most cases, the fit for the first line of the triplet is very good, while the other two lines are always a little too weak in the model as it is also the case for HD 4539.

However, this phenomenon is already known and not a real concern, when analysing the spectra. The problem with the Si model-atom becomes apparent when looking at Si II, the other ionisation stage of silicon present in the spectrum of HD 4539. While all Si III lines fit decently, all Si II lines are too strong in the model. Two Si II lines from HD 4539 are exemplarily shown in the lower panel of Figure 7.2, with the model data plotted in red. This strange behaviour of the silicon model lines can be seen in various stars, while in other cases model and observation of the Si II lines fitted nicely. One example is CD-32 1567, shown in Figure 7.3. Like before with HD 4539, the first line of the silicon triplet is fitted very well, while the other two lines are a little too weak in the model. When looking at the Si II lines they fit a lot better than for HD 4539, with only the second line being a little bit too strong.

Looking for similarities among the stars with too strong Si II lines in the model, it became clear that the fitting issue depends on the effective temperature. All stars with $22000 \text{ K} < T_{\text{eff}} < 26000 \text{ K}$ are affected by too strong Si II lines, becoming more obvious with better signal-to-noise ratio.

This problem affects the results of the silicon abundance, as well as the effective temperature. To bypass this, the silicon triplet, being the main effective temperature indicator, is weighted stronger during the fit routine than the problematic Si II lines. This allows us to still fit all silicon lines, but with much less weight to lines that are probably affected by problems in the model atom in certain temperature ranges.

To fully resort this problem, the silicon model atom has to be revised and further improvements have to be implemented.

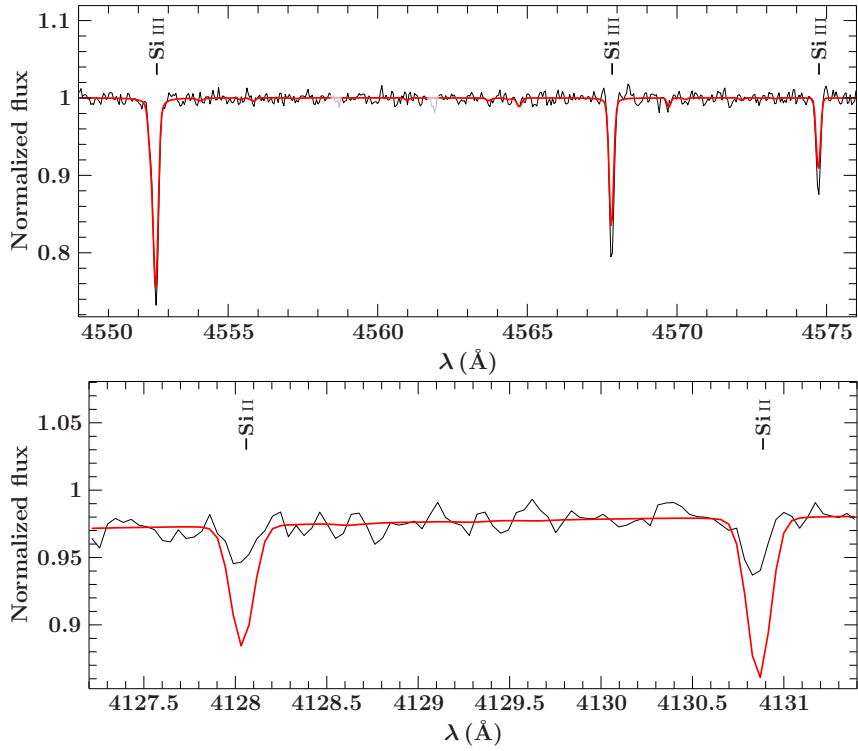


Figure 7.2: Silicon lines of HD 4539 along with the best fit plotted in red

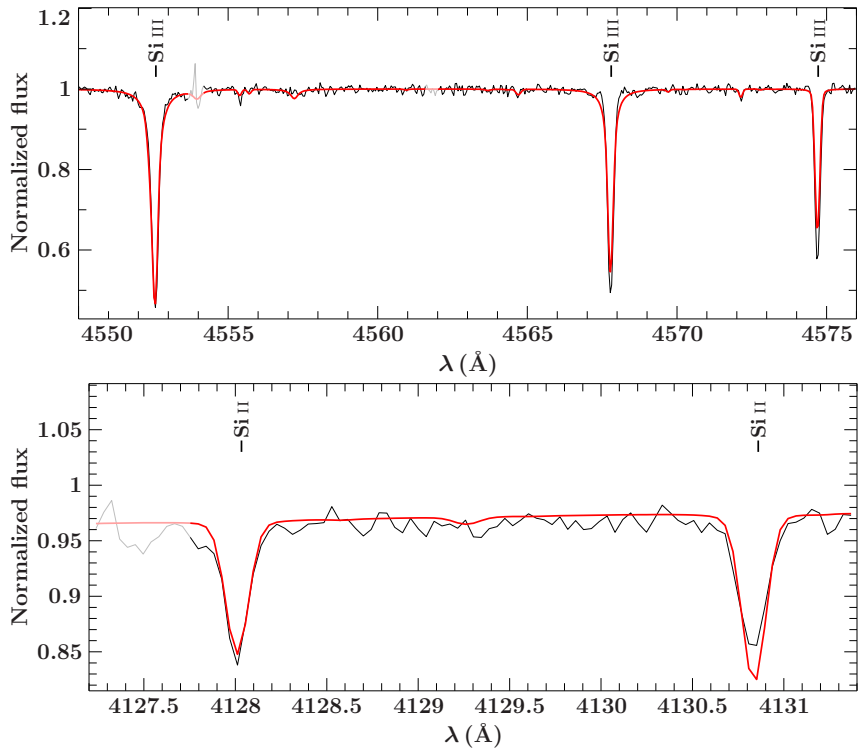


Figure 7.3: Silicon lines of CD-32 1567 with the best fit plotted in red

8 Discussion

8.1 Comparison to Geier et al. 2013

As mentioned in the beginning, Geier (2013) used a semi-automatic approach analysing subdwarf B stars with a pre-selected set of metal lines in the spectrum and models only considering LTE. In the following the results from this work, using all available lines in the spectrum as well as newer models considering LTE and NLTE effects, will be compared to some results of Geier (2013). In total 22 subdwarfs have been analyzed before by Geier and by me in this study.

Figure 8.1 compares the effective temperature of these 22 stars. On the x-axis the results from this work are shown, on the y-axis from Geier (2013). The identity is shown in red. The results are generally in good agreement, with some deviations, but no clear trend can be seen. There are no errors given by Geier (2013), therefore only my analysis shows errorbars.

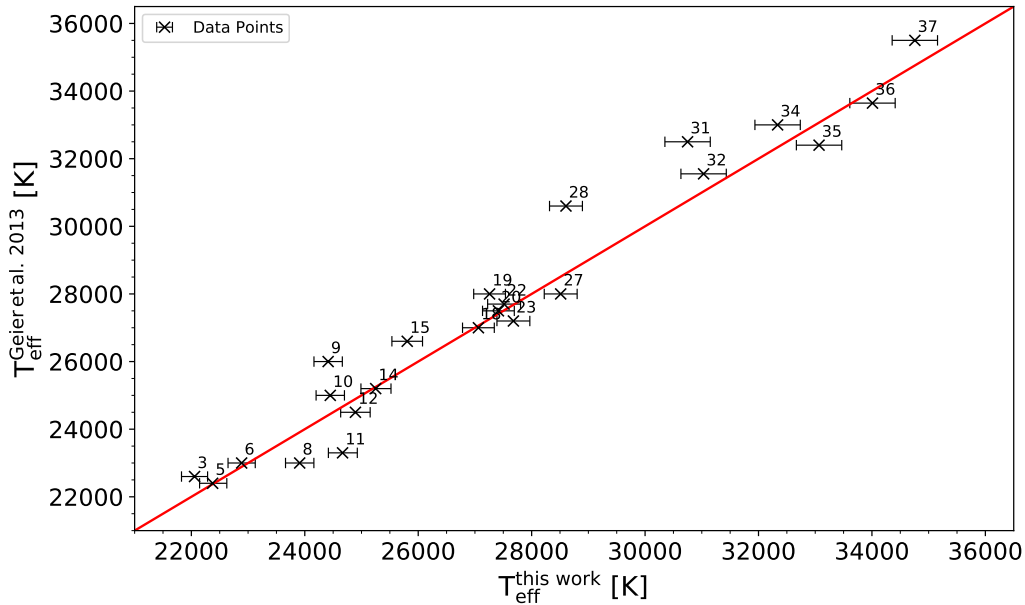


Figure 8.1: Effective temperature results from this work (x-axis) compared to results from Geier (2013) at the y-axis. The identifications of the stars by numbers is given in Table 9.1 and Table 9.4.

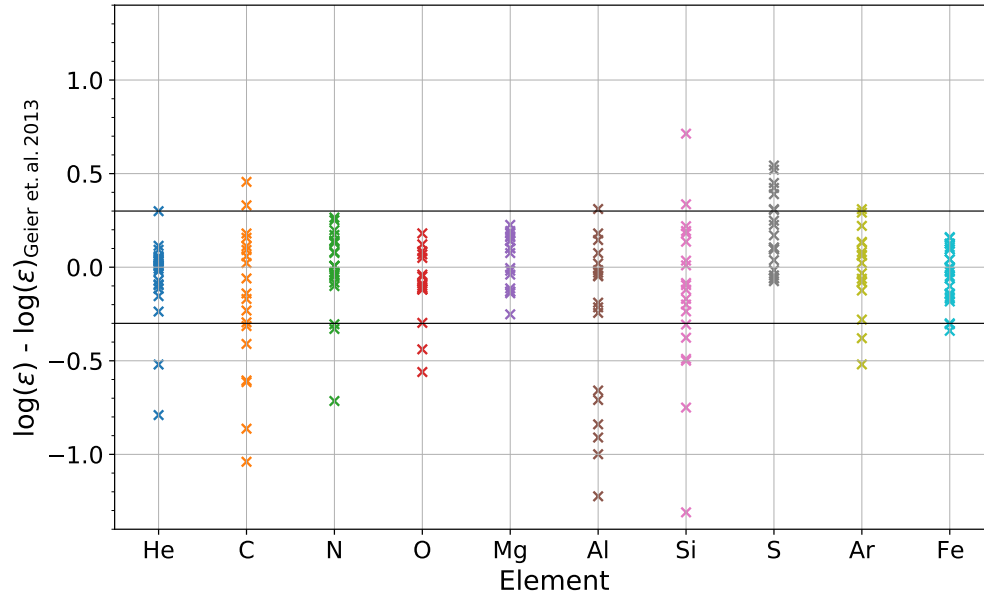


Figure 8.2: Difference of metal abundances between this work and Geier (2013).

Another comparison can be made with the results from the metal abundances. Figure 8.2 shows the difference between the results from both works. The errors from Geier (2013) are 0.3 dex for each element, dominating the final error, because the errors from this work are considerably smaller in the order of 0.05 dex. The 0.3 dex errors are represented by the horizontal lines in Figure 8.2. While most of the results are in good agreement, some of the results show large discrepancies of up to -1.0 dex and beyond. Notably the results for carbon, aluminium and silicon show large differences and sulphur shows a systematic trend to higher abundances. The differences are the lowest for magnesium and iron, indicating that NLTE effects are not so important for these elements.

8.2 Pulsating stars

It is still unknown whether other mechanisms influence the diffusion processes inside of subdwarf B stars. To see if pulsations have an influence on the diffusion processes and therefore on the elemental abundances, the sample stars were cross checked for known pulsators. This was done after the analysis of each star. In total 6 stars out of the 41 sample stars are known pulsators. To see if there are any trends in the abundances, Figure 8.3 shows the elemental abundances of each known pulsator. All elements have a large spread for the abundances, except iron and silicon, as well as oxygen and sulphur when excluding HD 4539 (black data points). Especially HD 4539 shows differences compared to the other stars. It has the lowest T_{eff} among the pulsators, and it is also the one with the lowest surface gravity. Thus, this may be a cause for these large differences. Interestingly it shows always a higher abundance than the other pulsators except for oxygen and magnesium. Again, the iron abundance for all stars is at the solar level, showing that pulsations probably have no influence on this process. Other trends cannot be concluded from this figure.

Of special interest are the stars CD-35 15910 (dark green data points) and EPIC 211779126 (turquoise data points), having almost the same atmospheric parameters, only being separated by $T_{\text{eff}} = 500$ K. Their abundance pattern is almost identical for each element. These results are combined with the results from EC 14338-1445, a normal sdB candidate with no signs of pulsations, in Figure 8.4. The star is a twin star of EPIC 211779126, sharing the same atmospheric parameters, radius and mass. While both pulsating stars show almost the same abundance patterns, EC 14338-1445 shows large differences for elements like carbon, silicon and sulfur. This could be an indication that pulsations have an influence on the diffusion processes. However, because these three stars are the only candidates suitable for such studies based on the current sample, no real conclusion can be drawn and future studies are needed to see whether pulsations have an influence on diffusion.

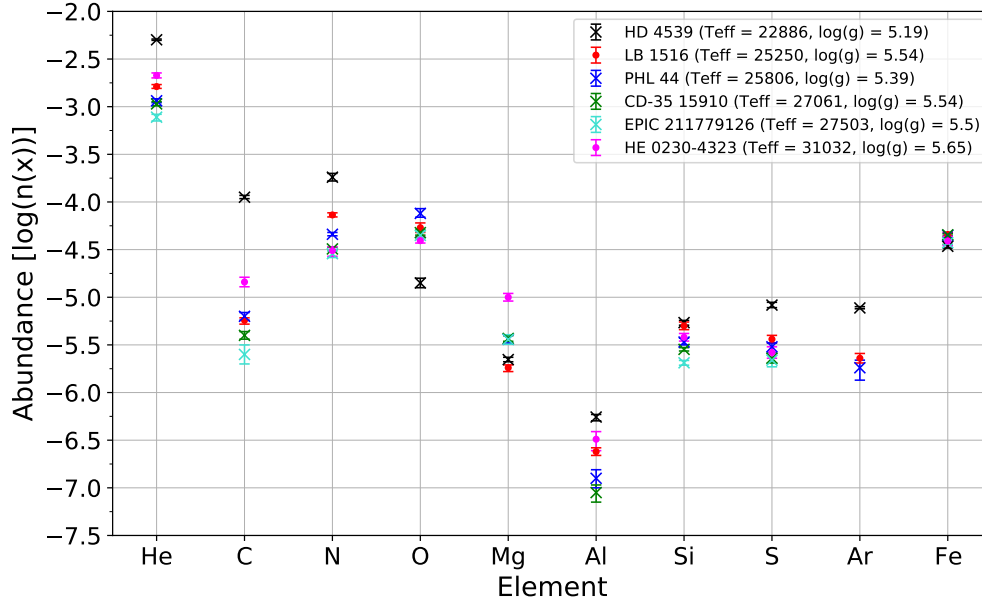


Figure 8.3: Elemental abundances of each pulsating star in the sample

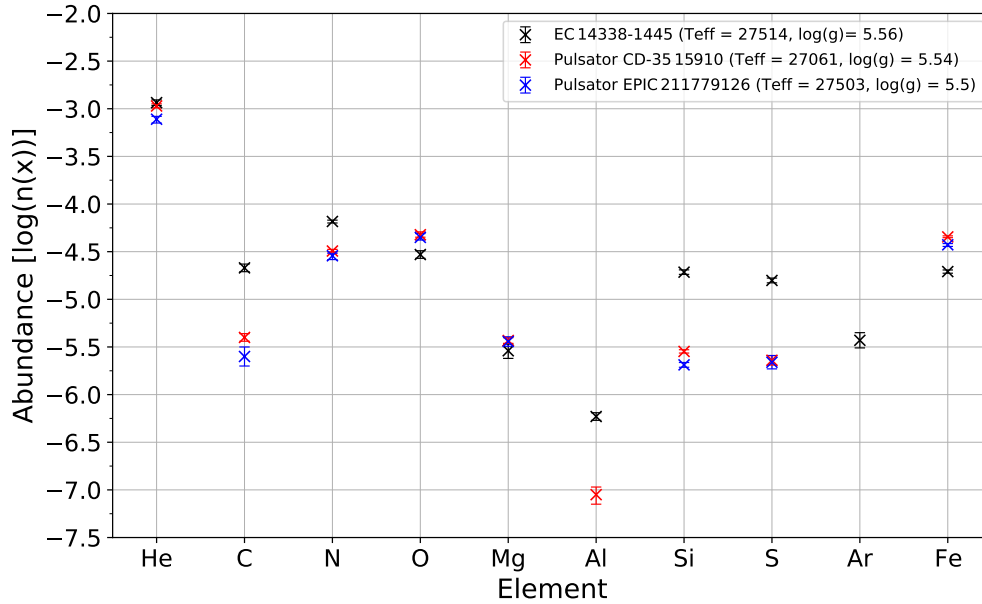


Figure 8.4: Elemental abundances of the two pulsating sdBs EPIC 211779126 and CD-35 15910 and the normal sdB EC 14338-1445.

8.3 Comparison to Michaud et al. 2011

The driver behind the unique abundance patterns are diffusion processes taking place in the star. These processes let some elements diffuse inwards, while other elements diffuse to the stars' surface, resulting in abundance anomalies at the star's surface. To predict how each element behaves with different effective temperature, surface gravity, metallicity and mass is part of current research.

The latest, state-of-the-art models are calculated by Michaud et al. (2011). They assume a mixing zone consisting of the outer $10^{-7.5}$ mass fraction of the star. This turbulent mixing zone is introduced with enough turbulence to create an abundance homogeneity in the zone. The models determine which abundance anomalies occur at the star's surface and cover about 35 million years, which corresponds to roughly one third of the star's lifetime on the EHB (Michaud et al. 2008, 2011).

Figure 8.5a shows model tracks describing the logarithmic mass fraction of iron with respect to the effective temperature. The first 10 million years are indicated by the dashed parts of the track. The models differ in mass, which is color coded but also indicated at each model individually. The mass is given with respect to the mass of the sun. Apart from that, there are two different sets of models, with different starting metallicities. The black and violet models have a starting metallicity of $z = 0.02$, which is close to the solar metallicity. The light blue and green models have a lower starting metallicity of $z = 0.004$. The red data points are the results from my analysis converted to mass fractions along with the corresponding uncertainties.

When looking at the different models, the first thing to be noticed is the different behaviour of the models with metallicity. The abundance of iron does not vary widely over the time period of the models with solar metallicity. In contrast the models with lower metallicity vary a lot more, up to 0.8 dex. It also becomes apparent that the time period of the models is still too short, because a lot of data points lie above the evolutionary model tracks, especially in the region of $22000 \text{ K} < T_{\text{eff}} < 28000 \text{ K}$. In contrast to that, stars with T_{eff} above 32000 K have an iron abundance which is lower than the predicted one by the lower metallicity models, far away from the solar metallicity models. One explanation for this would be that the stars have an even lower metallicity and are very close to the ZAEHB. In Figure 8.5b the logarithmic mass fraction of iron along with the same models like in Figure 8.5a is shown, but this time over the surface gravity. Again in red are the results from this analysis. For surface gravities below 5.6, the data points mostly lie above the model tracks, indicating again that the time period of the tracks needs to be increased well beyond 35 Myr. The iron abundance for stars with surface gravities larger than ≈ 5.7 is about 0.4 to 0.6 dex lower than for stars with surface gravities below 5.6. At surface gravities of 5.8, there are many data points right in between two models, which differ in mass by only $0.001 M_{\odot}$. This shows how sensitive the models are to this parameter. These data points also all seem to lie right at the beginning of the lower metallicity tracks, far away from the solar metallicity ones and cannot be accurately described by the models. The comparison of the other elements with the models from Michaud et al. (2011) are available in Figure 8.6 through Figure 8.14.

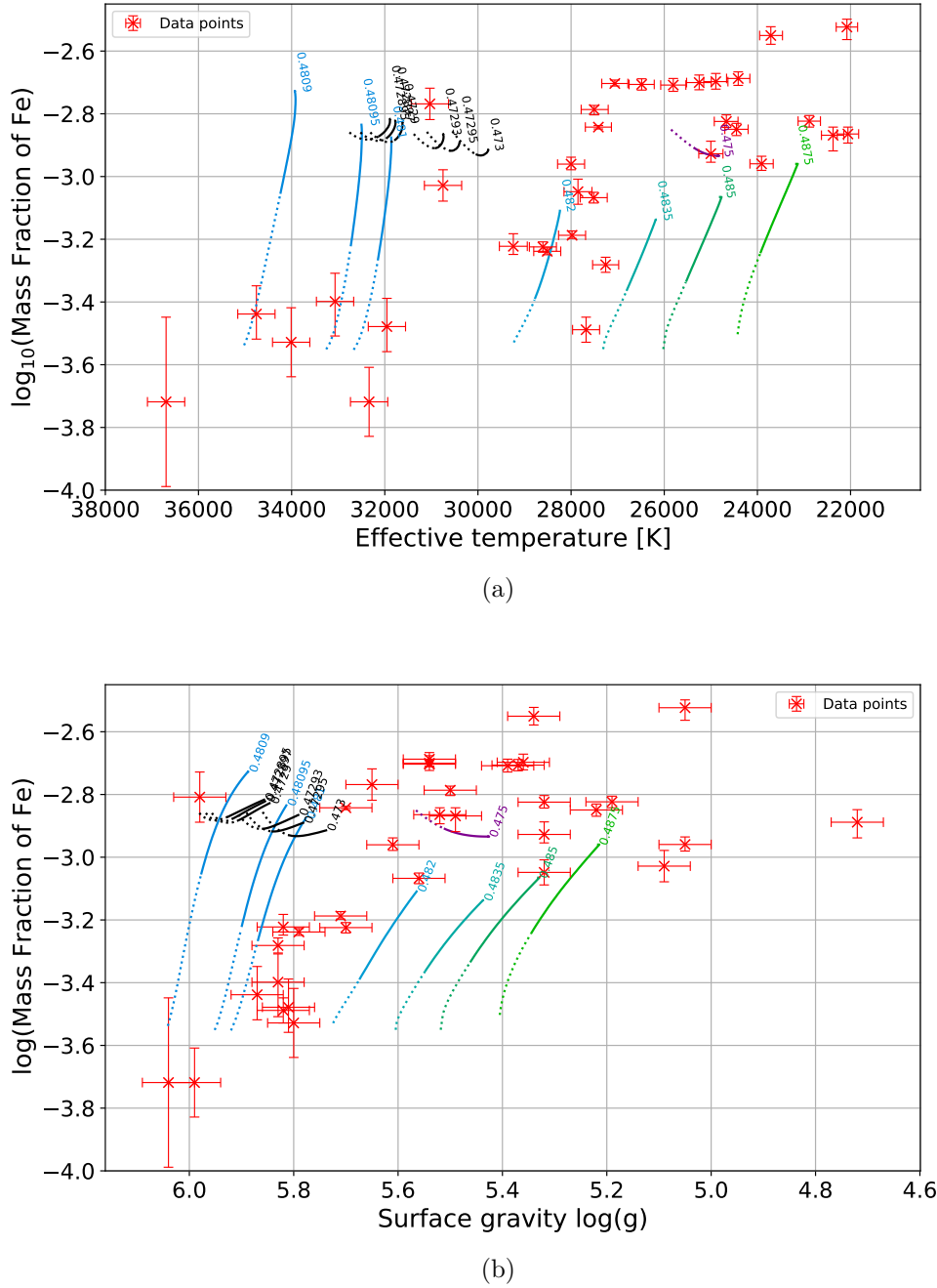
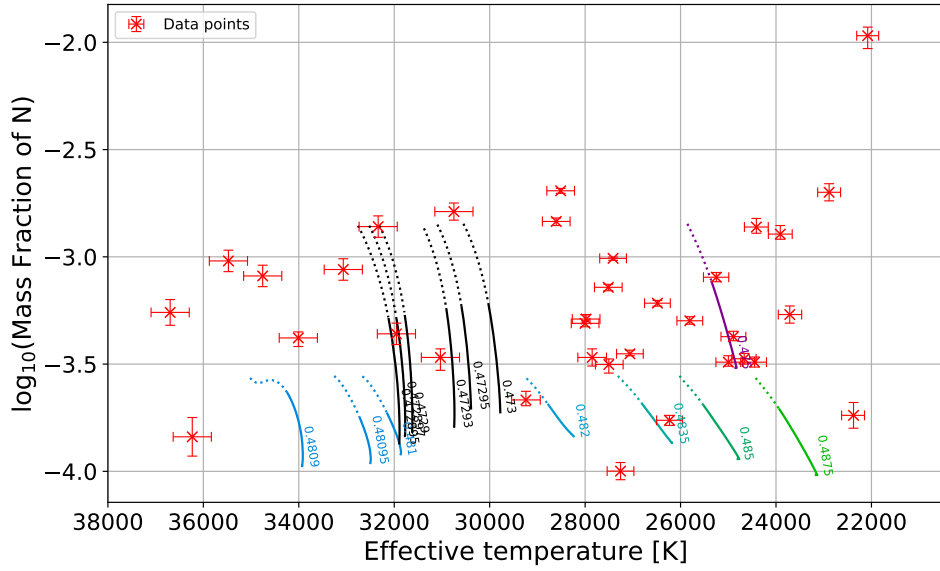
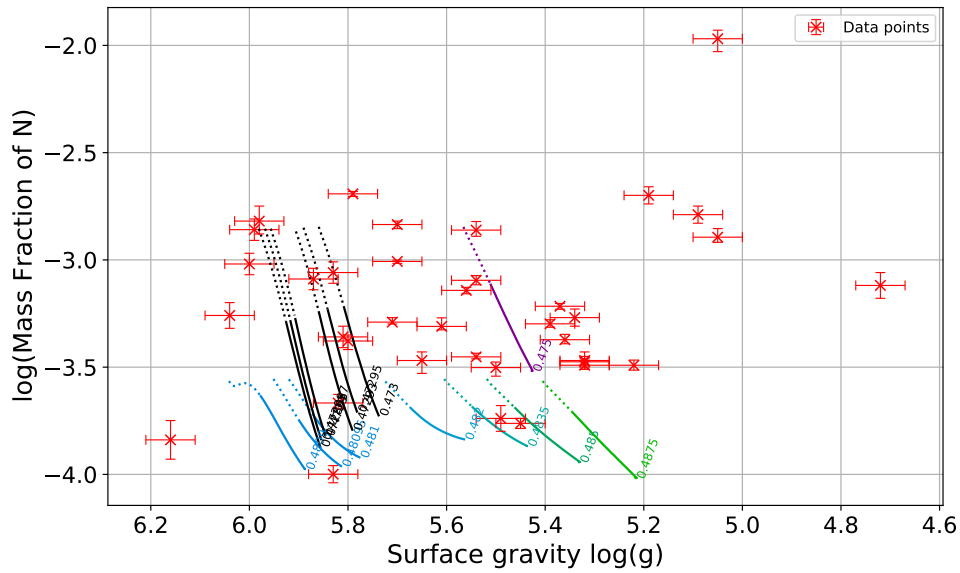


Figure 8.5: Logarithm of the mass fraction of iron over effective temperature (a), and over surface gravity (b). The models from Michaud et al. (2011) are color coded according to mass, which is also given on solar masses next to the lines. The light blue and light green models have a metallicity of $z = 0.004$, while the black and violet ones are having a almost solar metallicity of $z = 0.02$. In red are the results from my analysis.

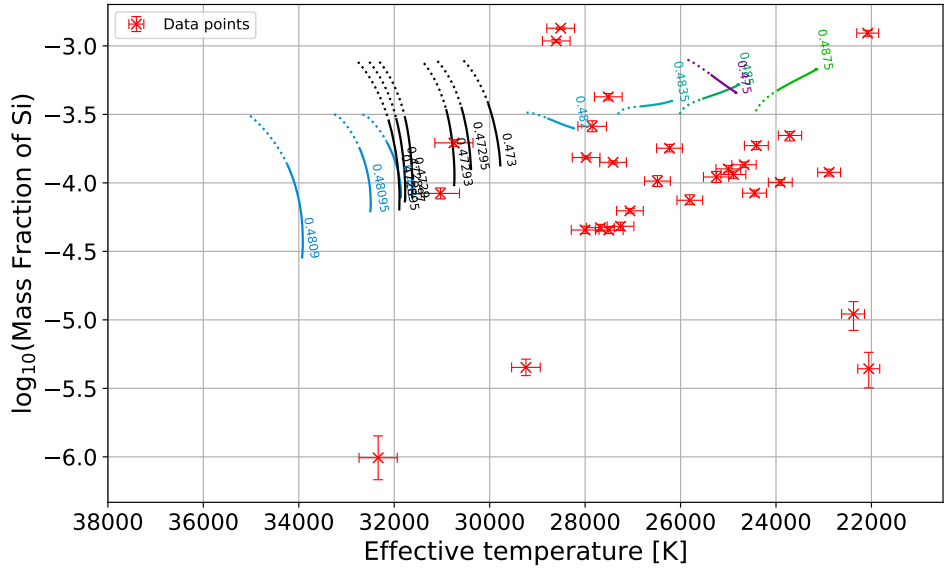


(a)

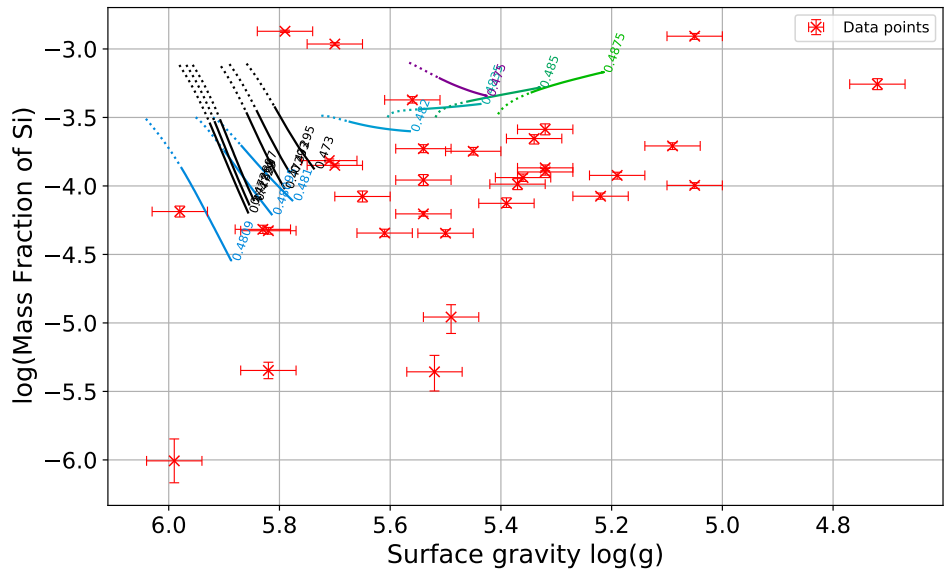


(b)

Figure 8.7: Same as in Figure 8.5 but this time for nitrogen.

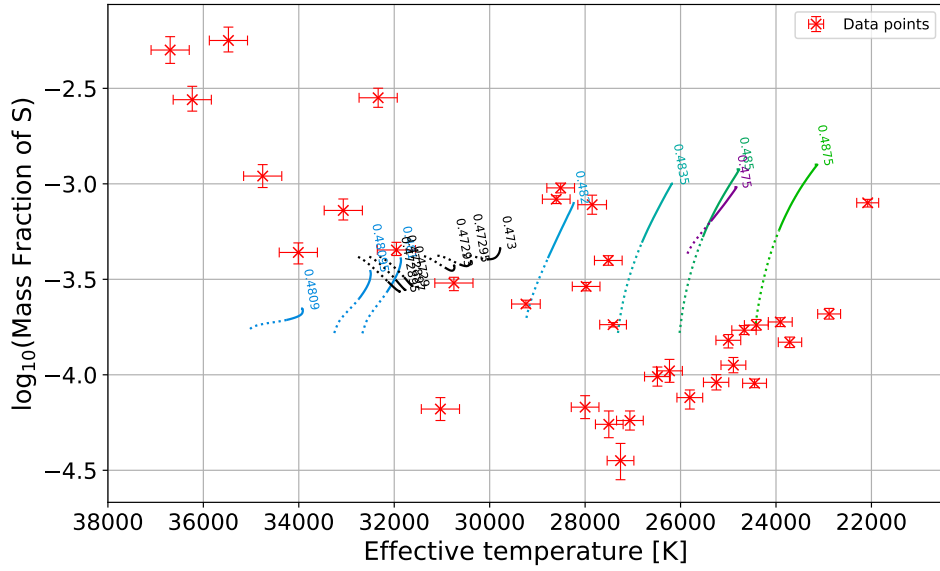


(a)

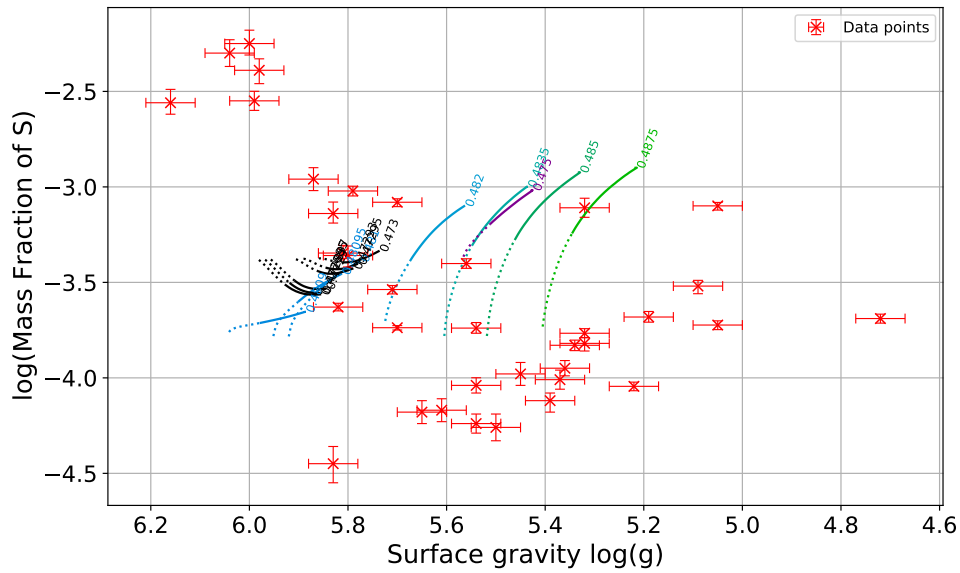


(b)

Figure 8.11: Same as in Figure 8.5 but this time for silicon.

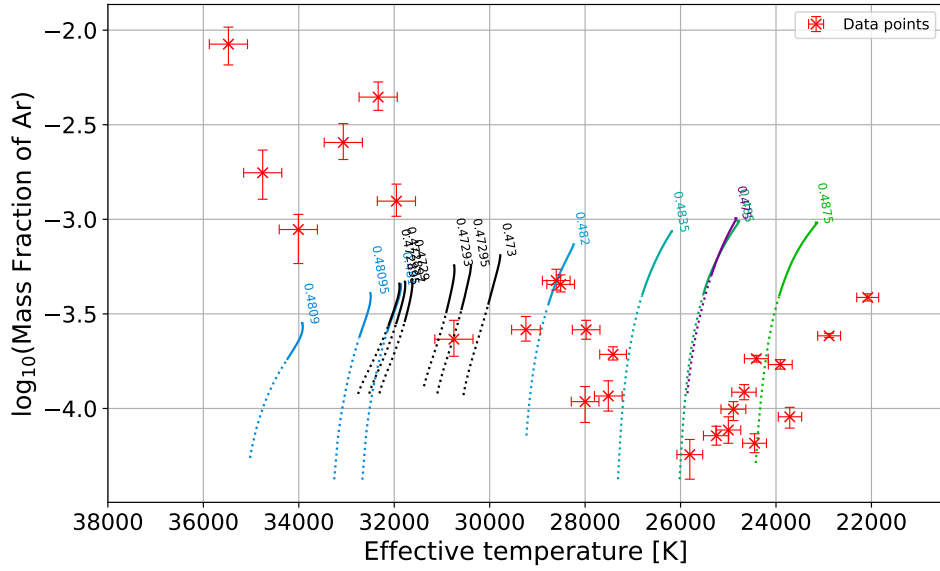


(a)

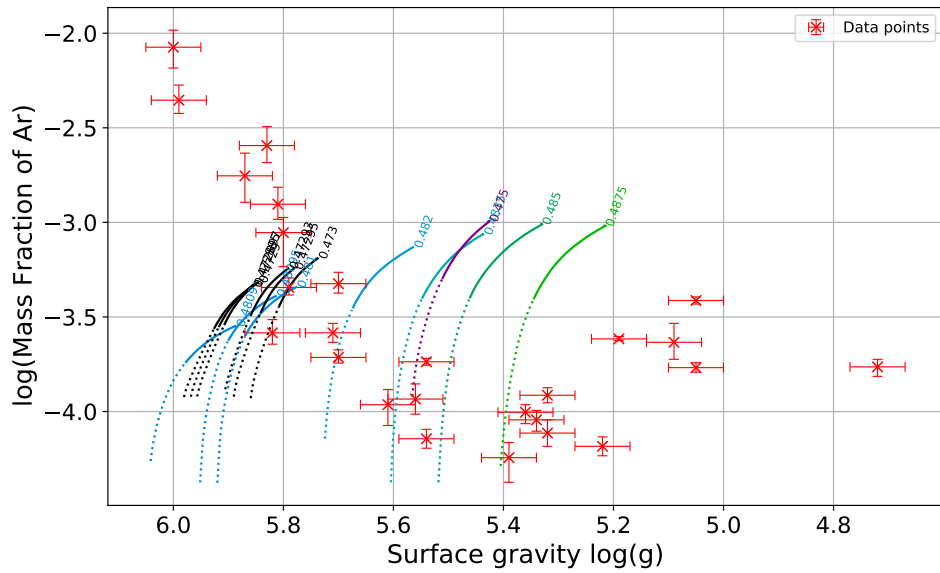


(b)

Figure 8.12: Same as in Figure 8.5 but this time for sulphur.

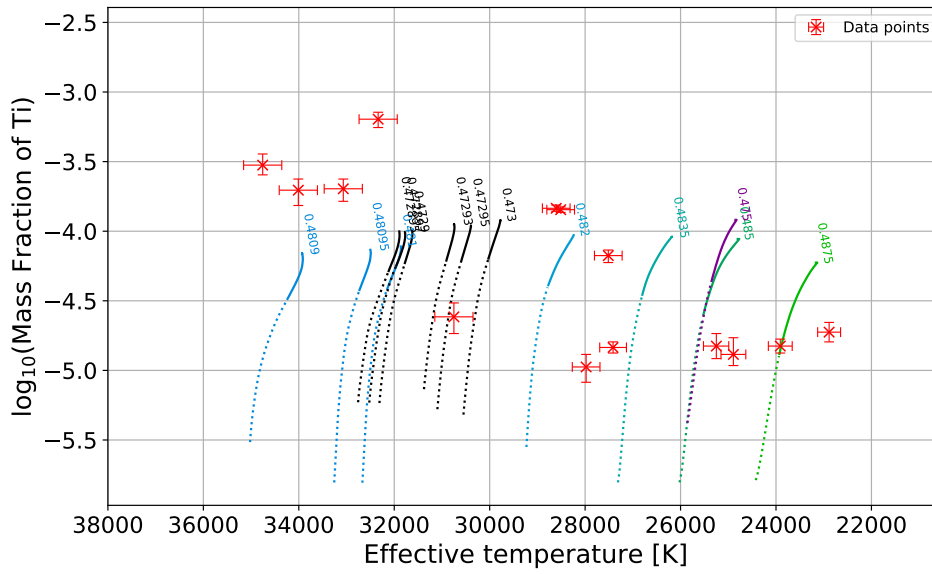


(a)

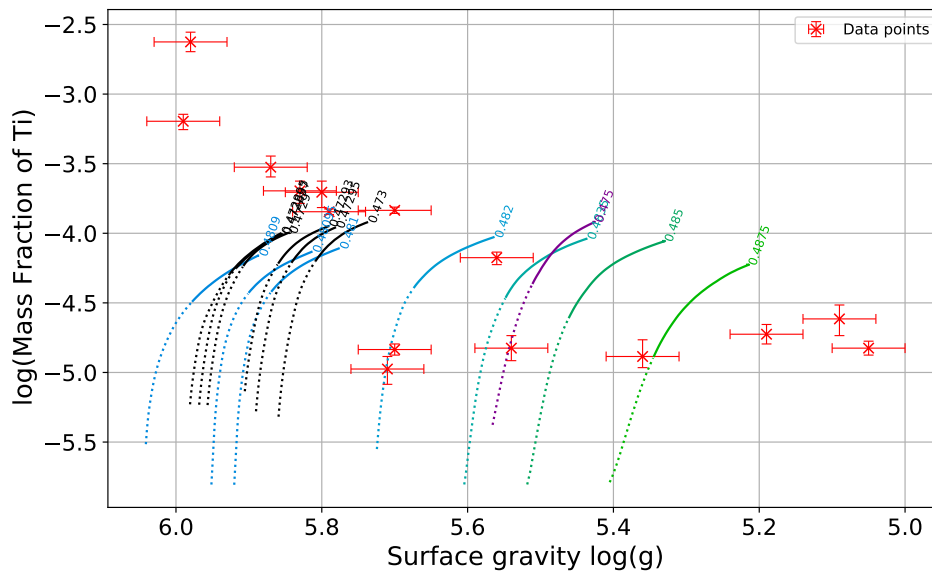


(b)

Figure 8.13: Same as in Figure 8.5 but this time for argon.



(a)



(b)

Figure 8.14: Same as in Figure 8.5 but this time for titanium.

To compare both atmospheric parameters to the models from Michaud et al. (2011), Figure 8.15 shows the Kiel diagram. The model tracks as well as the data points are color coded with the corresponding iron abundance in logarithmic mass fractions. Because the tracks only cover roughly one third of the stars' lifetime on the EHB, they are rather short in the Kiel Diagram. The ZAEHB and TAEHB are again taken from Dorman et al. (1993), like in Figure 6.6. While some data points are in agreement with the models, a lot of them lie beneath them. One can see that the start of the evolution on the EHB in the models from Michaud et al. (2011) is different, than the ZAEHB from Dorman et al. (1993). Therefore a lot of stars lie beneath the zero age of Michaud. Again a longer time span would greatly improve the comparisons.

Because the metallicity is a large factor in the models from Michaud et al. (2011), it is interesting to know if there are halo or thick disk stars among the sample stars. Stars in the halo and thick disk generally have a lower metallicity. Based on their kinematic parameters stars can be classified into halo, thick and thin disk stars. This is done in a so-called Toomre diagram, shown in Figure 8.16. There are three Galactic space velocities U , V and W . U is the velocity positive towards the Galactic center, V is positive in the direction of the Galactic rotation and W is the velocity positive towards the North Galactic Pole. The Toomre diagram shows three contours. The blue contour represents the thin disk distribution, the green contour the thick disk distribution and the grey contour marks the halo region of the Galaxy. The golden mark represents the position of the sun. Because all sample stars (black data points) lie within the blue contour, the probability is very high that all sample stars are thin disk stars. This indicates that the primordial metallicity of the sample stars should differ from solar by -0.7 and $+0.3$ dex (Bensby et al. 2014).

Another way to see whether the models are sufficient enough, is to look at the spread of abundances of the evolutionary tracks and compare it to the spread of my sample. Evolutionary tracks for each element are available in Figure 8.17 and Figure 8.18. The upper left panel of Figure 8.17 shows the evolution of the iron abundance over time. The iron abundance in the lower metallicity models is rising steadily, while the iron abundance in the solar metallicity models stays rather constant, only rising slightly over time. With this the spread of the models for each element can be determined by taking the total maximum and minimum value. The spread of the elemental abundances from this work are taken from Figure 8.5 through Figure 8.14. The comparison is done in Table 8.1.

For carbon, magnesium and iron, the results are in general in good agreement with the prediction from the models. The nitrogen models indicate that nitrogen only gets depleted from the stars surface over time, having the highest value right at the beginning, see Figure 8.17. This is in agreement with the derived abundances, except for one outlier which has a nitrogen abundance about 1 dex higher than predicted by the models.

Some results seem to be in disagreement like silicon. However, when looking at Figure 8.11 it becomes apparent that the resulting spread of my analysis is heavily influenced by four outliers, increasing the spread. When these outliers are not considered, the spread of the results from this analysis is in better agreement with the prediction of the models.

For other elements like argon or titanium, the highest abundance in the models is lower than the observed one. When looking at the time evolution of these elements in Figure 8.18, one can see that in both cases the abundance is rising over time. Therefore the time span of ≈ 35 Myr is not enough to explain the observed abundances, and the time span needs to be extended.

All in all, it can be said that the models partially fit well. However, the missing information about the starting metallicity of the sample stars makes a comparison complicated and there is still room improvement in many places.

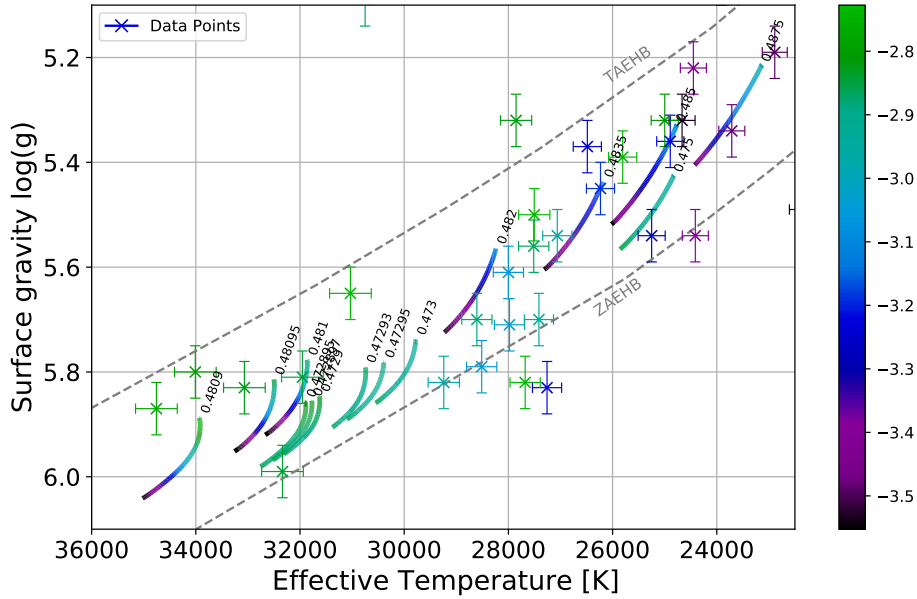


Figure 8.15: Atmospheric parameters compared to the models from Michaud et al. (2011). The tracks, as well as the data points, are color coded with corresponding iron abundance in mass fraction.

Element	Michaud et al. (2011) [dex]			This work [dex]		
	Highest	Lowest	Spread	Highest	Lowest	Spread
C	-2.53	-4.65	2.12	-2.62	-4.62	2.0
N	-2.84	-4.02	1.18	-1.95	-3.99	2.04
O	-2.03	-3.66	1.63	-2.61	-4.12	1.51
Mg	-3.14	-5.36	2.22	-3.05	-4.49	1.44
Al	-4.19	-6.32	2.13	-3.78	-6.0	2.22
Si	-3.10	-4.54	1.44	-2.86	-6.0	3.14
S	-2.89	-3.78	0.89	-2.22	-4.44	2.22
Ar	-2.99	-4.37	1.38	-2.07	-4.26	2.19
Fe	-2.73	-3.55	0.82	-2.50	-3.70	1.20
Ti	-3.95	-5.80	1.85	-2.61	-4.96	2.35

Table 8.1: Comparison of the elemental abundance spread between the models from Michaud et al. (2011) and this work. The models cover two metallicities: $z = 0.02$ and $z = 0.004$.

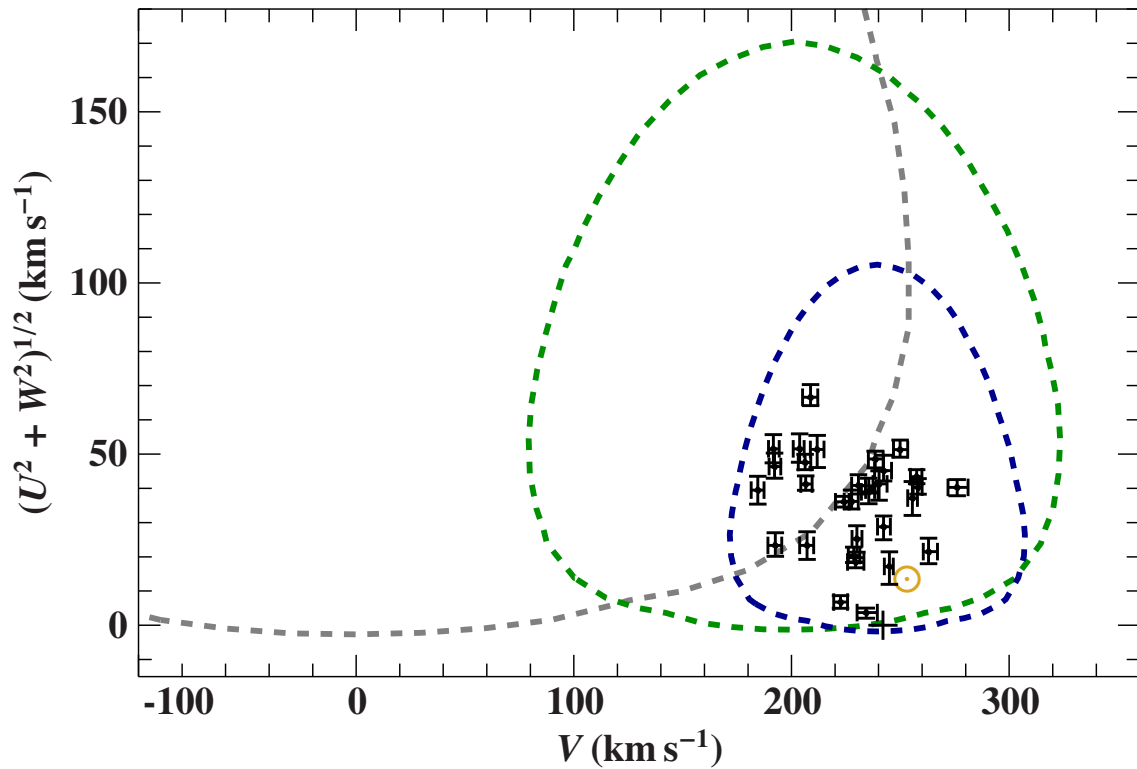


Figure 8.16: Toomre diagram of the sample stars. U , V and W are the three Galactic space velocities. The blue contour marks the thin disk distribution, the green contour the thick disk distribution and the grey contour the halo region of the Galaxy. The golden circle marks the position of the sun. The probability is high that all sample stars (black data points) are thin disk stars, because all of them lie within the blue contour.

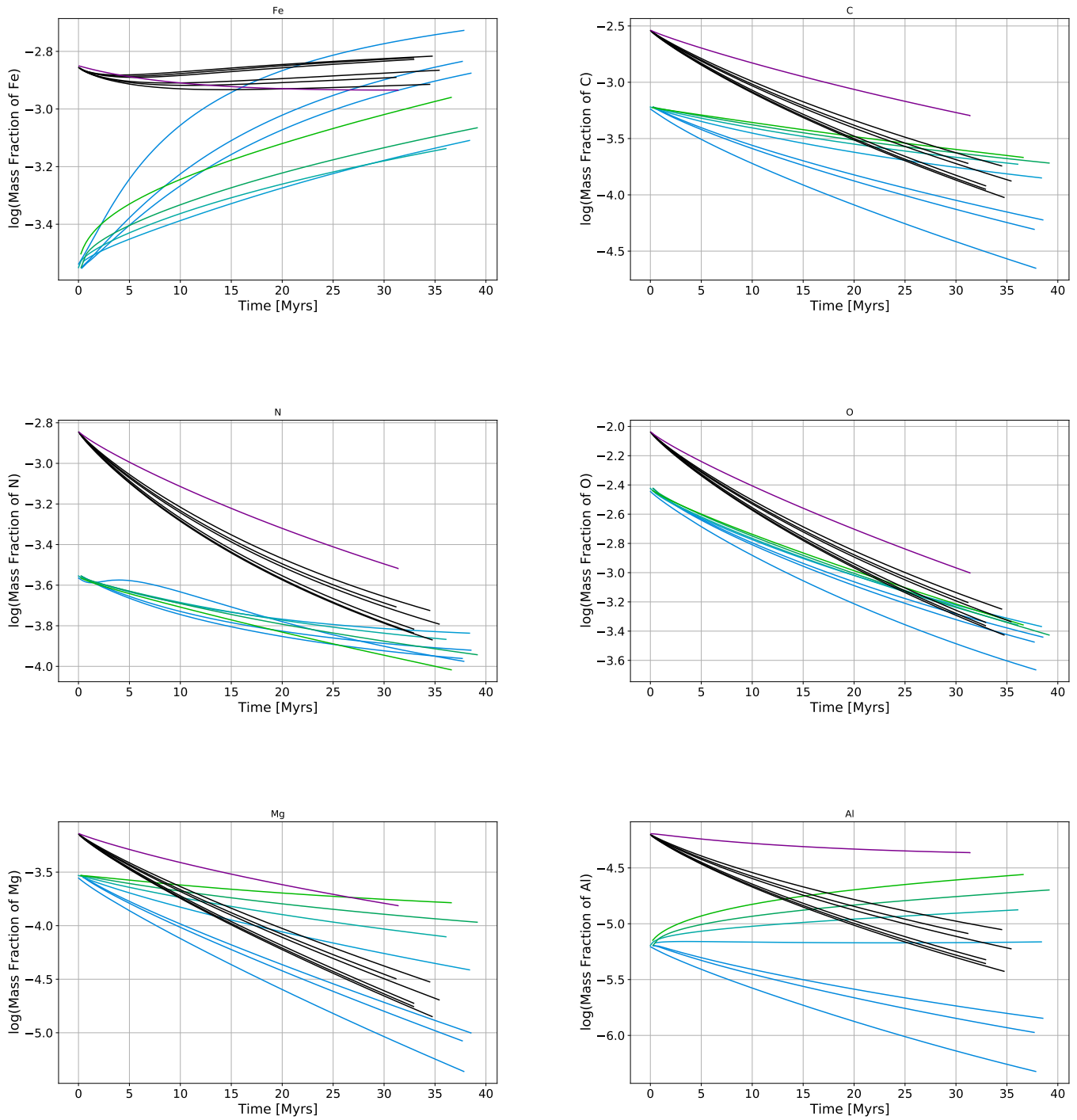


Figure 8.17: Evolutionary tracks for iron, carbon, nitrogen, oxygen, magnesium and aluminium (top left to bottom right). The light blue and light green models have a metallicity of $z = 0.004$, while the black and violet ones have an almost solar metallicity of $z = 0.02$.

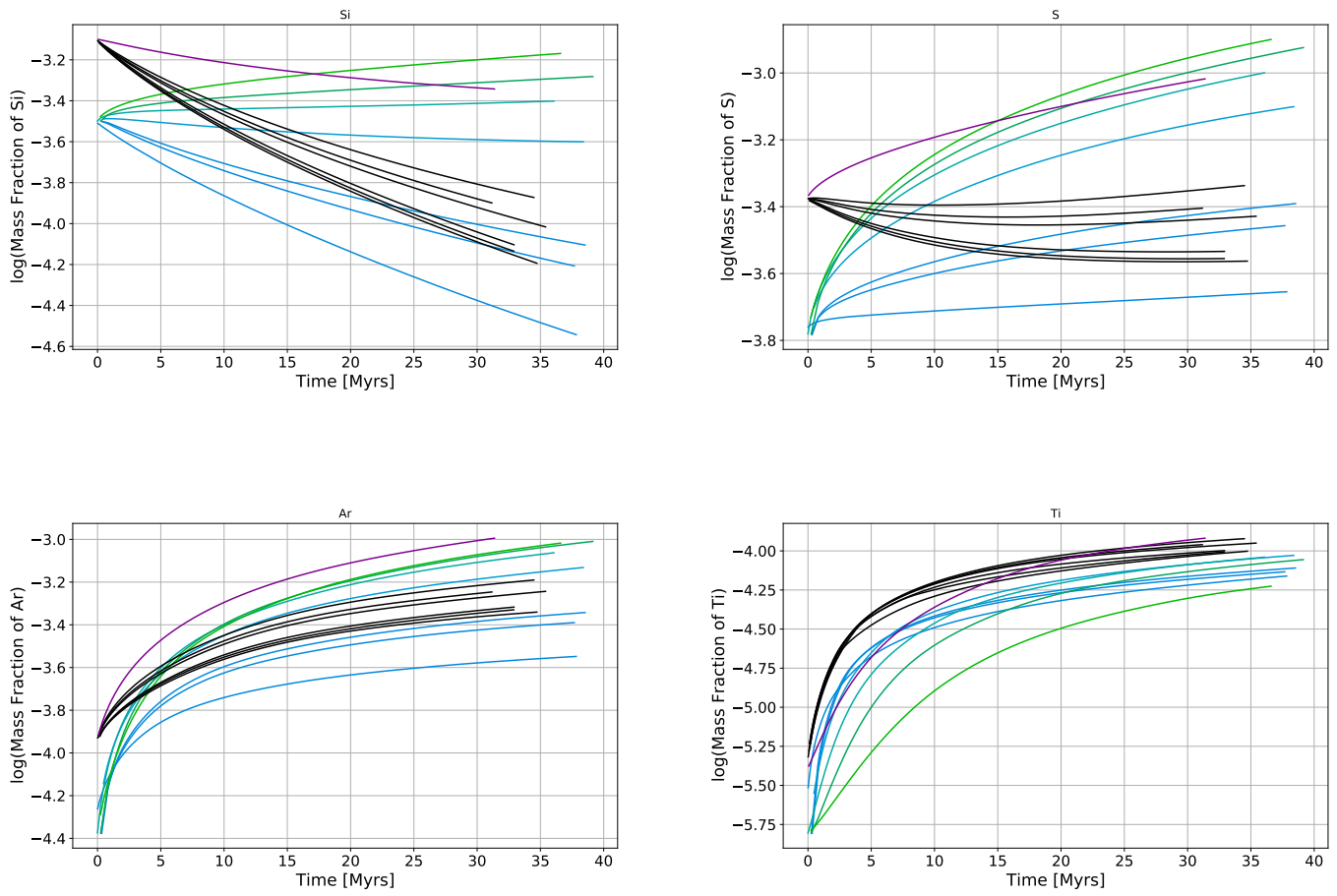


Figure 8.18: Same as Figure 8.17, but this time for silicon, sulphur, argon and titanium (top left to bottom right).

9 Summary and conclusion

Subdwarfs are immediate precursors of white dwarfs and thus close to the final stage in their evolution. After the red-giant phase, the stars have cast off their shell and only the helium core is remaining, with a small hydrogen envelope around it.

What makes sdBs of special interest, is that they allow us to study poorly understood diffusion processes, which cause peculiar abundance pattern at the star's surface, so that chemical elements may be over- or underabundant with respect to the Sun. Different models were developed to predict the different behaviour of elemental abundances in sdB stars. To better understand these diffusion processes and to test the latest state-of-the-art diffusion models, it is important to determine elemental abundances for many sdBs.

In this work 41 subdwarfs are analyzed and their atmospheric parameters, as well as elemental abundances are determined. To determine the elemental abundances, optical high resolution spectra are used.

For the modeling of the spectra, the codes ATLAS12, DETAIL and SURFACE are used to calculate state-of-the-art models, also considering non-local thermal equilibrium (NLTE) effects for the elements: H, He, C, N, O, Mg, Ne, Mg, Al, Si, S, Ar and Fe. Other elements considered in the analysis are: Ca, Ti, Cr, P, Mn, Co, Sr, V. These elements are considered in local thermal equilibrium (LTE). Unlike previous studies, for the analysis an objective, χ^2 -base spectroscopic analysis technique (Irrgang et al. 2014) was employed, which makes use of all spectral features available, rather than using pre-selected lines.

I determined effective temperature T_{eff} , surface gravity $\log(g)$ and helium abundance $\log(n(\text{He}))$ for all 41 subdwarfs, along with their respective elemental abundances. Angular diameters and interstellar extinctions were derived from a photometric analysis. Making use of trigonometric distances from the *Gaia* mission, the masses, radii and luminosities were determined. By plotting the atmospheric parameters in the Kiel diagram ($\log(g)$ over T_{eff}) and in the Hertzsprung-Russell diagram (Luminosity over T_{eff}), the sample is compared to stellar evolution models for the extreme horizontal branch (EHB). This leads to the conclusion that all but one star lie on the EHB. The latter has already evolved away from the EHB (see Sec. 6).

While analysing the sample, I uncovered a potential problem with the silicon model atom described in Sec. 7. Stars with $22000 \text{ K} < T_{\text{eff}} < 26000 \text{ K}$ have Si II-lines always being stronger than the actual observation, while their Si III-lines are reproduced. For hotter stars observed Si II- and Si III-lines are consistently reproduced by the synthetic spectra. The model atom probably needs some improvements and needs to be revised to fix this issue.

Twenty two stars of my sample were also analyzed by Geier (2013) using a semi-automatic procedure and a rather limited list of spectral lines and LTE synthetic spectra. Consequently, the uncertainties of the resulting abundances were limited to about 0.3 dex. The abundances derived in this work are much more accurate, typically 0.05 dex.

To see how the results match, a comparison between the determined effective temperatures and elemental abundances is made in Sec. 8. It becomes apparent that the determined effective temperatures are in good agreement, indicating that NLTE effects do not have a large influence on this atmospheric parameter. In general the elemental abundances are consistent with those of Geier (2013) given the larger uncertainties of the latter study, but also revealing systematic trends for some elemental abundances compared to the results from Geier (2013).

Six subdwarf stars in the sample are multi-mode pulsators. To see if and how pulsations have an influence on diffusion processes a triple of stars was found, having almost the same T_{eff} differing by ± 500 K and $\log(g) \pm 0.05$ only. Two stars in the triplet are known pulsators, showing almost the same elemental abundances, while the third star is not pulsating and shows a different abundance pattern. However, this is the only group of stars that can be analyzed in this way. Therefore, further studies are needed to show whether and how pulsations influence the diffusion process.

The accurate abundance pattern derived in this work are considered a benchmark to model predictions. Therefore, the results of this analysis are compared to the latest state-of-the-art diffusion models by Michaud et al. (2011) in Sec. 8.3. These models cover the evolution of many elements for roughly the first third of the star's lifetime on the EHB ($t = 35$ Myr). It becomes apparent that the primordial metallicity of the stars plays a huge role in the evolution of the elemental abundances. However, this parameter is unknown for the sample stars, which renders conclusions difficult. To get an idea of the primordial metallicity, the kinematics of the stars were analyzed, separating the stars of the metal poor (thick disk and halo) populations from the those of the thin disk. All stars seem to be thin disk stars, indicating that their primordial metallicity should differ from solar by -0.7 and $+0.3$ dex (Bensby et al. 2014), only. While some parts of the results are in agreement with the models, there are still open questions regarding the covered time span of the diffusion models as well as the metallicity of the stars.

The homogeneous and comprehensive analysis in this work provides atmospheric parameters and elemental abundances of unprecedented precision and accuracy for 41 stars in a temperature range from 19000 K to 36000 K. The analysis considers NLTE effects for most of the elements, while also considering all available spectral lines in the optical range. This sample can be used as a benchmark to improve future diffusion models and help to better understand the processes taking place within the sdBs.

References

- Ahn, C. P., Alexandroff, R., Allende Prieto, C. et al., The Ninth Data Release of the Sloan Digital Sky Survey: First Spectroscopic Data from the SDSS-III Baryon Oscillation Spectroscopic Survey. 2012, *ApJS*, 203, 21
- Becker, S. R. 1998, in *Astronomical Society of the Pacific Conference Series*, Vol. 131, *Properties of Hot Luminous Stars*, ed. I. Howarth, 137
- Becker, S. R. & Butler, K., Non-LTE line formation in early B and late O stars. I. Singly ionized oxygen. 1988, *A&A*, 201, 232
- Bensby, T., Feltzing, S. & Oey, M. S., Exploring the Milky Way stellar disk. A detailed elemental abundance study of 714 F and G dwarf stars in the solar neighbourhood. 2014, *A&A*, 562, A71
- Bevington, P. R. & Robinson, D. K. 1992, *Data reduction and error analysis for the physical sciences*
- Castelli, F., ATLAS12: how to use it. 2005, *Memorie della Societa Astronomica Italiana Supplementi*, 8, 25
- Chambers, K. C., Magnier, E. A., Metcalfe, N. et al. 2019, *The Pan-STARRS1 Surveys*
- Copperwheat, C. M., Morales-Rueda, L., Marsh, T. R. et al., Radial-velocity measurements of subdwarf B stars. 2011, *MNRAS*, 415, 1381
- DENIS Consortium, VizieR Online Data Catalog: The DENIS database (DENIS Consortium, 2005). 2005, *VizieR Online Data Catalog*, II/263
- Dorman, B., Rood, R. T. & O'Connell, R. W., Ultraviolet Radiation from Evolved Stellar Populations. I. Models. 1993, *ApJ*, 419, 596
- Dorsch, M., Latour, M. & Heber, U., Heavy metals in intermediate He-rich hot subdwarfs: the chemical composition of HZ 44 and HD 127493. 2019, *A&A*, 630, A130
- Dye, S., Warren, S. J., Hambly, N. C. et al., The UKIRT Infrared Deep Sky Survey Early Data Release. 2006, *Monthly Notices of the Royal Astronomical Society*, 372, 1227 [LINK]
- ESO. 2021a, ESO - Data, [Online; accessed 11-June-2021] [LINK]
- ESO. 2021b, ESO - Phase 3, [Online; accessed 18-May-2021] [LINK]
- Fitzpatrick, E. L., Massa, D., Gordon, K. D. et al., An Analysis of the Shapes of Interstellar Extinction Curves. VII. Milky Way Spectrophotometric Optical-through-ultraviolet Extinction and Its R-dependence. 2019, *ApJ*, 886, 108
- Fontaine, G., Green, E., Brassard, P. et al. 2014, in *Astronomical Society of the Pacific Conference Series*, Vol. 481, *6th Meeting on Hot Subdwarf Stars and Related Objects*, ed. V. van Grootel, E. Green, G. Fontaine, & S. Charpinet, 83

- Gaia Collaboration, Brown, A. G. A., Vallenari, A. et al., Gaia Early Data Release 3: Summary of the contents and survey properties. 2020, arXiv e-prints, arXiv:2012.01533
- Gaia Collaboration, Prusti, T., de Bruijne, J. H. J. et al., The Gaia mission. 2016, *A&A*, 595, A1
- Geier, S., Hot subdwarf stars in close-up view. III. Metal abundances of subdwarf B stars. 2013, *A&A*, 549, A110
- Geier, S., Heber, U., Edelmann, H. et al., Metal abundances of subdwarf B stars—the extended sample. 2010, *Ap&SS*, 329, 127
- Geier, S., Heber, U. & Napiwotzki, R. 2008, in *Astronomical Society of the Pacific Conference Series*, Vol. 392, *Hot Subdwarf Stars and Related Objects*, ed. U. Heber, C. S. Jeffery, & R. Napiwotzki, 159
- Geier, S., Østensen, R. H., Nemeth, P. et al., The population of hot subdwarf stars studied with Gaia. I. The catalog of known hot subdwarf stars. 2017, *A&A*, 600, A50
- Geier, S., Raddi, R., Gentile Fusillo, N. P. et al., The population of hot subdwarf stars studied with Gaia. II. The Gaia DR2 catalogue of hot subluminoous stars. 2019, *A&A*, 621, A38
- Giddings, J. R. 1981, PhD thesis, University of London
- Greenstein, G. S., Helium Deficiency in Old Halo B Stars. 1967, *Nature*, 213, 871
- Harris, C. R., Millman, K. J., van der Walt, S. J. et al., Array programming with NumPy. 2020, *Nature*, 585, 357 [LINK]
- Heber, U., Hot Subluminoous Stars. 2016, *PASP*, 128, 082001
- Heber, U., Edelmann, H., Lisker, T. et al., Discovery of a helium-core white dwarf progenitor. 2003, *A&A*, 411, L477
- Heber, U., Irrgang, A. & Schaffenroth, J., Spectral energy distributions and colours of hot subluminoous stars. 2018, *Open Astronomy*, 27, 35
- Høg, E., Fabricius, C., Makarov, V. V. et al., The Tycho-2 catalogue of the 2.5 million brightest stars. 2000, *A&A*, 355, L27
- Houck, J. C. & Denicola, L. A. 2000a, in *Astronomical Society of the Pacific Conference Series*, Vol. 216, *Astronomical Data Analysis Software and Systems IX*, ed. N. Manset, C. Veillet, & D. Crabtree, 591
- Houck, J. C. & Denicola, L. A. 2000b, in *Astronomical Society of the Pacific Conference Series*, Vol. 216, *Astronomical Data Analysis Software and Systems IX*, ed. N. Manset, C. Veillet, & D. Crabtree, 591
- Hunter, J. D., Matplotlib: A 2D graphics environment. 2007, *Computing In Science & Engineering*, 9, 90

- Hämmerich, S. 2020, Master's thesis, Friedrich-Alexander-Universität Erlangen-Nürnberg
- Irrgang, A. 2014, PhD thesis, Friedrich-Alexander-Universität Erlangen-Nürnberg
- Irrgang, A., Kreuzer, S., Heber, U. et al., A quantitative spectral analysis of 14 hypervelocity stars from the MMT survey. 2018, *A&A*, 615, L5
- Irrgang, A., Przybilla, N., Heber, U. et al., A new method for an objective, χ^2 -based spectroscopic analysis of early-type stars. First results from its application to single and binary B- and late O-type stars. 2014, *A&A*, 565, A63
- Kaufer, A., Stahl, O., Tubbesing, S. et al., Commissioning FEROS, the new high-resolution spectrograph at La-Silla. 1999, *The Messenger*, 95, 8
- Kurucz, R., ATLAS9 Stellar Atmosphere Programs and 2 km/s grid. 1993, ATLAS9 Stellar Atmosphere Programs and 2 km/s grid. Kurucz CD-ROM No. 13. Cambridge, 13
- Kurucz, R. L. 1996, in *Astronomical Society of the Pacific Conference Series*, Vol. 108, M.A.S.S., Model Atmospheres and Spectrum Synthesis, ed. S. J. Adelman, F. Kupka, & W. W. Weiss, 160
- Lindgren, L., Klioner, S. A., Hernández, J. et al., Gaia Early Data Release 3: The astrometric solution. 2020, arXiv e-prints, arXiv:2012.03380
- Lynn, B. B., Keenan, F. P., Dufton, P. L. et al., Early-type stars in the Galactic halo from the Palomar-Green survey-III. Completion of a magnitude range limited sample. 2004, *MNRAS*, 349, 821
- Magee, H. R. M., Dufton, P. L., Keenan, F. P. et al., Model atmosphere and kinematical analyses of early-type stars from the Edinburgh-Cape Survey. 2001, *MNRAS*, 324, 747
- McKinney, W. 2010, in *Proceedings of the 9th Python in Science Conference*, Vol. 445, Austin, TX, 51–56
- McKinney, W., pandas: a foundational Python library for data analysis and statistics. 2011, *Python for High Performance and Scientific Computing*, 14
- McMahon, R., G., Banerji et al., VizieR Online Data Catalog: The VISTA Hemisphere Survey (VHS) catalog DR4.1 (McMahon+, 2013). 2019, *VizieR Online Data Catalog*, II/359
- Mermilliod, J. C., VizieR Online Data Catalog: Homogeneous Means in the UBV System (Mermilliod 1991). 2006, *VizieR Online Data Catalog*, II/168
- Michaud, G., Richer, J. & Richard, O., Abundance Anomalies in Horizontal Branch Stars and Atomic Diffusion. 2008, *ApJ*, 675, 1223
- Michaud, G., Richer, J. & Richard, O., Horizontal branch evolution, metallicity, and sdB stars. 2011, *A&A*, 529, A60

- Morel, T. & Butler, K., The neon content of nearby B-type stars and its implications for the solar model problem. 2008, *A&A*, 487, 307
- Morel, T., Butler, K., Aerts, C. et al., Abundance analysis of prime B-type targets for asteroseismology. I. Nitrogen excess in slowly-rotating β Cephei stars. 2006, *A&A*, 457, 651
- Napiwotzki, R., Christlieb, N., Drechsel, H. et al., Search for progenitors of supernovae type Ia with SPY. 2001, *Astronomische Nachrichten*, 322, 411
- Naslim, N., Jeffery, C. S., Hibbert, A. et al., Discovery of extremely lead-rich subdwarfs: does heavy metal signal the formation of subdwarf B stars? 2013, *MNRAS*, 434, 1920
- Nieva, M. F. & Przybilla, N., C II Abundances in Early-Type Stars: Solution to a Notorious Non-LTE Problem. 2006, *ApJ*, 639, L39
- Nieva, M. F. & Przybilla, N., Hydrogen and helium line formation in OB dwarfs and giants. A hybrid non-LTE approach. 2007, *A&A*, 467, 295
- Nieva, M. F. & Przybilla, N., Carbon abundances of early B-type stars in the solar vicinity. Non-LTE line-formation for C II/III/IV and self-consistent atmospheric parameters. 2008, *A&A*, 481, 199
- Nieva, M. F. & Przybilla, N., Present-day cosmic abundances. A comprehensive study of nearby early B-type stars and implications for stellar and Galactic evolution and interstellar dust models. 2012, *A&A*, 539, A143
- Onken, C. A., Wolf, C., Bessell, M. S. et al., SkyMapper Southern Survey: Second data release (DR2). 2019, *PASA*, 36, e033
- Paunzen, E., A new catalogue of Strömgren-Crawford uvbytomety. 2015, *A&A*, 580, A23 [LINK]
- Powell, M. J. D., An efficient method for finding the minimum of a function of several variables without calculating derivatives. 1964, *The Computer Journal*, 7, 155 [LINK]
- Przybilla, N., Non-LTE modelling of the He I 10830 Å line in early-type main sequence stars. 2005, *A&A*, 443, 293
- Przybilla, N. & Butler, K., Non-LTE line formation for N: Abundances and stellar parameters. Model atom and first results on BA-type stars. 2001, *A&A*, 379, 955
- Przybilla, N. & Butler, K., Non-LTE Line Formation for Hydrogen Revisited. 2004, *ApJ*, 609, 1181
- Przybilla, N., Butler, K., Becker, S. R. et al., Non-LTE line formation for $\text{Mg}\{\text{I/II}\}$ Abundances and stellar parameters. Model atom and first results on A-type stars. 2001, *A&A*, 369, 1009
- Przybilla, N., Butler, K., Becker, S. R. et al., Quantitative spectroscopy of BA-type supergiants. 2006, *A&A*, 445, 1099

- Przybilla, N., Butler, K., Becker, S. R. et al., Non-LTE line formation for neutral oxygen. Model atom and first results on A-type stars. 2000, *A&A*, 359, 1085
- Schaffenroth, J. 2016, Master's thesis, Friedrich-Alexander-Universität Erlangen-Nürnberg
- Schindewolf, M., Németh, P., Heber, U. et al., A quantitative NLTE analysis of visual and ultraviolet spectra of four helium-rich subdwarf O stars. 2018, *A&A*, 620, A36
- Schneider, D., Irrgang, A., Heber, U. et al., NLTE spectroscopic analysis of the ^3He anomaly in subluminous B-type stars. 2018, *A&A*, 618, A86
- Shanks, T., Metcalfe, N., Chehade, B. et al., The VLT Survey Telescope ATLAS. 2015, *MNRAS*, 451, 4238
- Silva, M. D. V. & Napiwotzki, R., Ejection velocities of high Galactic latitude runaway stars. 2011, *MNRAS*, 411, 2596
- Skrutskie, M. F., Cutri, R. M., Stiening, R. et al., The Two Micron All Sky Survey (2MASS). 2006, *AJ*, 131, 1163
- van Leeuwen, F., Validation of the new Hipparcos reduction. 2007, *A&A*, 474, 653
- Vrancken, M., Butler, K. & Becker, S. R., Non-LTE line formation for SII and SIII. I. Model atoms and first results. 1996, *A&A*, 311, 661
- Wamsteker, W. 2000, The IUE newly extracted spectra system
- Wolf, C., Golding, J., Hon, W. J. et al., SkyMapper colours of Seyfert galaxies and Changing-Look AGN. 2020, *Monthly Notices of the Royal Astronomical Society*, 499, 1005–1022 [LINK]
- Wright, E. L., Eisenhardt, P. R. M., Mainzer, A. K. et al., The Wide-field Infrared Survey Explorer (WISE): Mission Description and Initial On-orbit Performance. 2010, *AJ*, 140, 1868
- Zangwill, W. I., Minimizing a function without calculating derivatives. 1967, *The Computer Journal*, 10, 293 [LINK]

Acknowledgments

Part 1: Data, software and services

Based on data obtained from the ESO Science Archive Facility under request number MasterLars#543705. These data products have been processed by the Cambridge Astronomy Survey Unit (CASU) at the Institute of Astronomy, University of Cambridge, and by the FLAMES/UVES reduction team at INAF/Osservatorio Astrofisico di Arcetri. These data have been obtained from the Gaia-ESO Survey Data Archive, prepared and hosted by the Wide Field Astronomy Unit, Institute for Astronomy, University of Edinburgh, which is funded by the UK Science and Technology Facilities Council. This research has made use of the SIMBAD database, operated at CDS, Strasbourg, France. This research has made use of NASA's Astrophysics Data System. This research has made use of the VizieR catalogue access tool, CDS, Strasbourg, France. This research made use of matplotlib, a Python library for publication quality graphics (Hunter 2007). This research made use of NumPy (Harris et al. 2020). This research made use of ISIS to perform spectral fitting (Houck & Denicola 2000b) This research made use of pandas (McKinney 2010, 2011). This work has made use of data from the European Space Agency (ESA) mission *Gaia* (<https://www.cosmos.esa.int/gaia>), processed by the *Gaia* Data Processing and Analysis Consortium (DPAC, <https://www.cosmos.esa.int/web/gaia/dpac/consortium>). Funding for the DPAC has been provided by national institutions, in particular the institutions participating in the *Gaia* Multilateral Agreement. Parts of the acknowledgements were compiled using the Astronomy Acknowledgement Generator.

Part 2: The true acknowledgments

First of all I like to thank Prof. Dr. Ulrich Heber and Dr. Andreas Irrgang to give me the opportunity to write my master's thesis at the Karl-Remeis-Sternwarte and providing me with this interesting topic. I also want to thank them for all the constructive discussions, as well as their answers to all my questions. I really enjoyed working on this thesis.

A special thanks to Andreas for providing and explaining all the different ISIS scripts as well as helping me to improve my own scripts.

Another special thanks to Georges Michaud and Jacques Richer for providing me with their model data and allow me to use them in this analysis.

Thank you Steven for helping me with any problem regarding computer stuff or other issues. It was always a pleasure to discuss and talk with you.

I want to thank Matti, Markus, David and Simon for helping me with all kinds of computer stuff and always having an open ear for my problems and complains.

Even though I did not get to spent so much time in Bamberg due to Corona, I want to thank Jonathan, David, Steven and Sarah. We could not spent much time in the Drechsel Room together but I really enjoyed the meetings either via zoom or in person.

Thank you to all the admins at the Sternwarte to keep the cluster up and running, as well as providing great solutions for the home-office.

I'd like to thank Dirk Sander for the helpful discussion and tips on my thesis.

Thank you to my family and friends who have always supported and helped me.

As we say in the Drechsel-Room: "That was!"

Appendix

Spectroscopic results

Table 9.1: First half of the results from the spectroscopic analysis.

All abundances are given as $\frac{n}{n_{\text{H}}}$.
The uncertainties are 1σ uncertainties, including statistical uncertainties and systematical uncertainties of 1% in T_{eff} and 0.05 dex in $\log(g)$.

#	Star name	T_{eff} [K]	$\log(g)$ [cgs]	$\log(\text{He})$ [dex]	$\log(\text{C})$ [dex]	$\log(\text{N})$ [dex]	$\log(\text{O})$ [dex]
1	EC 03568-4849	19636.7^{+220}_{-210}	4.72 ± 0.05	$-2.013^{+0.05}_{-0.026}$	-4.65 ± 0.05	-4.16 ± 0.06	$-4.43^{+0.11}_{-0.12}$
2	HD 188112	20646.5 ± 210	5.75 ± 0.05	-4.7 ± 0.06	-	-	-
3	EC 15103-1557	22056.3 ± 230	5.52 ± 0.05	$-3.897^{+0.022}_{-0.018}$	-	-	-
4	CPD-20 1123	22078.5 ± 230	5.05 ± 0.05	$-0.615^{+0.011}_{-0.01}$	-4.97 ± 0.04	$-3.01^{+0.04}_{-0.06}$	$-4.02^{+0.05}_{-0.07}$
5	EC 21494-7018	22375.2^{+250}_{-230}	5.49 ± 0.05	$-3.361^{+0.021}_{-0.024}$	$-5.22^{+0.04}_{-0.05}$	-4.78 ± 0.06	-
6	HD 4539	22886.7 ± 240	5.19 ± 0.05	$-2.298^{+0.008}_{-0.006}$	$-3.95^{+0.019}_{-0.015}$	-3.74 ± 0.04	-4.85 ± 0.05
7	JL 36	23711.8^{+240}_{-250}	5.34 ± 0.05	-2.563 ± 0.014	-4.31 ± 0.03	-4.31 ± 0.04	-3.73 ± 0.05
8	EC 11349-2753	23910.3 ± 250	5.05 ± 0.05	$-2.229^{+0.013}_{-0.011}$	$-3.904^{+0.013}_{-0.012}$	$-3.935^{+0.04}_{-0.024}$	-4.9 ± 0.04
9	PG 0342+026	24411.9 ± 250	5.54 ± 0.05	$-2.669^{+0.01}_{-0.011}$	-4.861 ± 0.013	$-3.902^{+0.04}_{-0.029}$	-4.06 ± 0.05
10	PB 7352	24449.3 ± 250	5.22 ± 0.05	-2.553 ± 0.017	$-4.975^{+0.023}_{-0.022}$	$-4.532^{+0.024}_{-0.023}$	-4.11 ± 0.05
11	EC 14345-1729	24666.0^{+260}_{-250}	5.32 ± 0.05	-2.561 ± 0.016	$-4.624^{+0.025}_{-0.024}$	-4.516 ± 0.025	$-4.0^{+0.04}_{-0.05}$
12	EC 20106-5248	24892.7 ± 260	5.36 ± 0.05	$-2.712^{+0.017}_{-0.015}$	$-4.711^{+0.023}_{-0.022}$	$-4.413^{+0.025}_{-0.019}$	-3.91 ± 0.05
13	EC 23483-6445	24998.8 ± 260	5.32 ± 0.05	$-2.558^{+0.018}_{-0.015}$	$-4.667^{+0.04}_{-0.029}$	$-4.532^{+0.03}_{-0.019}$	-3.96 ± 0.05
14	LB 1516	25250.0^{+270}_{-260}	5.54 ± 0.05	$-2.789^{+0.021}_{-0.019}$	$-5.242^{+0.026}_{-0.04}$	$-4.136^{+0.022}_{-0.021}$	-4.27 ± 0.05
15	PHL 44	25806.0 ± 270	5.39 ± 0.05	$-2.938^{+0.021}_{-0.02}$	-5.2 ± 0.04	$-4.339^{+0.019}_{-0.016}$	$-4.12^{+0.05}_{-0.04}$
16	CD-38 222	26232.0 ± 270	5.45 ± 0.05	$-2.762^{+0.06}_{-0.027}$	-4.642 ± 0.029	$-4.803^{+0.023}_{-0.024}$	-4.4 ± 0.05
17	EC 23073-6905	26484.8 ± 270	5.37 ± 0.05	$-2.7^{+0.027}_{-0.023}$	-5.18 ± 0.05	$-4.257^{+0.013}_{-0.014}$	-4.08 ± 0.04
18	CD-35 15910	27061.4 ± 280	5.54 ± 0.05	$-2.971^{+0.023}_{-0.02}$	-5.4 ± 0.04	$-4.493^{+0.017}_{-0.009}$	$-4.322^{+0.03}_{-0.026}$
19	PG 2349+002	27258.2 ± 280	5.83 ± 0.05	-3.97 ± 0.04	$-5.33^{+0.09}_{-0.16}$	-5.04 ± 0.04	$-5.26^{+0.06}_{-0.1}$
20	CPD-64 481	27414.1 ± 280	5.7 ± 0.05	-2.461 ± 0.015	$-4.466^{+0.026}_{-0.027}$	$-4.048^{+0.006}_{-0.009}$	$-4.232^{+0.025}_{-0.024}$
21	EPIG 211779126	27503.5^{+280}_{-300}	5.5 ± 0.05	$-3.11^{+0.03}_{-0.04}$	-5.6 ± 0.1	$-4.543^{+0.026}_{-0.04}$	$-4.35^{+0.04}_{-0.028}$

Table 9.2: First half of the results from the spectroscopic analysis continued

#	Star name	log(Ne) [dex]	log(Mg) [dex]	log(Al) [dex]	log(Si) [dex]	log(S) [dex]	log(Ar) [dex]	log(Fe) [dex]
1	EC 03568-4849	-4.43 ± 0.06	-4.98 ± 0.04	$-6.27^{+0.07}_{-0.12}$	-4.6 ± 0.04	$-5.09^{+0.023}_{-0.024}$	$-5.26^{+0.04}_{-0.05}$	$-4.53^{+0.04}_{-0.05}$
2	HD 188112	-	-	-	-	-	-	-
3	EC 15103-1557	-	$-5.774^{+0.029}_{-0.03}$	-	$-6.7^{+0.12}_{-0.14}$	-	-	$-4.506^{+0.022}_{-0.029}$
4	CPD-20 1123	-3.9 ± 0.04	-4.34 ± 0.04	$-5.139^{+0.023}_{-0.026}$	$-4.25^{+0.02}_{-0.023}$	$-4.5^{+0.018}_{-0.022}$	-4.909 ± 0.019	$-4.165^{+0.025}_{-0.04}$
5	EC 21494-7018	-	-	-	$-6.3^{+0.09}_{-0.12}$	-	-	$-4.51^{+0.026}_{-0.05}$
6	HD 4539	-	$-5.654^{+0.024}_{-0.023}$	$-6.257^{+0.027}_{-0.04}$	$-5.266^{+0.023}_{-0.027}$	$-5.082^{+0.029}_{-0.027}$	$-5.112^{+0.013}_{-0.009}$	$-4.465^{+0.018}_{-0.019}$
7	JL 36	-	-	$-6.49^{+0.05}_{-0.08}$	$-4.997^{+0.028}_{-0.04}$	$-5.23^{+0.027}_{-0.028}$	$-5.54^{+0.05}_{-0.06}$	-4.192 ± 0.028
8	EC 11349-2753	-	-5.627 ± 0.026	$-6.417^{+0.022}_{-0.017}$	$-5.339^{+0.02}_{-0.022}$	$-5.124^{+0.022}_{-0.024}$	$-5.264^{+0.026}_{-0.024}$	$-4.601^{+0.024}_{-0.021}$
9	PG 0342+026	-	$-5.514^{+0.025}_{-0.027}$	-6.575 ± 0.026	-5.071 ± 0.029	$-5.14^{+0.029}_{-0.027}$	-5.233 ± 0.018	$-4.329^{+0.021}_{-0.022}$
10	PB 7352	-	-5.52 ± 0.04	-6.55 ± 0.04	$-5.418^{+0.023}_{-0.022}$	$-5.445^{+0.022}_{-0.023}$	-5.68 ± 0.05	$-4.491^{+0.019}_{-0.02}$
11	EC 14345-1729	-	-5.36 ± 0.04	-6.8 ± 0.06	-5.211 ± 0.021	$-5.167^{+0.024}_{-0.023}$	-5.41 ± 0.04	$-4.466^{+0.021}_{-0.019}$
12	EC 20106-5248	$-4.62^{+0.14}_{-0.13}$	-5.32 ± 0.05	-6.43 ± 0.04	$-5.282^{+0.026}_{-0.028}$	-5.35 ± 0.04	$-5.5^{+0.04}_{-0.06}$	$-4.339^{+0.026}_{-0.024}$
13	EC 23483-6445	-4.3 ± 0.07	-5.34 ± 0.04	-6.55 ± 0.06	$-5.241^{+0.026}_{-0.023}$	$-5.22^{+0.03}_{-0.04}$	-5.61 ± 0.07	$-4.569^{+0.04}_{-0.027}$
14	LB 1516	-	$-5.74^{+0.03}_{-0.04}$	-6.62 ± 0.04	-5.3 ± 0.04	-5.44 ± 0.04	-5.64 ± 0.05	$-4.342^{+0.024}_{-0.023}$
15	PHL 44	$-4.38^{+0.09}_{-0.1}$	-5.44 ± 0.04	$-6.9^{+0.09}_{-0.1}$	$-5.47^{+0.04}_{-0.03}$	$-5.52^{+0.04}_{-0.06}$	$-5.74^{+0.08}_{-0.13}$	$-4.35^{+0.021}_{-0.02}$
16	CD-38 222	-	$-5.74^{+0.05}_{-0.07}$	-	$-5.09^{+0.028}_{-0.027}$	-5.38 ± 0.06	-	-5.9 ± 0.2
17	EC 23073-6905	-	$-5.06^{+0.05}_{-0.04}$	-6.87 ± 0.12	-5.33 ± 0.04	-5.41 ± 0.05	-	-4.348 ± 0.018
18	CD-35 15910	-	$-5.432^{+0.029}_{-0.03}$	$-7.05^{+0.08}_{-0.1}$	$-5.547^{+0.018}_{-0.017}$	-5.64 ± 0.05	-	$-4.345^{+0.011}_{-0.008}$
19	PG 2349+002	-	-5.53 ± 0.05	$-6.99^{+0.11}_{-0.16}$	-5.66 ± 0.03	$-5.85^{+0.09}_{-0.1}$	-	-4.923 ± 0.024
20	CPD-64 481	$-4.58^{+0.06}_{-0.07}$	$-5.436^{+0.024}_{-0.023}$	$-6.421^{+0.015}_{-0.016}$	$-5.193^{+0.011}_{-0.012}$	$-5.138^{+0.011}_{-0.012}$	$-5.21^{+0.04}_{-0.03}$	$-4.484^{+0.005}_{-0.006}$
21	EPIC 21179126	-	-5.443 ± 0.05	-	-5.688 ± 0.025	-5.66 ± 0.07	-	$-4.428^{+0.013}_{-0.017}$

Table 9.3: First half of the results from the spectroscopic analysis continued

#	Star name	$\log(\text{Ca})$ [dex]	$\log(\text{Ti})$ [dex]	$\log(\text{CR})$ [dex]	$\log(\text{P})$ [dex]	$\log(\text{Sr})$ [dex]
1	EC 03568-4849	-	-	-	$-5.293^{+0.029}_{-0.03}$	-
2	HD 188112	-	-	-	-	-
3	EC 15103-1557	-	-	-	-	-
4	CPD-20 1123	-	-	-	$-6.27^{+0.09}_{-0.13}$	$-6.89^{+0.14}_{-0.13}$
5	EC 21494-7018	-	-	-	-	-
6	HD 4539	-5.15 ± 0.08	-6.3 ± 0.07	-	-	$-6.98^{+0.07}_{-0.09}$
7	JL 36	-	-	-	-	-
8	EC 11349-2753	-	-6.4 ± 0.05	-	-	$-7.2^{+0.13}_{-0.16}$
9	PG 0342+026	-	-	-	-	-
10	PB 7352	-	-	-	-	-
11	EC 14345-1729	-	-	-	-	-
12	EC 20106-5248	-	$-6.46^{+0.12}_{-0.08}$	-	-	-6.94 ± 0.16
13	EC 23483-6445	-	-	-	-	-
14	LB 1516	-	-6.4 ± 0.09	-	-	$-6.8^{+0.14}_{-0.16}$
15	PHL 44	-	-	-	-	-
16	CD-38 222	-	-	-	-	-
17	EC 23073-6905	-	-	-	-	-
18	CD-35 15910	-	-	-	-	-
19	PG 2349+002	-	-	-	-	-
20	CPD-64 481	-	-6.41 ± 0.04	-	-	-
21	EPIC 211779126	-	-	-	-	-

Table 9.4: Second half of the results from the spectroscopic analysis.
All abundances are given as $\frac{n}{n_{\text{Fe}}}$.
The uncertainties are 1σ uncertainties, including statistical uncertainties and systematical uncertainties of 1% in T_{eff}
and 0.05 dex in $\log(g)$.

#	Star name	T_{eff} [K]	$\log(g)$ [cgs]	$\log(\text{He})$ [dex]	$\log(\text{C})$ [dex]	$\log(\text{N})$ [dex]	$\log(\text{O})$ [dex]
22	EC 14338-1445	27514.1 ± 290	5.56 ± 0.05	-2.936 ± 0.029	-4.67 ± 0.04	-4.183 ^{+0.014} _{-0.016}	-4.53 ± 0.04
23	Feige 109	27678.1 ± 290	5.82 ± 0.05	-4.79 ^{+0.06} _{-0.07}	-	-	-
24	EC 03263-6403	27852.2 ± 300	5.32 ± 0.05	-2.78 ^{+0.05} _{-0.04}	-4.59 ± 0.07	-4.51 ± 0.04	-4.4 ± 0.04
25	EC 22029-3155	27978.7 ± 290	5.71 ± 0.05	-2.009 ± 0.017	-4.566 ^{+0.026} _{-0.028}	-4.331 ^{+0.021} _{-0.009}	-4.02 ^{+0.028} _{-0.026}
26	JL 236	28000.0 ± 290	5.61 ± 0.05	-2.637 ^{+0.027} _{-0.026}	-4.88 ± 0.05	-4.351 ^{+0.04} _{-0.016}	-4.374 ^{+0.027} _{-0.021}
27	CD-32 1567	28512.2 ± 290	5.79 ± 0.05	-1.921 ± 0.014	-4.098 ^{+0.018} _{-0.02}	-3.733 ^{+0.011} _{-0.012}	-4.345 ^{+0.023} _{-0.021}
28	Feige 38	28605.2 ± 290	5.7 ± 0.05	-2.608 ^{+0.022} _{-0.02}	-4.144 ± 0.017	-3.876 ^{+0.016} _{-0.019}	-4.467 ^{+0.015} _{-0.014}
29	GALEX J225444.1-551505	29240.3 ± 300	5.82 ± 0.05	-2.539 ^{+0.027} _{-0.026}	-	-4.708 ^{+0.04} _{-0.027}	-
30	EPIC 211708181	30247.8 ± 400	5.91 ± 0.05	-4.25 ^{+0.12} _{-0.3}	-	-	-
31	EC 20229-3716	30749.5 ± 400	5.09 ± 0.05	-1.91 ^{+0.019} _{-0.017}	-3.608 ^{+0.027} _{-0.04}	-3.83 ± 0.04	-4.473 ± 0.025
32	HE 0230-4323	31032.0 ± 400	5.65 ± 0.05	-2.672 ± 0.026	-4.84 ± 0.05	-4.51 ^{+0.04} _{-0.06}	-4.406 ^{+0.04} _{-0.025}
33	Ton S 290	31954.4 ± 400	5.81 ± 0.05	-1.924 ± 0.019	-	-4.4 ± 0.05	-
34	EC 05479-5818	32336.7 ± 400	5.99 ± 0.05	-1.632 ± 0.016	-4.08 ± 0.04	-3.9 ± 0.05	-
35	EC 21043-4017	33067.6 ± 400	5.83 ± 0.05	-1.544 ± 0.019	-	-4.1 ± 0.05	-
36	PG 0057+155	34009.9 ± 400	5.8 ± 0.05	-1.641 ^{+0.017} _{-0.018}	-	-4.419 ^{+0.028} _{-0.04}	-
37	HD 149382	34756.5 ± 400	5.87 ± 0.05	-1.444 ^{+0.015} _{-0.016}	-5.291 ^{+0.027} _{-0.026}	-4.13 ± 0.05	-
38	EC 03408-1315	35474.6 ± 400	6.0 ± 0.05	-1.64 ^{+0.017} _{-0.018}	-4.249 ^{+0.04} _{-0.025}	-4.06 ± 0.05	-
39	PG 1616+144	36232.2 ± 400	6.16 ± 0.05	-1.387 ^{+0.016} _{-0.018}	-4.78 ^{+0.05} _{-0.06}	-4.88 ± 0.09	-
40	Ton S 140	36695.5 ± 400	6.04 ± 0.05	-1.643 ^{+0.018} _{-0.019}	-4.11 ± 0.04	-4.3 ± 0.06	-
41	CW83 0825+15	38652.2 ± 400	5.98 ± 0.05	-0.769 ^{+0.007} _{-0.01}	-	-3.86 ^{+0.07} _{-0.06}	-

Table 9.5: Second half of the results from the spectroscopic analysis continued

#	Star name	$\log(\text{Ne})$ [dex]	$\log(\text{Mg})$ [dex]	$\log(\text{Al})$ [dex]	$\log(\text{Si})$ [dex]	$\log(\text{S})$ [dex]	$\log(\text{Ar})$ [dex]	$\log(\text{Fe})$ [dex]
22	EC 14338-1445	-	$-5.54^{+0.07}_{-0.08}$	-6.23 ± 0.04	$-4.715^{+0.024}_{-0.023}$	-4.802 ± 0.025	-5.43 ± 0.08	-4.709 ± 0.017
23	Feige 109	-	-5.36 ± 0.05	-6.28 ± 0.04	$-5.67^{+0.024}_{-0.025}$	-	-	-5.13 ± 0.04
24	EC 03263-6403	-	$-5.3^{+0.07}_{-0.08}$	-6.35 ± 0.09	-4.93 ± 0.04	-4.51 ± 0.05	-	-4.69 ± 0.04
25	EC 22029-3155	-	$-5.109^{+0.028}_{-0.03}$	$-6.234^{+0.022}_{-0.017}$	$-5.158^{+0.012}_{-0.011}$	$-4.938^{+0.021}_{-0.023}$	-5.08 ± 0.05	$-4.829^{+0.014}_{-0.01}$
26	JL 236	-	-5.65 ± 0.06	-	$-5.687^{+0.028}_{-0.026}$	-5.57 ± 0.06	$-5.46^{+0.08}_{-0.11}$	$-4.602^{+0.022}_{-0.018}$
27	CD-32 1567	-	$-4.512^{+0.028}_{-0.04}$	-5.53 ± 0.02	$-4.214^{+0.008}_{-0.009}$	$-4.422^{+0.025}_{-0.026}$	$-4.84^{+0.05}_{-0.04}$	-4.88 ± 0.011
28	Feige 38	-	$-4.799^{+0.03}_{-0.029}$	-6.217 ± 0.021	$-4.307^{+0.011}_{-0.012}$	$-4.481^{+0.018}_{-0.023}$	$-4.82^{+0.06}_{-0.05}$	$-4.866^{+0.016}_{-0.017}$
29	GALEX J225444.1-551505	-	-	-	-6.69 ± 0.06	-5.03 ± 0.02	$-5.08^{+0.07}_{-0.06}$	$-4.864^{+0.04}_{-0.026}$
30	EPIC 211708181	-	-	-	-	-	-	-
31	EC 20229-3716	-4.73 ± 0.05	$-5.21^{+0.024}_{-0.025}$	-6.05 ± 0.04	$-5.051^{+0.023}_{-0.026}$	$-4.92^{+0.03}_{-0.04}$	$-5.13^{+0.1}_{-0.09}$	-4.67 ± 0.05
32	HE 0230-4323	-	-5.0 ± 0.04	$-6.49^{+0.08}_{-0.12}$	-5.42 ± 0.04	-5.58 ± 0.06	-	-4.41 ± 0.05
33	Ton S 290	-	-	-	-	$-4.747^{+0.04}_{-0.029}$	$-4.4^{+0.09}_{-0.08}$	$-5.12^{+0.09}_{-0.08}$
34	EC 05479-5818	-	-	-	-7.35 ± 0.16	-3.95 ± 0.05	$-3.85^{+0.08}_{-0.07}$	-5.36 ± 0.11
35	EC 21043-4017	-	-	-	-	$-4.54^{+0.06}_{-0.05}$	$-4.09^{+0.1}_{-0.09}$	$-5.04^{+0.09}_{-0.11}$
36	PG 0057+155	-	-	-	-	$-4.76^{+0.05}_{-0.06}$	$-4.55^{+0.08}_{-0.18}$	-5.17 ± 0.11
37	HD 149382	-	-	$-7.28^{+0.13}_{-0.16}$	-	-4.36 ± 0.06	$-4.25^{+0.12}_{-0.14}$	$-5.08^{+0.09}_{-0.08}$
38	EC 03408-1315	-	-	-	-	$-3.65^{+0.07}_{-0.06}$	$-3.57^{+0.09}_{-0.11}$	-
39	PG 1616+144	-	-	-	-	$-3.96^{+0.07}_{-0.06}$	-	-
40	Ton S 140	-	-	-	-	-3.7 ± 0.07	-	-5.36 ± 0.27
41	CW83 0825+15	-4.31 ± 0.07	-5.11 ± 0.07	-	-5.53 ± 0.04	$-3.79^{+0.06}_{-0.07}$	-	-4.45 ± 0.08

Table 9.6: Second half of the results from the spectroscopic analysis continued

#	Star name	log(Ca) [dex]	log(Ti) [dex]	log(Cr) [dex]	log(P) [dex]	log(Sr) [dex]
22	EC 14338-1445	-	$-5.75^{+0.04}_{-0.05}$	-	-	-
23	Feige 109	-	-	-	-	-
24	EC 03263-6403	-	-	-	-	-
25	EC 22029-3155	-	$-6.55^{+0.09}_{-0.11}$	-	-	$-6.76^{+0.14}_{-0.18}$
26	JL 236	-	-	-	-	-
27	CD-32 1567	$-4.96^{+0.12}_{-0.11}$	-5.42 ± 0.02	-4.8 ± 0.1	-	$-6.05^{+0.09}_{-0.1}$
28	Feige 38	-	$-5.41^{+0.023}_{-0.022}$	-4.84 ± 0.09	-	-
29	GALEX J225444.1-551505	-	-	-	-	-
30	EPIC 211708181	-	-	-	-	-
31	EC 20229-3716	-	$-6.19^{+0.1}_{-0.12}$	-	-	$-6.7^{+0.17}_{-0.18}$
32	HE 0230-4323	-	-	-	-	-
33	Ton S 290	-	-	-	-	-
34	EC 05479-5818	-	$-4.77^{+0.05}_{-0.06}$	-	-	-
35	EC 21043-4017	-	$-5.27^{+0.07}_{-0.09}$	-	-	$-6.97^{+0.4}_{-0.05}$
36	PG 0057+155	-	$-5.28^{+0.08}_{-0.11}$	-	-	-
37	HD 149382	-	$-5.1^{+0.08}_{-0.07}$	$-4.33^{+0.19}_{-0.21}$	$-6.79^{+0.08}_{-0.09}$	-
38	EC 03408-1315	-	-	-	-6.48 ± 0.16	-
39	PG 1616+144	-	-	-	-	-
40	Ton S 140	-	-	-	-	-
41	CW83 0825+15	-	-4.2 ± 0.07	$-3.29^{+0.24}_{-0.27}$	-	-

Spectro-photometric results

Table 9.7: First half of the results from the spectro-photometric analysis

#	Star name	Parallax [mas]	Distance [kpc]	$\log(\Theta)$ [rad]	Radius [R_{\odot}]	Mass [M_{\odot}]	Luminosity [L_{\odot}]
1	EC 03568-4849	$0.864^{+0.025}_{-0.022}$	1.19 ± 0.04	$-10.819^{+0.008}_{-0.012}$	0.396 ± 0.012	0.3 ± 0.04	$20.9^{+1.6}_{-1.5}$
2	HD 188112	$14.002^{+0.059}_{-0.053}$	0.072 ± 0.005	-10.143 ± 0.004	$0.117^{+0.001}_{-0.001}$	$0.28^{+0.028}_{-0.026}$	2.3 ± 0.1
3	EC 15103-1557	$2.941^{+0.049}_{-0.038}$	0.345 ± 0.005	$-10.635^{+0.009}_{-0.012}$	0.167 ± 0.004	0.33 ± 0.04	5.9 ± 0.4
4	CPD-20 1123	$3.128^{+0.055}_{-0.044}$	0.325 ± 0.005	$-10.559^{+0.005}_{-0.001}$	0.214 ± 0.004	$0.183^{+0.024}_{-0.017}$	9.8 ± 0.6
5	EC 21494-7018	$4.886^{+0.04}_{-0.035}$	0.207 ± 0.002	$-10.486^{+0.018}_{-0.014}$	$0.164^{+0.002}_{-0.002}$	$0.299^{+0.04}_{-0.027}$	$6.04^{+0.4}_{-0.28}$
6	HD 4539	$5.828^{+0.079}_{-0.07}$	$0.172^{+0.002}_{-0.002}$	-10.209 ± 0.005	0.244 ± 0.004	0.34 ± 0.04	14.7 ± 0.8
7	JL 36	$1.833^{+0.036}_{-0.028}$	$0.555^{+0.01}_{-0.009}$	$-10.687^{+0.015}_{-0.012}$	0.256 ± 0.005	$0.52^{+0.06}_{-0.05}$	$18.6^{+1.1}_{-1.0}$
8	EC 11349-2753	$1.72^{+0.06}_{-0.046}$	$0.595^{+0.017}_{-0.016}$	$-10.67^{+0.017}_{-0.013}$	0.285 ± 0.009	0.33 ± 0.04	$23.9^{+1.8}_{-1.7}$
9	PG 0342+026	$5.86^{+0.052}_{-0.046}$	0.171 ± 0.001	$-10.3^{+0.02}_{-0.013}$	$0.195^{+0.002}_{-0.003}$	0.47 ± 0.05	12.1 ± 0.6
10	PB 7352	$2.153^{+0.069}_{-0.055}$	$0.473^{+0.013}_{-0.012}$	$-10.588^{+0.006}_{-0.022}$	0.259 ± 0.008	0.4 ± 0.05	$21.5^{+1.6}_{-1.5}$
11	EC 14345-1729	$1.74^{+0.046}_{-0.037}$	$0.585^{+0.014}_{-0.012}$	$-10.734^{+0.018}_{-0.015}$	$0.239^{+0.006}_{-0.007}$	0.43 ± 0.05	18.9 ± 1.3
12	EC 20106-5248	$2.337^{+0.177}_{-0.136}$	$0.432^{+0.028}_{-0.024}$	$-10.658^{+0.008}_{-0.025}$	0.205 ± 0.013	$0.35^{+0.07}_{-0.05}$	$14.4^{+2.1}_{-1.7}$
13	EC 23483-6445	$1.514^{+0.039}_{-0.032}$	$0.67^{+0.015}_{-0.014}$	$-10.851^{+0.017}_{-0.018}$	0.219 ± 0.006	0.36 ± 0.04	16.8 ± 1.1
14	LB 1516	$1.882^{+0.054}_{-0.042}$	$0.541^{+0.013}_{-0.012}$	-10.764 ± 0.007	0.209 ± 0.006	$0.54^{+0.07}_{-0.06}$	$15.9^{+1.1}_{-1.0}$
15	PHL 44	$1.586^{+0.045}_{-0.036}$	$0.642^{+0.016}_{-0.015}$	$-10.86^{+0.04}_{-0.05}$	$0.221^{+0.006}_{-0.007}$	0.43 ± 0.05	$19.4^{+1.4}_{-1.3}$
16	CD-38 222	$5.485^{+0.164}_{-0.147}$	$0.183^{+0.006}_{-0.005}$	$-10.155^{+0.016}_{-0.029}$	$0.226^{+0.008}_{-0.007}$	$0.52^{+0.07}_{-0.06}$	$21.7^{+1.7}_{-1.6}$
17	EC 23073-6905	$2.022^{+0.048}_{-0.037}$	$0.504^{+0.01}_{-0.009}$	$-10.698^{+0.015}_{-0.017}$	0.224 ± 0.006	0.42 ± 0.05	22.2 ± 1.4
18	CD-35 15910	$4.169^{+0.072}_{-0.065}$	0.241 ± 0.004	$-10.393^{+0.008}_{-0.01}$	0.218 ± 0.005	$0.6^{+0.06}_{-0.08}$	22.8 ± 1.3
19	PG 2349+002	$2.176^{+0.043}_{-0.035}$	0.466 ± 0.008	-10.77 ± 0.019	$0.158^{+0.005}_{-0.007}$	$0.59^{+0.09}_{-0.08}$	$12.2^{+1.0}_{-1.2}$
20	CPD-64 481	$4.431^{+0.041}_{-0.037}$	$0.227^{+0.002}_{-0.002}$	$-10.449^{+0.005}_{-0.014}$	$0.176^{+0.002}_{-0.004}$	0.56 ± 0.06	15.6 ± 0.9
21	EPIC 211779126	$1.871^{+0.05}_{-0.038}$	$0.546^{+0.012}_{-0.011}$	$-10.96^{+0.11}_{-0.003}$	0.205 ± 0.005	0.48 ± 0.06	$21.5^{+1.5}_{-1.3}$

Table 9.8: Second half of the results from the spectro-photometric analysis

#	Star name	Parallax [mas]	Distance [kpc]	$\log(\Theta)$ [rad]	Radius [R_{\odot}]	Mass [M_{\odot}]	Luminosity [L_{\odot}]
22	EC 14338-1445	$1.67^{+0.037}_{-0.032}$	$0.61^{+0.013}_{-0.012}$	$-10.873^{+0.022}_{-0.028}$	0.19 ± 0.005	0.48 ± 0.06	$18.6^{+1.3}_{-1.1}$
23	Feige 109	$2.032^{+0.043}_{-0.038}$	$0.499^{+0.01}_{-0.009}$	$-10.89^{+0.012}_{-0.02}$	0.139 ± 0.004	0.46 ± 0.05	$10.1^{+0.7}_{-0.6}$
24	EC 03263-6403	$1.583^{+0.032}_{-0.027}$	$0.631^{+0.012}_{-0.011}$	-10.849 ± 0.014	$0.192^{+0.005}_{-0.007}$	$0.27^{+0.04}_{-0.03}$	$19.6^{+1.4}_{-1.5}$
25	EC 22029-3155	$2.63^{+0.056}_{-0.044}$	0.387 ± 0.007	$-10.631^{+0.022}_{-0.023}$	$0.188^{+0.006}_{-0.007}$	0.65 ± 0.08	$19.3^{+1.4}_{-1.5}$
26	JL 236	$1.59^{+0.033}_{-0.027}$	$0.638^{+0.011}_{-0.012}$	$-10.871^{+0.011}_{-0.013}$	$0.186^{+0.005}_{-0.006}$	0.5 ± 0.06	$19.0^{+1.3}_{-1.4}$
27	CID-32 1567	$5.465^{+0.039}_{-0.035}$	0.184 ± 0.001	-10.418 ± 0.006	$0.148^{+0.002}_{-0.006}$	0.47 ± 0.06	$12.8^{+0.8}_{-1.1}$
28	Feige 38	$2.098^{+0.071}_{-0.056}$	$0.484^{+0.014}_{-0.013}$	$-10.762^{+0.009}_{-0.01}$	0.172 ± 0.005	0.54 ± 0.06	$17.7^{+1.3}_{-1.2}$
29	GALEX J225444.1-551505	$3.431^{+0.05}_{-0.04}$	0.295 ± 0.004	$-10.688^{+0.013}_{-0.018}$	0.141 ± 0.002	0.47 ± 0.05	13.0 ± 0.7
30	EPIC 211708181	$1.244^{+0.053}_{-0.046}$	$0.82^{+0.04}_{-0.03}$	$-10.868^{+0.012}_{-0.026}$	0.199 ± 0.009	$1.16^{+0.16}_{-0.14}$	$29.6^{+4.0}_{-2.7}$
31	EC 20229-3716	$1.77^{+0.061}_{-0.054}$	$0.564^{+0.018}_{-0.017}$	$-10.505^{+0.017}_{-0.026}$	$0.363^{+0.016}_{-0.019}$	0.57 ± 0.08	$105.3^{+11.0}_{-12.0}$
32	HE 0230-4323	$1.176^{+0.066}_{-0.058}$	0.86 ± 0.05	$-10.97^{+0.07}_{-0.007}$	$0.181^{+0.017}_{-0.012}$	$0.53^{+0.12}_{-0.09}$	$27.0^{+6.0}_{-4.0}$
33	Ton S 290	$1.518^{+0.041}_{-0.036}$	$0.668^{+0.017}_{-0.016}$	$-11.042^{+0.06}_{-0.021}$	0.148 ± 0.004	0.51 ± 0.06	20.4 ± 1.4
34	EC 05479-5818	$2.4^{+0.063}_{-0.05}$	0.416 ± 0.009	$-10.82^{+0.016}_{-0.022}$	0.132 ± 0.004	$0.62^{+0.07}_{-0.08}$	17.0 ± 1.1
35	EC 21043-4017	$1.891^{+0.053}_{-0.042}$	$0.537^{+0.013}_{-0.012}$	$-11.013^{+0.1}_{-0.013}$	$0.154^{+0.005}_{-0.006}$	0.58 ± 0.07	$25.5^{+1.9}_{-2.0}$
36	PG 0057+155	$3.152^{+0.062}_{-0.05}$	0.322 ± 0.006	$-10.617^{+0.018}_{-0.024}$	0.15 ± 0.003	$0.51^{+0.06}_{-0.05}$	$26.9^{+1.6}_{-1.5}$
37	HD 149382	$13.272^{+0.064}_{-0.057}$	0.076 ± 0.005	$-10.048^{+0.013}_{-0.014}$	$0.146^{+0.002}_{-0.001}$	0.57 ± 0.06	28.0 ± 1.3
38	EC 03408-1315	$1.891^{+0.055}_{-0.048}$	$0.528^{+0.014}_{-0.013}$	$-10.915^{+0.017}_{-0.006}$	0.123 ± 0.005	0.54 ± 0.07	21.5 ± 1.8
39	PG 1616+144	$1.817^{+0.039}_{-0.033}$	$0.555^{+0.011}_{-0.01}$	$-11.08^{+0.07}_{-0.005}$	0.131 ± 0.003	$0.89^{+0.1}_{-0.09}$	$26.5^{+1.7}_{-1.6}$
40	Ton S 140	$1.546^{+0.041}_{-0.037}$	$0.657^{+0.017}_{-0.016}$	$-11.047^{+0.027}_{-0.006}$	0.12 ± 0.004	$0.57^{+0.07}_{-0.08}$	$23.4^{+1.8}_{-1.6}$
41	CW83 0825+15	$3.773^{+0.064}_{-0.055}$	$0.269^{+0.005}_{-0.004}$	$-10.642^{+0.015}_{-0.04}$	$0.128^{+0.002}_{-0.003}$	0.56 ± 0.06	$32.5^{+1.9}_{-1.8}$

Galex J093448.2-251248

GALEX J093448.2-251248 is binary system, which was further investigated. Veronika Schaffenroth studied the light curve of the star and found periodic light variations due to reflective effects with a period of 0.1429033 d (priv. comm.). To confirm these results, I analyzed the FEROS spectra to determine their radial velocities. Together with the time of observation, the radial velocity curve in Figure 9.1 and the periodogram in Figure 9.2 can be determined. The resulting period of my analysis is 0.1429032 ± 0.000011 d and matches with the one from the light curve. All resulting orbital parameters are given in Table 9.9.

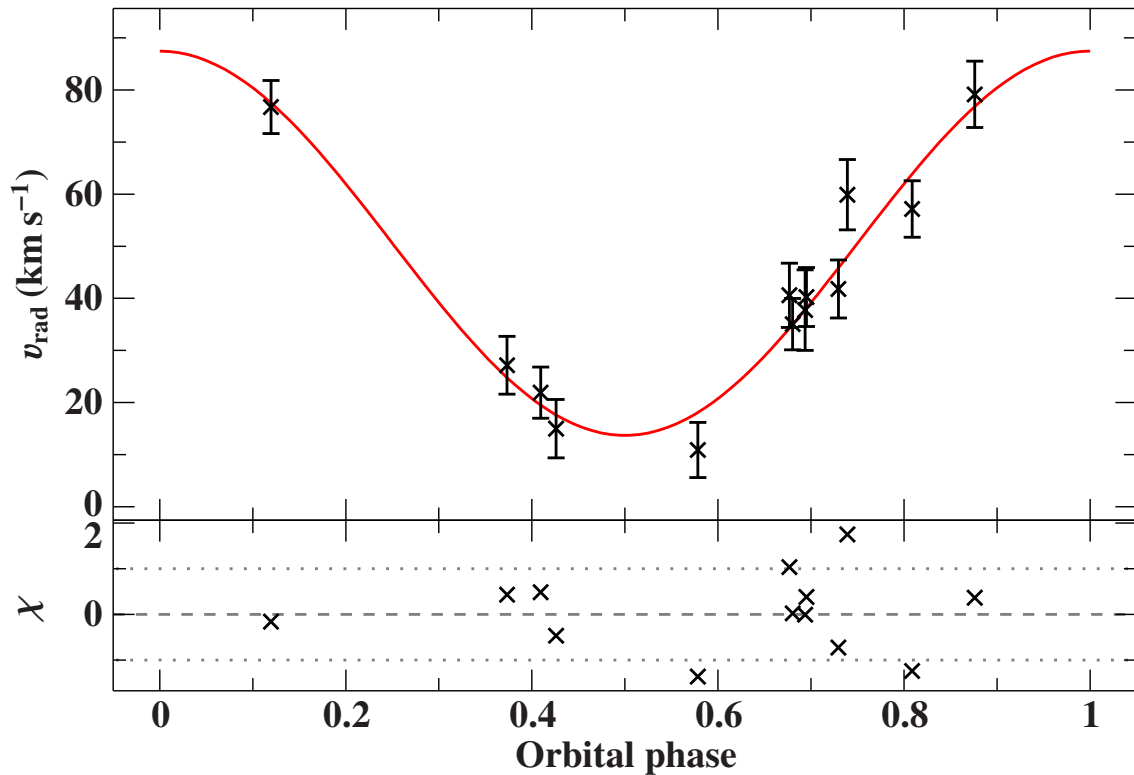


Figure 9.1: Radial velocity curve of GALEX J093448.2-251248. The top panel shows the best fit for the radial velocity curve during one orbital phase in red. The black data points are radial velocity measurements of different spectra. The bottom panels shows the residuals, χ , that is the difference between measured data points and best fit, divided by the corresponding uncertainties.

Parameter	Value
Period P	$0.1429032^{+0.0000011}_{-0.0000010}$ d
Epoch of periastron	$2456995.0654^{+0.0026}_{-0.0029}$ HJD
Velocity semiamplitude K	37 ± 4 km s $^{-1}$
Systemic velocity γ	50.6 ± 2.1 km s $^{-1}$
Mass function $f(M)$	$(7.4^{+2.0}_{-1.7}) \cdot 10^{-4} M_{\odot}$

Table 9.9: Orbital parameters of the radial velocity curve in Figure 9.1 of GALEX J093448.2-251248.

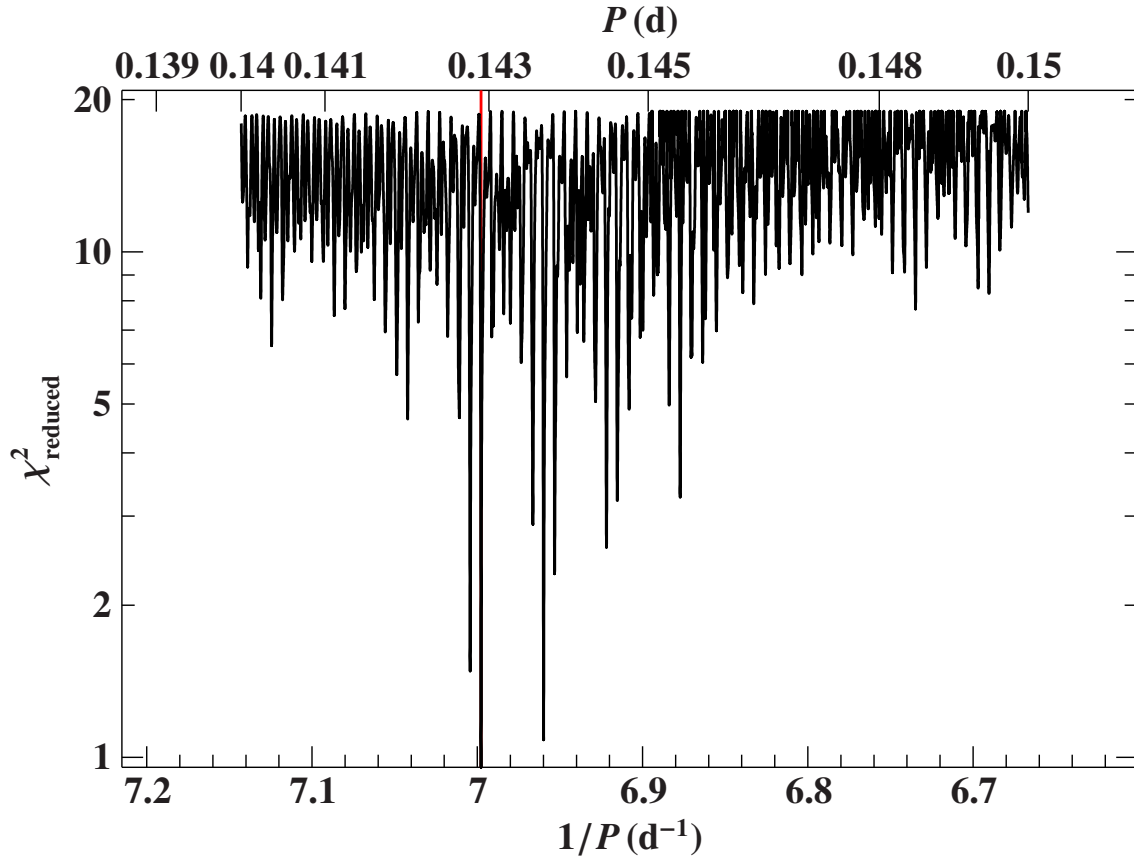


Figure 9.2: Periodogram of GALEX J093448.2-251248. The diagram shows the period P on the upper x-axis with the reduced χ^2 on the y-axis. The most likely period is marked in red and is $P = 0.1429032$ d.

Results of the sorted out stars

Star	T_{eff} [K]	$\log(g)$	$\log(n(\text{He}))$	Reason for sorting out
PG 2159+051 ^a	14500 ^a	3.3 ^a	-	No subdwarf
PHL 460 ^b	15000 ^b	3.9 ^b	-	No subdwarf
EC 04420-1908 ^b	14000 ^b	3.4 ^b	-	No subdwarf (BHB)
PHL 2018 ^b	19095 ^b	3.4 ^b	-	No subdwarf
CD-68 82 ^c	20500 ^c	3.2 ^c	-	No subdwarf (Post-AGB)
EC 10282-1605 ^d	$\sim 16000^d$	-	-	No subdwarf (MS-B)
PG 1258-030	15375	< 4.6	-2.62	No subdwarf
EC 09452-1403	16448	< 4.6	-1.42	No subdwarf
[DSH99] 456-21	18523	< 4.6	< -4.05	Unusable spectra
KPD 2022+2033	23790	5.03	-1.47	Unusable spectra
PG 1432+004	25733	5.35	-2.37	Unusable spectra
EC 10475-2118	25992	5.36	-1.35	Binary system ^(*)
HD 86248	27951	< 4.6	-1.04	No subdwarf
PG 2111+023	28187	5.59	-2.66	Unusable spectra
TYC 6369-1068-1	29017	< 4.6	< -4.05	No subdwarf
CD-24 16312	29272	< 4.6	-1.25	No subdwarf
HD 119069	29525	< 4.6	-1.12	No subdwarf
PB 7032	29562	5.95	-3.47	Unusable spectra
HE 0218-3437	29808	5.67	-2.98	Unusable spectra
Ton S 201	29955	< 4.6	< -4.05	Unusable spectra
EC 03143-5945	32285	5.55	-2.73	Binary system ^(*)
LB 1695	32886	5.79	-2.82	Unusable spectra
CD-40 13747	33558	6.51	-3.27	Binary system ^(*)
V* NY Vir	34536	5.69	-2.95	Fast rotator
EC 22081-1916	34996	5.34	-2.45	Fast rotator
TYC 8977-3335-1	35794	< 4.6	< -4.05	No subdwarf
GALEX J093448.2-251248	40818	5.55	-2.31	Fast rotator

Table 9.10: Results of the initial guess of the sorted out stars. These values are rough estimates. No detailed analysis was performed on these stars. The binary systems marked with ^(*) have probably a companion which contributes to the spectrum of the subdwarf. Stars marked with a letter are known no subdwarfs and literature values are given, which are taken from: ^(a)Lynn et al. (2004); ^(b)Silva & Napiwotzki (2011); ^(c)Magee et al. (2001); ^(d)Copperwheat et al. (2011).

Left out stars

Star	Classification Geier et al. (2019)	Star	Classification Geier et al. (2019)
HD 110698	-	PG 2151+100	sdB
JL 82	sdB+dM	UCAC2 23234937	sdO
Ton S 135	sdB+WD	[CW83] 1419-09	sdOB
CPD-20 1123	sdB+WD	EC 13047-3049	sdB
CD-45 5058	sdO	PHL 1548	sdOB
HD 205805	sdB	CD-24 731	sdB+WD
GD 108	sdB+WD	EC 10189-1502	sdOB
EC 12234-2607	sdB	Ton S 61	sdB
EC 14248-2647	sdOB	[YSS2013] 107	-
Balloon 90100001	sdBV	PG 0909+164	sdB
HD 76431	-	CD-48 106	sdBV
EC 03143-5945	sdB+MS	PG 2317+046	sdOB+WD
BPS CS 22940-0009	He-sdB	CD-46 8926	He-sdO
CD-48 8608	sdB	JL 119	sdOB
TYC 6545-1888-1	-	HD 127493 ^a	sdO
V* UY Sex	sdBV	EC 14316-1908	-
PG 2110+127	sdB+F	PG 1352-023	sdOB
GD 1110	sdB+dM/BD	HD 159176B	-
HD 134199	-	PG 1127+019	He-sdO
PG 2148+095	sdB+K	GALEX J095256.6-371940	He-sdO
JL 87	He-sdB	[CW83] 0832-01	He-sdO
EC 13506-3137	sdB	LS 1150	sdO
Feige 110	sdOB	CPD-31 1701 ^b	sdO
CD-24 9052	He-sdO	JL 25	sdOB
Ton S 183	sdB+WD	LS IV -12 1	sdO
PG 1506-052	sdOB	[CW83] 0904-02 ^b	He-sdO
NGC 5139 5701	-	V* V603 Aql	-
LB 1766	sd	PHL 382	-

Table 9.11: Stars which were left out due to time constraints, along with the spectral classification in Geier et al. (2019) if available. He-sdBs and He-sdOs were also excluded since the models used during this analysis are not suited for these types of stars.^(a)Elemental abundances available in Dorsch et al. (2019).^(b)Elemental abundances available in Schindewolf et al. (2018).

Eigenständigkeitserklärung

Hiermit erkläre ich, dass ich diese Arbeit selbstständig und nur unter Verwendung der angegebenen Hilfsmittel angefertigt habe.

Datum, Ort

Lars Möller